AFRL-VA-WP-TR-2004-3080

FILTERED RAYLEIGH SCATTERING VELOCIMETRY FOR WIND TUNNEL APPLICATIONS

Jim Crafton, Greg Elliott, Campbell Carter, Tom Beutner, Henry Baust, and Andrew Mosdale

Innovative Scientific Solutions, Inc.
2766 Indian Ripple Rd.
Dayton, OH 45440-3638

APRIL 2004

Final Report for 01 January 1998 – 01 January 2004

THIS IS A SMALL BUSINESS INNOVATION RESEARCH (SBIR) PHASE II REPORT.

STINFO FINAL REPORT

AIR VEHICLES DIRECTORATE
AIR FORCE MATERIEL COMMAND
AIR FORCE RESEARCH LABORATORY
WRIGHT-PATTERSON AIR FORCE BASE, OH 45433-7542

NOTICE

/s/

HENRY D. BAUST
Project Engineer
Aerospace Vehicles Integration and
  Demonstration Branch
Aeronautical Sciences Division

/s/

FRANK WITZEMAN
Chief
Aerospace Vehicles Integration and
  Demonstration Branch
Aeronautical Sciences Division

/s/

TIM J. SCHUMACHER, Chief
Aeronautical Sciences Division
Air Vehicles Directorate

REPORT DOCUMENTATION PAGE		*Form Approved* *OMB No. 0704-0188*

The public reporting burden for this collection of information is estimated to average 1 hour per response, including the time for reviewing instructions, searching existing data sources, searching existing data sources, gathering and maintaining the data needed, and completing and reviewing the collection of information. Send comments regarding this burden estimate or any other aspect of this collection of information, including suggestions for reducing this burden, to Department of Defense, Washington Headquarters Services, Directorate for Information Operations and Reports (0704-0188), 1215 Jefferson Davis Highway, Suite 1204, Arlington, VA 22202-4302. Respondents should be aware that notwithstanding any other provision of law, no person shall be subject to any penalty for failing to comply with a collection of information if it does not display a currently valid OMB control number. **PLEASE DO NOT RETURN YOUR FORM TO THE ABOVE ADDRESS**.

1. REPORT DATE *(DD-MM-YY)*	2. REPORT TYPE	3. DATES COVERED *(From - To)*
April 2004	Final	01/01/1998 – 01/01/2004

4. TITLE AND SUBTITLE	5a. CONTRACT NUMBER
FILTERED RAYLEIGH SCATTERING VELOCIMETRY FOR WIND TUNNEL APPLICATIONS	F33615-98-C-3001
	5b. GRANT NUMBER
	5c. PROGRAM ELEMENT NUMBER 0605502

6. AUTHOR(S)	5d. PROJECT NUMBER
Jim Crafton, Greg Elliott, Campbell Carter, Tom Beutner, Henry Baust, and Andrew Mosdale	A06S
	5e. TASK NUMBER 0A
	5f. WORK UNIT NUMBER

7. PERFORMING ORGANIZATION NAME(S) AND ADDRESS(ES)	8. PERFORMING ORGANIZATION REPORT NUMBER
Innovative Scientific Solutions, Inc. 2766 Indian Ripple Rd. Dayton, OH 45440-3638	

9. SPONSORING/MONITORING AGENCY NAME(S) AND ADDRESS(ES)	10. SPONSORING/MONITORING AGENCY ACRONYM(S)
Air Vehicles Directorate Air Force Research Laboratory Air Force Materiel Command Wright-Patterson Air Force Base, OH 45433-7542	AFRL/VAAI
	11. SPONSORING/MONITORING AGENCY REPORT NUMBER(S) AFRL-VA-WP-TR-2004-3080

12. DISTRIBUTION/AVAILABILITY STATEMENT
Approved for public release; distribution is unlimited. This is a Small Business Innovation Research (SBIR) Phase II report.

13. SUPPLEMENTARY NOTES
Report contains color.

14. ABSTRACT

Molecular/atomic filter techniques offer the potential of making quantitative and multi-component two-dimensional velocity measurements. Furthermore, they appear well suited to applications in large scale facilities. As such, considerable interest in these techniques has been generated during the past several years. The goals of the current research program were to develop and demonstrate a molecular filtered based velocimetry system (including the hardware and software). The system demonstration was to be carried out on various flow fields of interest.

15. SUBJECT TERMS
SBIR Phase II Report

16. SECURITY CLASSIFICATION OF:			17. LIMITATION OF ABSTRACT:	18. NUMBER OF PAGES	19a. NAME OF RESPONSIBLE PERSON (Monitor)
a. REPORT Unclassified	b. ABSTRACT Unclassified	c. THIS PAGE Unclassified	SAR	192	Henry D. Baust
					19b. TELEPHONE NUMBER *(Include Area Code)* (937) 255-5747

Standard Form 298 (Rev. 8-98)
Prescribed by ANSI Std. Z39-18

Table of Contents

List of Figures

List of Tables

Acknowledgments

1. INTRODUCTION

Molecular/atomic filter techniques offer the potential of making quantitative and multi-component two-dimensional velocity measurements. Furthermore, they appear well suited to applications in large scale facilities. As such, considerable interest in these techniques has been generated during the past several years. The goals of the current research program were to develop and demonstrate a molecular filtered based velocimetry system (including the hardware and software). The system demonstration was to be carried out on various flow fields of interest.

1.1. General Description of PDV

The basis of these techniques lye in measuring the Doppler shift of laser light scattered off of moving particles. These particles are generally seeded into the flow (such as smoke, fog, aluminum oxide, condensation etc.) or occur naturally through condensation processes. When the laser light is scattered by a moving particle, the frequency of the light is shifted according to the Doppler shift equation:

$$\Delta f_D = \frac{1}{\lambda}\left(\underline{k}_o - \underline{k}_i\right)\cdot\underline{V}$$ Equation 1.1

where Δf_D is the Doppler shift, λ is the wavelength of the incident laser light, $\underline{k}_0$ is the unit vector in the scattering direction (sometimes referred to as the observation vector), $\underline{k}_i$ is the unit vector in the direction of the incident laser propagation (sometimes referred to as the incident light vector), and $\underline{V}$ is the velocity vector associated with the fluid flow.

The presence of this Doppler shift allows the molecular-filter-based diagnostic techniques described below to measure velocity. The Doppler shift of light is well known and has been used by astronomers for years to determine the velocity of stars based on the shift in emission spectra. Indeed, in flow applications, where a fluorescent species is present and excited, a similar technique may be applied.[1,2] What is novel in this new class of diagnostic techniques, however, is that they do not depend on a fluorescent species being present in the flow: instead they operate with light scattered by particles in the flow with the absorption species located in the detection system.

Before describing PDV in detail, a general description is given here. PDV uses a narrow-linewidth laser to illuminate a plane of the flow field as illustrated in Figure 1.1. As illustrated,

the laser sheet is imaged by one camera which views the illuminated plane through a molecular filter, termed the signal camera (or signal image). A second camera views the plane without a filter, this is termed the reference camera (or reference image). The molecular filter is simply an optical cell (glass cylinder with windows on each end) containing a molecule having an absorption line in the frequency tuning range of the illuminating laser. This results in a filter that has a transmission profile with finite sloping edges as shown in Figure 1.2a. The term I_v / I_0 is the spectral transmission of the molecular filter, with I_v defined as the spectral intensity (intensity at frequency v) after the cell, and I_0 defined as the spectral intensity before entering the cell. The flow field contains small particles which are seeded into the flow or occur naturally (such as condensation) and scatter the illuminating light from the laser sheet. The spectral intensity of the light which passes through the molecular filter is the convolution of the scattered spectral intensity from the particles illuminated in the flow field, and the absorption profile of the molecule present within the cell (as illustrated in Figure 1.2b). As an example, consider a case where the laser frequency, f_0, is tuned to the midpoint of the transmission profile. The scattered light experiences a change in frequency, due to the Doppler shift (Equation 1.1), causing the transmission from the scattered light to either increase or decrease depending on whether the frequency increases or decreases. Note, also, that there is no ambiguity in the direction of the shift: positive and negative frequency shifts are distinguished by the increase or decrease in transmission respectively. The pixels of the signal camera CCD array, record the integrated spectral intensity which is transmitted through the molecular filter's absorption profile and is given by I (i.e. $I = \int I_v \, dv$ with the limits on the integration dependent on the spectral sensitivity of the camera and optics). The second reference camera (or a separate portion of the same camera) is used to collect images of the flow field without the molecular filter. The reference camera is used to account for intensity fluctuations due to laser energy (and/or sheet energy distribution) or seed-concentration variations. The reference camera records I_0, which is the integrated spectral intensity of the unfiltered light ($I_0 = \int I_{0v} \, dv$).

The integrated transmission through the cell (TR) is obtained by dividing the intensities of the signal (I) and reference (I_0) cameras at corresponding pixels. Figure 1.2c shows a plot of the integrated transmission as the independent variable and the frequency shift (or frequency function, determined from the given filter) as the dependent variable with points taken from Figure 1.2b highlighted. In an experiment, once the integrated transmission (TR) is determined

2

from the two cameras at each corresponding pixel, the Doppler shift can be found at each pixel using the frequency function of the filter (Figure 1.2c). The velocity is then calculated at each pixel of the image using this measured Doppler shift and Equation 1.1. This equation can be recast in scalar form as

$$\Delta f_D = \left[\frac{2 \sin\left(\frac{\phi}{2}\right)}{\lambda} \right] V \cos(\Omega) \qquad \text{Equation 1.2}$$

where ϕ is the angle between the incident and scattering vectors, and Ω is the angle between the velocity vector and the direction of PDV system sensitivity. The latter is the direction of the vector difference, ($\underline{k}_0$-$\underline{k}_i$) seen in Equation 1.1. In Equation 1.2, the term $V\cos(\Omega)$ can be thought of as the quantity to be measured, which is the velocity component parallel to the direction of PDV system sensitivity. The term in brackets is then an expression for the geometrical sensitivity of the particular PDV system arrangement. Note that this sensitivity depends only on the relationship between the incident and scattering vectors and is independent of the flow. Viewed in its scalar form, the Doppler shift equation can be thought of as one equation in one unknown: given the Doppler shift, the velocity component in the direction of PDV system sensitivity may be calculated. Figure 1.3 illustrates the relationship between the vectors and angles discussed above. The derivation of these equations can be found in Drain[3].

As may be noted in Equation 1.2, the measured Doppler shift is dependent on the angle between the illumination and observation directions, respectively. This fact may be exploited in order to make multi-component velocity measurements—either by viewing the flow field from more than one direction (changing the direction of the observed vector), or by illuminating the flow field from multiple directions (changing the direction of the incident light wave vector). Both approaches have been used by researchers in order to make multi-component measurements.

Over the last fifteen years many different acronyms have been given to essentially similar molecular-filter-based techniques to measure velocity. These include PDV[4] Doppler Global Velocimetry (DGV[5,6] which was the first system developed), Filtered Planar Velocimetry[7,8] Absorption Filter-Planar Doppler Velocimetry,[9] and Filtered Rayleigh Scattering (FRS) Velocimetry[10]. In addition it should be noted that molecular filtered based methodologies have been investigated utilizing scattering from molecules to obtain property measurements other than

velocity. Although each research group has their preference and each acronym represents different characteristics of the technique, PDV seems to be gaining wider acceptance in the literature[11]. It should be recognized that the early work of Komine and Brosnan,[5] Komine et al.,[12] and Meyers and Komine[6] who introduce molecular filters to aerodynamic measurement pioneered several of the features common to many molecular filtered based diagnostics. These works outlined many of the basic ideas of DGV and PDV and stand as the original proofs-of-concept to the data collection and analysis methodologies.

1.2. Comparison of PDV and PIV

Particle image velocimetry (PIV) is a planar velocity measurement technique which has gained wide acceptance in resent years. This is relatively easy to apply and is commercially available. Several companies now offer complete packages including the needed lasers, cameras, optics, and processing software. The basic concept behind PIV, illustrated in Figure 1.4, is to form a beam from a laser into a sheet using a combination of cylindrical and spherical optics or by sweeping the beam with a rotating mirror. Using a fast shutter or a double pulsed laser (i.e. second harmonic of a double pulsed Nd:YAG laser) the beam is pulsed twice with a delay between the two pulses of Δt. A camera views the laser sheet orthogonally as shown. The flow is then seeded with particles, which are individually visualized by the camera. In the early years of development, film cameras were used and both the initial and delayed images were recorded on one frame which resulted in problems with directional ambiguity that were difficult to resolve. This problem has been largely resolved by utilizing interline transfer or frame transfer digital cameras. These cameras can take two independent images (or frames) of the particle field with delay times as short as 500 ns between successive images. Due to the method that these digital cameras store and retrieve the data, they are referred to as interline transfer cameras (which is the most common) and PIV is then termed DPIV when utilizing them. Once the two frames are taken, the image is processed using two-dimensional cross-correlation techniques to determine the distance (dx) that a predefined subregion region of particles in the flow has translated during the time between pulses (Figure 1.5). After image processing and calculation of the cross-correlation of each sub-region, the magnitude and direction of each sub-region can be calculated. The pixel location of the peak in the cross-correlation indicates the distance that the particles in the sub-region have traveled between images. Since the time delay

between laser pulses (*dt*) and distance the particles have traversed (*dx*) is known, the magnitude of the velocity is simply defined as *V=dx/dt*. Variations on this technique include using steroscopic viewing with two cameras to obtain the out-of-plane velocity component. Also some researchers have utilized two wavelengths of laser light so that the initial and delayed image can be separated by color. This allows much shorter time delays to be utilized. A more complete review of PIV can be found in the book authored by Raffel et. al.[13]

In comparing PDV and PIV there are advantages and disadvantages in using each technique. Some of these items are described in more detail in the review article by Samimy and Wernet.[11] The following is a list of the advantages of each technique when comparing the PDV and PIV.

1.2.1. Advantages of PDV compared to PIV:

1. Larger fields of view are obtainable: Unlike PIV, PDV does not need to image individual particles, but measures the Doppler shift of the scattering from a volume of scattering particles. Therefore the imaging size and resolution is not restricted by the ability to image and track the displacement individual particles. For best results PIV requires that the imaged particle take up at least four pixels so that spatial correlations can be computed accurately.

2. Seeding requirements less stringent: Well controlled seeding is a significant issue for PIV. If there is too much seeding, individual particles are not distinct and if there is too little seeding, there are not enough particles to compute good vectors in each image sub-region leading to significant data fall out (i.e. inaccurate vectors). PDV only has a requirement that the seeding be high enough so that it can be imaged at a sufficient intensity level. This greatly easies constraints on the seeding level and uniformity, although extremely high particle loading can cause secondary scattering problems.

3. Less problems with particles tracking the flow: Since PDV images a volume of particles instead of individual particles much smaller particles can be used in seeding. Condensation particles in the Rayleigh scattering regime have often been utilized for PDV measurements. These small particles track the actual fluid much more accurately in the presence of large velocity gradients (i.e shock waves) that can not be tracked by larger particles needed for PIV. It is even possible to use the actual air molecules as a scattering medium in smaller flow fields, which has the added benefit of allowing additional flow properties to be calculated.

4. High in-plane velocities can be resolved: In order for the particles to be tracked by PIV, they must remain in the interrogating laser sheet from the initial to the delayed laser pulse. This sets a maximum on the allowable delay time with the minimum delay time set by having a sufficient displacement so that the velocity can be resolved. For some flow fields (i.e. vortices created from strakes and wings) the "thru plane velocity" is much higher than the cross-stream component being measured making accurate measurements difficult using PIV. Since PDV uses only one pulse, there is no such requirement on the thru plane velocity.

5. Better applicability for high-speed flows: One difficulty in high speed flows is the ability of particles to track the flow since the turbulence and shock waves can create problems resolving the flow velocity using PIV for reasons stated previously (see 2 and 3 described previously). In addition as the velocity increases so does the Doppler shift and the intensity variations become more well defined using PDV.

1.2.2. Disadvantages of PDV compared to PIV:

1. More complicated technique: There is no doubt that the biggest draw back with PDV in comparison with PIV is that it is a much more difficult technique to implement. PDV requires more intensive on-sight calibration (Although stereoscopic PIV has similar calibration techniques), more equipment (six cameras, wavemeter, multiple data collection computers, and stable injection seeded laser), and a much greater requirement that all components operate at peak performance. For a two component PIV measurement only a single interline transfer camera is needed and a double-pulsed laser, which does not need to be injection seeded and can be of a significantly lesser quality than that needed for PDV.

2. Single components generally not aligned with geometry or flow: Since PDV measures velocity components from the Doppler shift, the viewing angle and incident laser direction determine the velocity component measured. Generally for a single component the light sheet and viewing angle can not be set so that the illumination is normal or along a flow direction while the velocity component measured is in alignment with a typical independent coordinate.

Not suitable for low speed flows: PDV must have a Doppler shift significant enough to be measured. From most studies the accuracy quoted is generally on the order of 1 m/s. This is limited by the current stability and line-width of available lasers and accuracy of current camera systems.
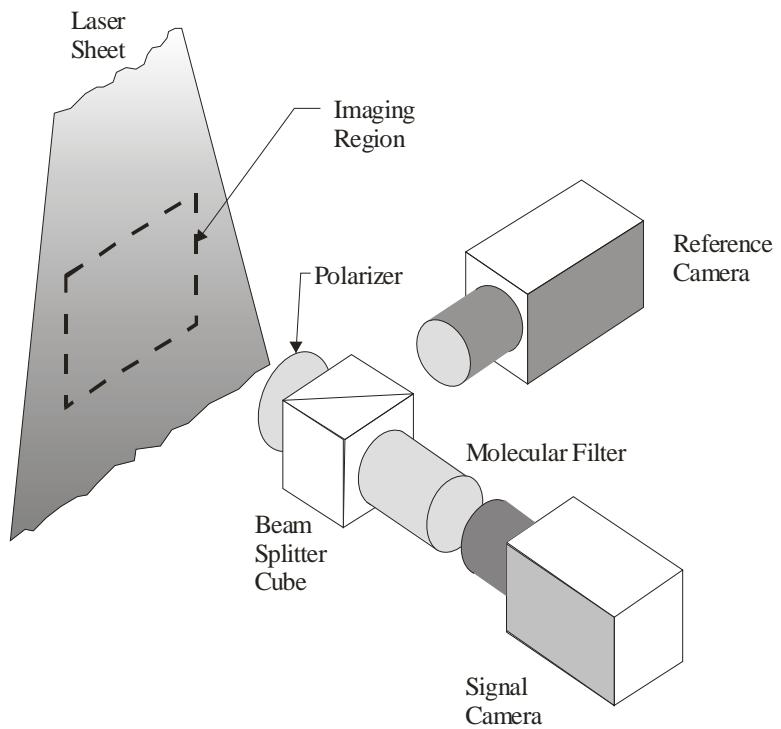
Figure 1.1 Planar Doppler Velocimetry (PDV) general optical arrangement.

a)

$I_\nu / I_{0\nu}$

Frequency

b)

$I_\nu / I_{0\nu}$

Δf_D

Doppler Shifted
Scattering

f_0

Frequency

c)

Doppler Shift (Frequency function, ζ; GHz)

$\hat{f}_0$

Δf_D

0.5
0.4
0.3
0.2
0.1
0.0
- 0.1
- 0.2
- 0.3
- 0.4
- 0.5

0.0   0.1   0.2   0.3   0.4   0.5   0.6   0.7   0.8   0.9   1.0
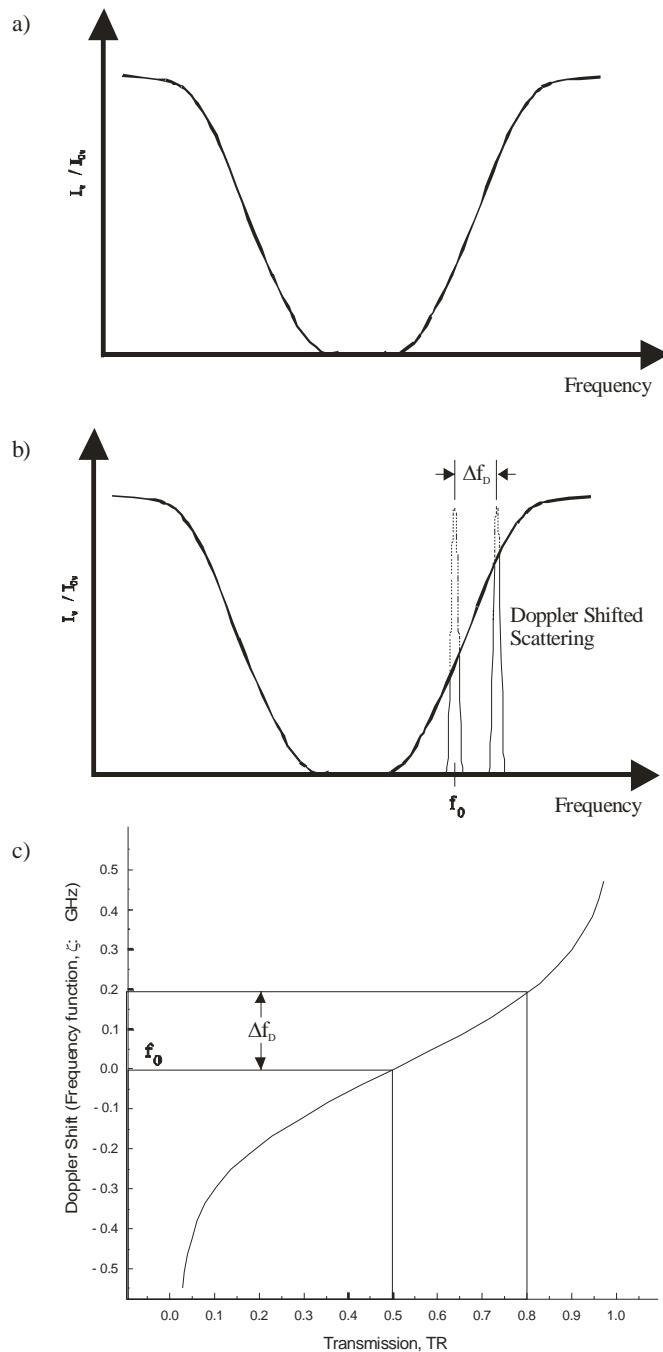
Transmission, TR

Figure 1.2 Schematic of intensity spectra of PDV process showing the (a) transmission profile of
the atomic/molecular filter, (b) laser and Doppler shifted signals with transmission
profile, and (c) frequency function

8

$\vec{V}$

k_o - k_i

Ω

Observation Unit vector, $\underline{k}_o$

φ

k_i Incident Light Unit vector, $\underline{k}_i$
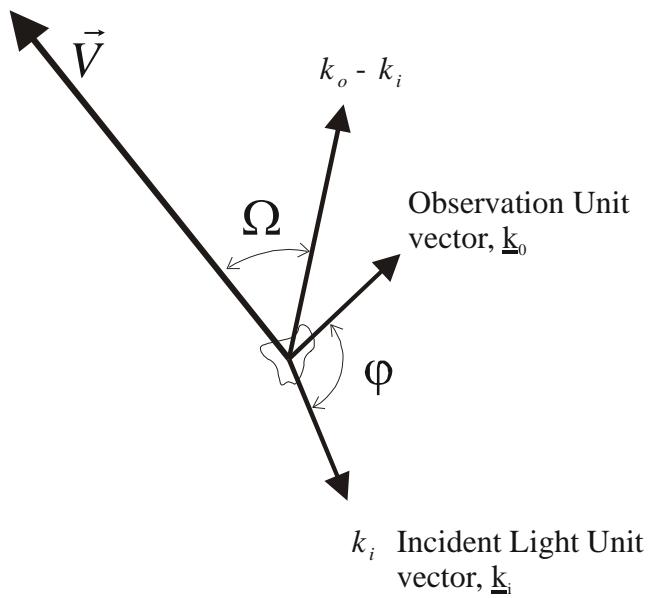
Figure 1.3 Vector relationships of incident and scattered light and the measured velocity component.

Laser Sheet (Double Pulse Nd:YAG)

Frame Transfer Camera
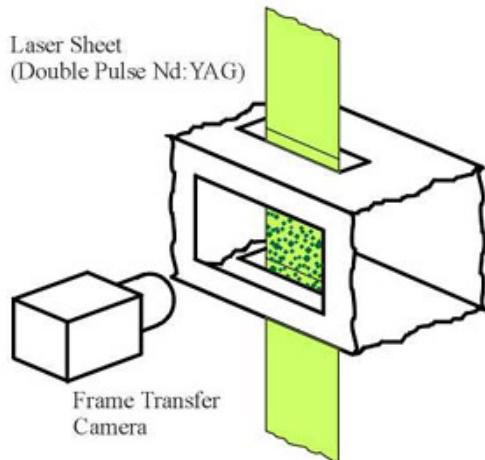
Figure 1.4 Typical arrangement for Particle Image Velocimetry
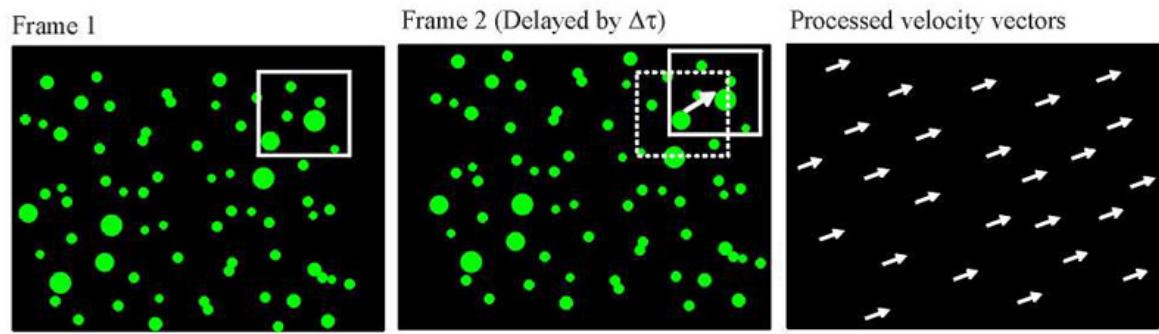
Figure 1.5 Schematic of initial and delayed PIV images and processed vectors.

2. The PDV System

The PDV system which was developed as part of the SBIR program is shown schematically in Figure 2.1. The four main components are the laser and sheet forming optics, the iodine filters, the laser frequency monitoring and cell calibration system, and PDV receiving optics and cameras.

2.1. The Laser and Sheet Forming Optics

Frequency-doubled Nd:YAG lasers (Spectra Physics GCR series) were used in the current experiments which were injection seeded with OEM or Lightwave seeders (note there is a large variation in the stability of each seeder and it was found that having external cooling water option had the great effect on seeding stability). The Nd:YAG lasers used in these experiments perform similarly, operating at a repetition rate of 10 Hz with a pulse duration of about 10 ns and energy per pulse in excess of 300 mJ. With the injection seeding, the laser produces a narrow linewidth pulse (~ 140 MHz) whose center frequency can be tuned over a range of 70 GHz by applying a bias voltage to the seeder. In addition the Build-up reduction time (BUT) voltage can be monitored to determine if the laser is seeding properly. In order to improve the stability of the laser frequency (particularly in a noisy large wind tunnel environment) the laser was supported on pneumatic vibration isolators, which was necessary since even the acoustic noise can have a detrimental effect on the ability of the laser to seed properly. The tunability of the laser and its narrow linewidth are important so that the interrogating laser light can be set to a precise location within the absorption spectrum of the iodine filter. Figure 2.2 shows the iodine absorption lines within the tuning range of the current laser system. The absorption line used for most of the experiments in this study was at 18789.28 cm^{-1} and is indicated in the figure. A combination of a spherical lens and a cylindrical lens formed the laser output into a thin sheet that defines the PDV measurement plane.

The Nd:YAG laser is a relatively stable platform; however, it is characterized by two features that complicate PDV implementation. First, its long term frequency drift and pulse-to-pulse fluctuations necessitate a frequency monitoring system (wavemeter), which is described below. Measurements with the current frequency monitoring system indicated that the standard deviation of the laser frequency was 11 MHz in a laboratory environment and 41 MHz in the

large scale (SARL) wind tunnel. This higher level of fluctuation in the latter experiments, in which the laser rested on top of the wind tunnel, was attributed to a higher level of vibration and acoustic noise.   Without accounting for these frequency fluctuations, spurious velocity fluctuations would be measured in the flow. In general as much vibration isolation should be used as possible through mounting the laser on a foam pad or as was done in later experiments mounting the laser on a table which is suspended on air pads. Second, several investigators have reported a chirp, or spatial variation in frequency, for the Nd:YAG laser of up to 150 MHz.[14,15] One solution to this problem is to use only the center of the laser profile which has been reported to reduce the variation to less than 4 MHz[14]. Alternatively, this chirp could be accounted for by calibration, assuming that it is steady from pulse to pulse. The low level of the chirp in the current experiments was confirmed in empty tunnel tests where no spatial gradients in the frequency were observed. Recently, it has been found that a major source of chirp is related to misalignment of the seeder within the host laser platform and thermal gradients within the Nd:YAG rods.

2.2.   The Iodine Filters

During the course of the development effort, one of the key aspects to the system was the ability to control the absorption profile of the iodine filter. The final filter design is shown in Figure 2.3. The iodine filters used in the current set of experiments were generally, 7 to 8 cm in diameter and from 12 to 25 cm in length, with flat optical plates at each end. Two different types of iodine filters were developed for the final system. Both arrangements are a starved iodine design where only iodine in the vapor state was contained in the cell body. This arrangement ensured that no communication with solid iodine could cause the number density of the vapor to change with temperature, which results in unstable absorption lines. The first arrangement, Figure 2.3, has a small side arm and a cold tip extend from the cylindrical body. Iodine crystals are placed in the filter, which was then evacuated. The cylindrical portion of the cell was wrapped with heating tape and insulation and maintained at 105°C via a closed-loop temperature controller (i.e. Cole Parmer DigiSense Model Number 89000-01). The side arm, which is connected to the body of the cell, was generally maintained at a lower temperature (40° to 50° C) using a constant temperature water bath. After solid-vapor equilibrium was established in the side arm, a valve was closed shutting it off from the body of the cell and fixing the number

density of the iodine in the cylindrical portion of the filter. Such a filter is termed a starved cell because all of the iodine is in a gaseous state. If there was no further need to change the absorption line profile for the cell, a system was developed so that the glass could be permanently welded shut before the valve to insure that the absorption profile would never change. This is termed a permanently sealed cell.

In addition to the iodine vapor, it is possible to introduce a small amount of nitrogen (~20 Torr) to pressure broaden the cell and increase the range of measurable frequency shifts. The nitrogen was added after forcing essentially all of the iodine into the solid state by submerging the cold tip in a dry-ice acetone bath. When the nitrogen was added, the pressure measured using a Baratron vacuum gage was almost entirely due to the nitrogen since the iodine was in solid form. Once the desired pressure of the nitrogen had been set, the cold tip was reheated to the cell temperature. After equilibrium was established, the side arm was shut off from the filter body, creating a pressure-broadened starved cell.

Figure 2.4 shows the effect of variations of three cell conditions: partial pressure of nitrogen, filter sidearm temperature, and filter cell temperature. These profiles have been normalized by the intensity ratio measured with no iodine present in the cell; thus, they show the variation in continuum absorption (non-resonant) as well as the variation in the line-shape. Figure 2.4a shows the effect of the partial pressure of the nitrogen on the absorption profile of a cell with a body temperature of 100°C and a sidearm temperature of 40°C. Pressure broadening is clearly evident as the nitrogen pressure is increased from 5 torr to 80 torr. This broadening allows the frequency range of the sloping region on the cell to be adjusted for a given velocity range. Figure 2.4b shows the effect of the side arm temperature (or iodine number density) on the absorption profile with no nitrogen present and a body temperature of 100°C. Five degree centigrade increments in sidearm temperature alter the cell performance dramatically. Therefore, in a saturated cell it is important to control the temperature of the coldest point in the cell precisely. The extent to which variations in the side arm temperature can affect velocity measurements will be addressed in the error analysis. Figure 2.4c indicates that the temperature of the cell body is not as important as the side arm temperature since the profiles overlie one another for a range of cell temperatures from 100°C to 140°C. These measurements were made with no nitrogen present and a sidearm temperature of 40°C. The chief reason for keeping the

cell at an elevated temperature is to prevent iodine condensation anywhere other than the sidearm.

2.3.   The Laser Frequency Monitoring System (Wavemeter)

A laser frequency monitoring system (termed a wavemeter) was developed to compensate for the jitter and drift in the Nd:YAG laser about its set point and calibrate the various iodine filters used in multi-component experiments.   The basic idea behind the wavemeter which was developed for PDV measurements was to measure the transmission of a small portion of the laser light through a second iodine filter, termed the reference filter, for each laser pulse. If the iodine filter absorption profile is stable then the frequency of the laser can be calculated for each laser pulse (with a knowledge of the absorption profile frequency function). The initial frequency monitoring system utilized photodiodes from which the signal was integrated utilizing Stanford Research Systems Boxcar Integrators as shown in the schematic of Figure 2.1. This system was further refined and improved to utilize Joule-meters as shown in Figure 2.5 providing a more portable system.

The frequency measurement is initiated by utilizing a small portion of the laser beam, which is reflected from the first surface of an optical wedge. The laser beam is then passed to a two inch diameter integrating sphere from Orial so that light from the entire beam profile is averaged together before being launched into a 400 micron optical fiber. The optical fiber is sent to the portable wavemeter detection system where the light from the fiber is expanded and collimated to a 25 mm diameter with a negative/positive lens pair. This allowed a substantial quantity of light to be sent through the filter without saturating the transition. To ascertain if the transition was saturated, measurements could be compared with a neutral density filter inserted in the beam path before the filter and after the filter. If the former measurement showed greater attenuation than the latter, the filter was saturated and the irradiance of the beam needed to be reduced. Two successive beam splitters then split the laser light into three beams. One beam is sent though the reference filter, the second is sent through a camera filter (during a test this position is left empty) and the third beam provides the intensity reference for the transmission calculation. Neutral density filters can be placed in each separate beam so that the detectors are not saturated however this is unnecessary when using the Joule-meters. The Joule-meters provide "onboard" integration of the signal. They also have an extremely low detection limit and

a linear dynamic range of about five orders of magnitude. This allows accurate measurements of the iodine absorption profiles. The Joule-meters are controlled through a GPIB interface which is directly connected to the GPIB card on the Master computer.

The need and quantification of the frequency monitoring system was demonstrated by measuring empty tunnel flow in the wind tunnel facility. The turbulent fluctuations in the tunnel were expected to be less than 0.1% resulting in a Doppler shift fluctuation of less than 0.5 MHz. Figure 2.6 shows a plot of the frequencies recorded by the monitoring system for 66 laser pulses utilizing the boxcar integrators and photodiodes. The spatially averaged Doppler shifted frequencies measured by the PDV cameras for the same 66 laser pulses are also shown on the plot. Note that the frequency of the laser fluctuates dramatically due to tunnel noise and vibration (rms variation equal to 41MHz). However, the difference between the PDV frequency and the laser frequency remains relatively constant (equal to the Doppler shift induced by the approximately uniform flow). The standard deviation of the difference is less than 4 MHz. This is an incredible achievement considering that this is less than 4% of the linewidth of the laser.

2.4.   The Cameras and Receiving Optics

Three PDV camera systems were packaged as shown in Figure 2.7 so that they could be moved to the various viewing angles used for each test. Each system consisted of a polarizer followed by a 7.6x7.6 cm cube beam splitter providing separate optical paths to two 16-bit back-illuminated Pixel View CCD cameras, SpectraVideo Model SV512 VI(C/A PFT95). These cameras were generally fitted with Nikkor lenses (i.e. 85 mm or 105 mm). The f-number of the lens was set as low as possible to reduce laser speckle but high enough to keep the entire field of view in focus (f# = 2.8 to 5.6). The purpose of the polarizer was to reduce polarization-dependent variations which might occur in the flow field and through the optical system. Scattering from the flow field mostly preserves its polarization whereas scattering from solid surfaces is nearly entirely depolarized. Therefore, one effect of the polarizer was to reduce the background intensity relative to the signal intensity. Permitting only one polarization to pass into the receiving system ensured that variations in the transmission ratio were not caused by any polarization dependencies in the subsequent optics. The purpose of the beam splitter was to ensure that the viewing angles of the signal and reference cameras were identical. This is particularly important when the seed particles are relatively large (in the Mie regime) resulting in

15

a strong angular dependence in the scattering intensities. The signal camera viewed the flow through a molecular iodine filter and the reference camera viewed the flow without a filter. A four inch diameter flat mirror ($\lambda/4$) is used to orient the image onto the reference camera and allow for both signal and reference optical paths to be approximately equal. A 20.4 cm starved iodine cell is placed in front of the signal camera for all PDV components. This cell is set at a temperature and pressure that is optimized for the flow being studied. The body of the cell is again elevated in temperature using heat tape and controlled by a Digi-sense temperature controller. Neutral density filters were placed in front of each reference camera so that it had approximately the same intensity as the signal camera. This insures that one camera is not saturated while the other is at a low intensity. High and low pass optical color glass filters are also placed in front of each camera lens (creating a broadband notch filter) to reduce effect from background ambient light. The cameras are aligned during the test so that they have approximately the same field of view. Care must be taken during camera alignment so make sure that the cameras are centered in all the optics, the camera lenses are approximately the same distance from the CCD and perpendicular to it, and they are located approximately the same distance from the beam splitter cube. The iodine cell was easily removable so that it could be calibrated during the tests. Camera exposure times were set to 50 ms. It should be remembered, however, that the measurement time scale was set by the duration of the laser pulse (10 ns) rather than the camera exposure time.

Each of the PDV reference and signal camera systems was controlled by a single computer. Two of the computers operated as slaves and were networked into the third computer which operated as the Master. For the multiple component tests, the Master computer not only controlled the slave systems but also collected and stored all the images (reference and signal) from each sub-system. In addition to controlling and collecting all the image data from the cameras, the Master computer also collected, controlled, and monitored the laser frequency using the previously described wavemeter. A user defined logfile would then be created for each test. This file included the file name of each image, camera/image information, input frequency offset voltage to the laser, readings from the frequency monitor photodiodes, and information about the type of data which was taken. The data collection program will be described in more detail shortly.

It should be noted that other investigators have combined both signal and reference images onto a single CCD chip. This was avoided in the present case. Two cameras for the one-component PDV system were used rather than a single camera for two reasons. First, splitting the image on a single CCD chip, as is required in the one-camera arrangements, reduces the resolution by a factor of 2. Second, image-splitting invariably results in some image overlap, particularly as the f-number is lowered to minimize laser speckle and this leads to erroneous velocity measurements.
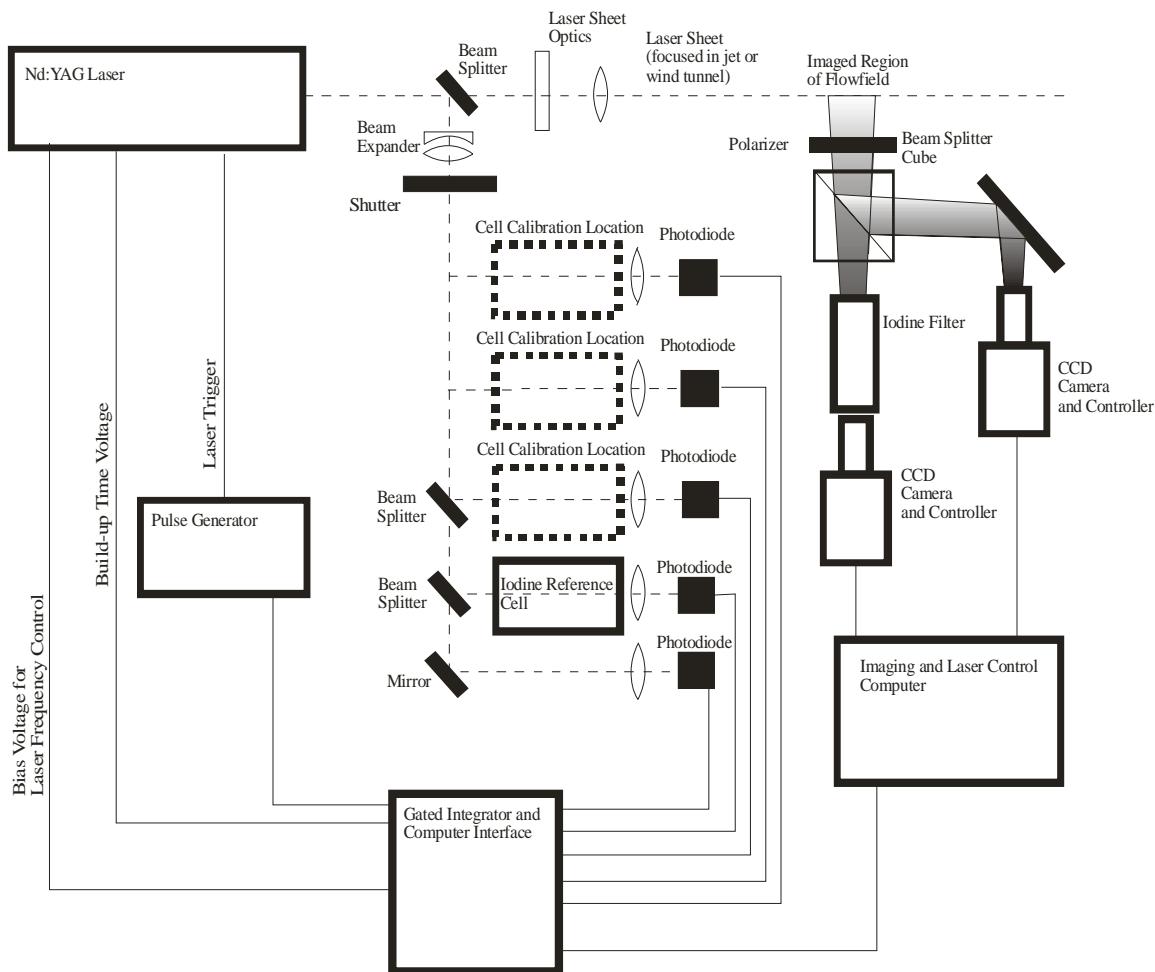
Figure 2.1 Planar Doppler Velocimetry experimental arrangement.
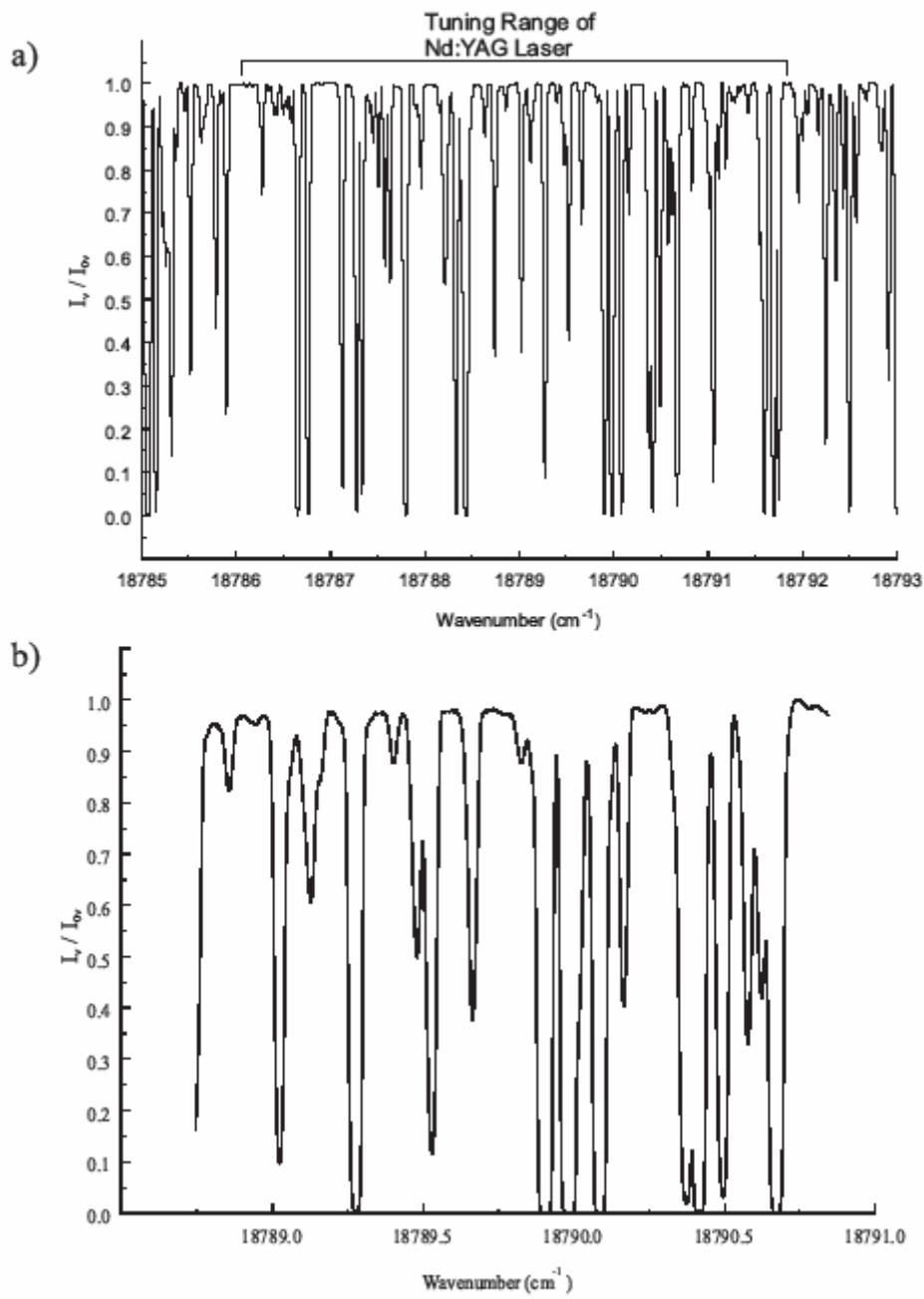
Figure 2.2 Absorption lines of Iodine in the visible wavelengths frequency region accessible by (a) Nd:YAG laser as calculated by the model of Forkey (1996) and (b) the experimentally measured spectra using a the Nd:YAG laser iodine cell calibration system.
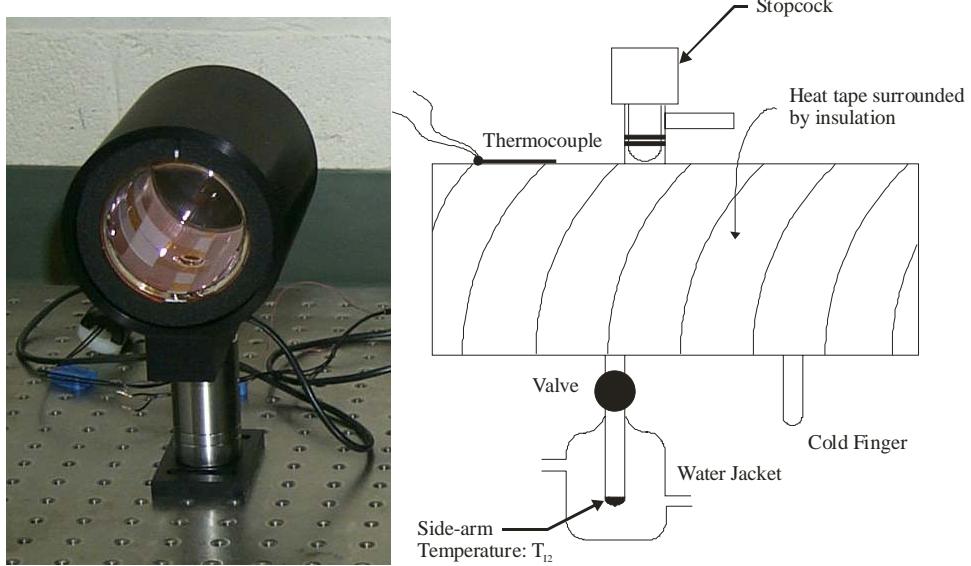
Figure 2.3 Typical iodine filter (cell) configuration.
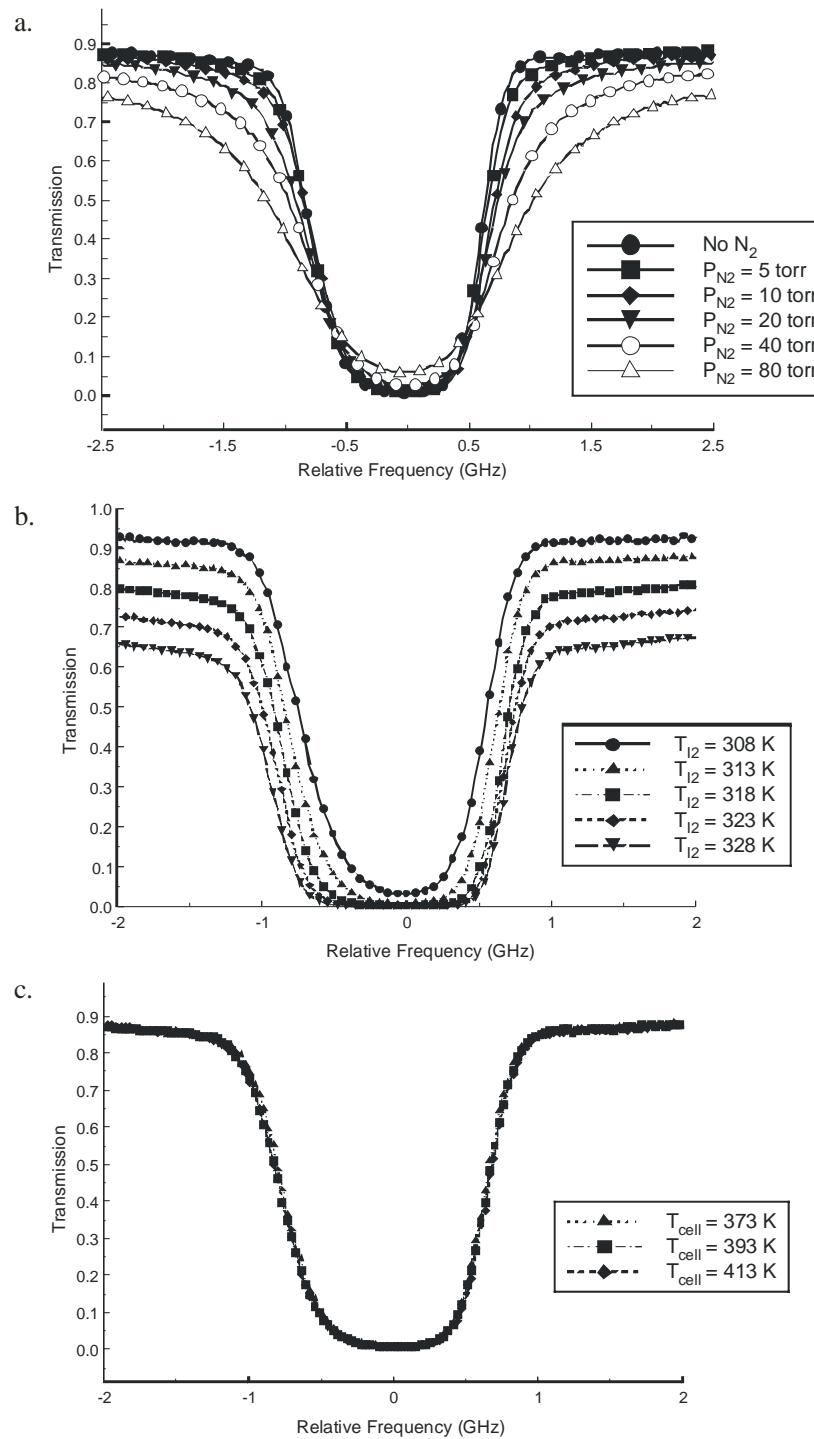
Figure 2.4 Effects of cell conditions on filter performance. Nominal conditions are 373 K body temperature; 313 K side-arm temperature, and no buffer gas. Varied conditions are (a.) partial pressure of nitrogen; (b.) temperature of side-arm; and c.) temperature of filter body.
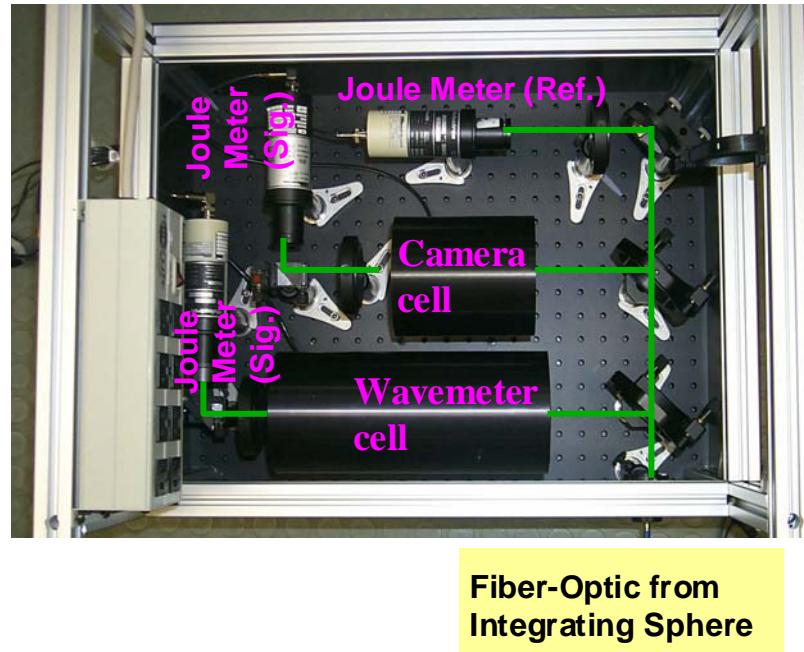
Figure 2.5 Final wavemeter system developed for laser frequency monitoring and iodine cell calibration.
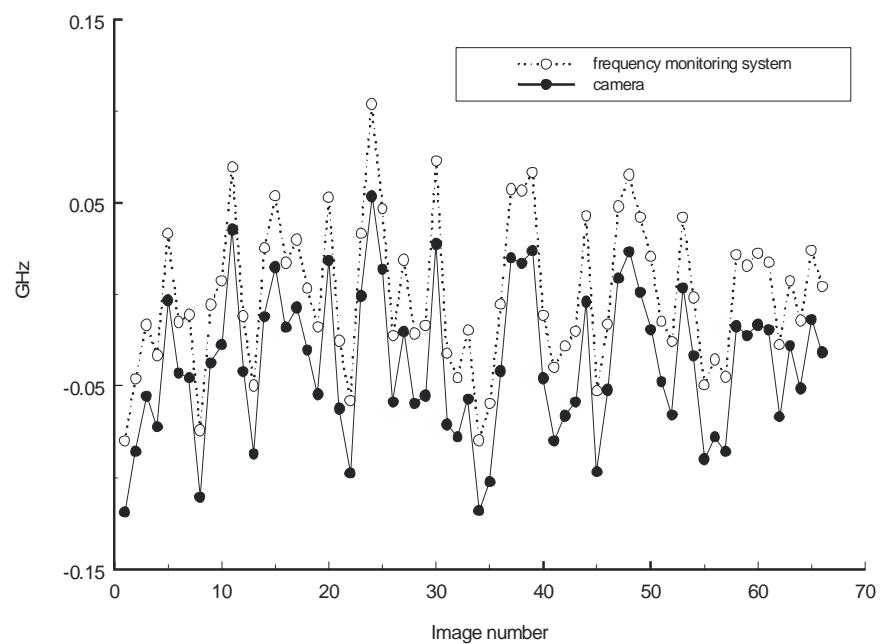
Figure 2.6 Frequency for 66 laser pulses as measured by the frequency monitoring system and by the PDV camera system in a uniform Mach 0.2 flow.
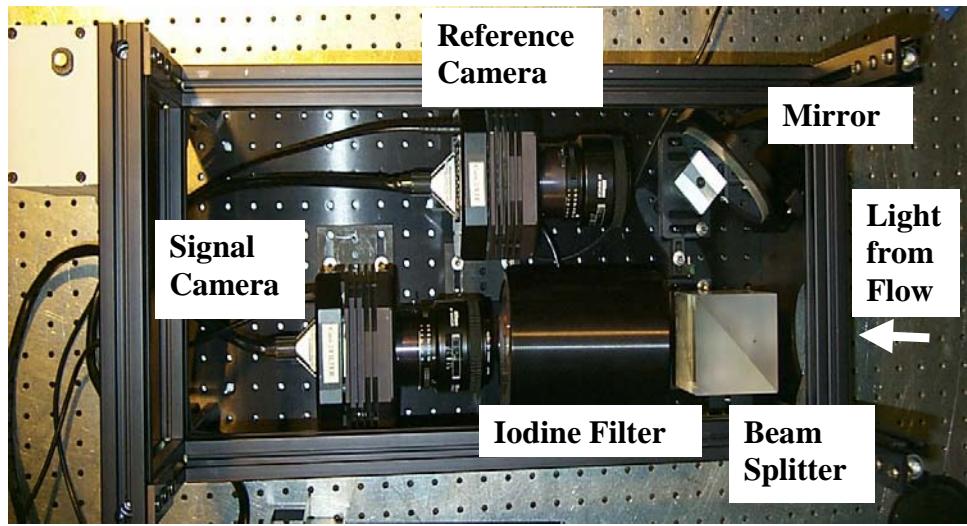
Figure 2.7 Detector box for PDV system.

3. PDV Methodology

Implementation of PDV in a facility requires the calibration of the system components and collection of the velocity data. Some aspects of the system calibration must be performed in-situ. Both the calibration and data collection process require that the user carefully monitor and record an extensive set of information. Several PC based data acquisition programs have been developed to facilitate this process. In the following section, the system calibration and data collection will be described. Following this, a short description of the data acquisition programs is given.

3.1.   System Calibration Data Collection

Before collecting the actual PDV images to convert to velocity, a significant aspect to PDV is the collection of data to calibrate the system. The calibration consists of three types of data which need to be collected; 1) calibration of the iodine cells, 2) spatial calibration of all of the cameras together (also termed image mapping) and 3) intensity calibration of the signal and reference cameras so that they can be used to determine the transmission ratio. Following is a description of how the data for these calibrations is obtained and general recommendations in taking the actual PDV images to measure the velocity. Table 3.1 gives a summary of the basic data collected for any PDV test.

3.1.1.   Calibration of Iodine Cells

Multiple iodine cells are needed in the current PDV system, one in front of the signal camera for each velocity component and one in front of the signal photodiode of the frequency monitoring system. The cell conditions (sidearm temperature, body temperature, and partial pressure of buffer gas) were set according to the expected velocity ranges. Before flow field measurements were made, the cell that was to be in front of the signal cameras during flow measurements was moved to its calibration location as seen in Figure 2.5. Iodine filters can be calibrated one at a time or if additional calibration stations are available, they can be calibrated simultaneously using the same laser pulses. Calibration consisted of scanning the laser frequency while measuring the transmission of the iodine cells. The laser frequency is controlled by a bias voltage applied to the seed laser by the master computer. Transmission was measured

in terms of the voltages recorded from the photodiodes connected to boxcar integrators. These were later replaced by the more compact Joule-meters. In either case, the raw data from the calibration consisted of four signals. The laser bias voltage v_s, which was varied over the desired frequency range of the filter scan, is recorded. The unfiltered signal from the Joule-meter (or boxcar integrated photodiode), v_u, and signal measured after the camera filter and the reference filter, denoted by v_c and v_r respectively, measured from a Joule-meter (or boxcar integrated photodiode) were also recorded. Each data point recorded in the computer from the Joule-meters during a calibration scan represented the average of 10 to 50 pulses. The BUT voltage is also monitored and the data point was not saved to the file unless the BUT is within the range of seeded operation.

Before these ordered pairs of data could be used, the abscissa needed to be converted from units of voltage to units of frequency. This conversion was performed through the laser tuning coefficient, which is the constant of proportionality relating the bias voltage applied to the seed laser to frequency. This constant is defined as the change in frequency per unit change in bias voltage. This constant can be found by recognizing the spectral features of iodine in a calibration scan and comparing their separation in terms of voltage to their known separation in terms of frequency. Figure 3.1 give a typical comparison of the experimental and theoretical transmission profiles.[16] The voltage per frequency for this test was found to be -1.192 GHz/VDC. An alternative way to obtain the laser tuning coefficient is to pass a portion of the beam through a Fabry-Perot etalon during the scan and record the separation in voltage between adjacent transmission maxima. Note that individual lasers have different tuning coefficients and can be either positive or negative, depending on the type and settings of the injection seeder. Also tuning toward the end of the range the frequency per voltage coefficient may not be linear so this should be avoided.

Once the tuning coefficient is determined, a fine scan may be performed of the particular spectral feature to be used for velocity discrimination. Normally, only the approximately linear portion along one side of the absorption line is used in a PDV experiment. Figure 3.2 shows an example of the transmission profiles used in a typical experiment. This is a detail of the absorption line indicated in the broad scan of Figure 2.2. The low-frequency side of the line, which possesses a shallower slope than the high-frequency side, was generally used in the jet experiments (due to the inherently higher velocity). The high frequency side of the line, which is

steeper, was generally used in the wind tunnel experiments. Modification of this profile was sometimes conducted by adding nitrogen and pressure broadening the profile. This modification was made to increase the range and sensitivity, respectively, for jet and wind tunnel experiments. The experimental method outlined above resulted in transmission curves for the camera filters and the reference system filter, having a common abscissa (relative frequency); however, the ordinates of these curves were independent of one another. Differences in the performance of the beam splitters, the optical paths, and the boxcar gains meant that the voltage ratios representing the transmission of the filters had undetermined scales. Each curve was normalized using the maximum transmission ratio within the range of the scan. Thus, normalized transmission ratios were defined by

$$S_{c12} = \frac{\frac{v_c}{v_u}}{\left(\frac{v_c}{v_u}\right)_{max}} \qquad\qquad \text{Equation 3.1}$$

and

$$S_r = \frac{\frac{v_r}{v_u}}{\left(\frac{v_r}{v_u}\right)_{max}} \qquad\qquad \text{Equation 3.2}$$

These normalized curves resulted in transmission ranges that varied from approximately zero to unity. Thus, two transmission curves were obtained: one curve was for the camera filter and one was for the frequency monitoring filter. Inverting these curves produced relative frequency plotted against transmission ratio. This is perhaps the natural way to think of these functions for PDV, with transmission ratio as the independent variable and frequency as the dependent variable. These functions are denoted ζ_c (S_{c12}) and ζ_r (S_r) for the camera and reference filters, respectively. The former function is used to establish the shifted frequency of the light scattered into the PDV optical system at each pixel. The latter function is used to establish the frequency of the unshifted light pulse before it is scattered. As an example, Figure 1.2c shows the frequency function used in a typical PDV experiment.

3.1.2. Spatial Calibration of Cameras (Image Mapping)

In order to make accurate PDV measurements, several images are needed for a spatial calibration of the cameras. First are dot card images which are used to spatially line up the images from the signal and reference cameras on a pixel by pixel basis. A physical dot card with

equally spaced circular or rectangle dots is placed at the location of the light sheet where the flow velocity will be measured. Generally this is accomplished by turning the laser sheet on and aligning the dot card so that it skims the surface. The size of the dots should be large enough so that they take up a few pixels (4-8) and spaced far enough apart so that the centroids can be distinguished without interference from neighboring dots. A transparent film for the dots it can easily be viewed from either side, this will reduce the number of calibration shots which are needed. Each image pair provides a reference and signal image for that component. Even with poor illumination, the processing programs are able to accurately pick out the centroids. Generally 5 to 10 dot card images are taken and averaged together to decrease noise as much as possible.

3.1.3. Intensity Calibration of Cameras

The second calibration data shot is used to calibrate the intensity. These are termed green card images. When taking these intensity calibration shots the laser is tuned to a region of the iodine absorption profile which has a flat maximum transmission (frequency of 0.5 in Figure 3.2 note that the ratio of the filtered and unfiltered reference photodiodes at this frequency is used to correct the frequency monitoring system). Laser light is used since there is always a slight amount of chromatic differences in the signal and reference optics which has been found to cause a calibration offset. There are three types of green card images which can be used for intensity calibration:

1. **Static Green Card:** To obtain typical green card data the laser is expanded onto a Mylar sheet which is used to illuminate diffusely a white screen placed over the dot-card. The goal is to provide as even as illumination as possible to all camera views. Background images are also taken with the laser off so that they can be subtracted from the green card images. The intensity of recorded by the camera can be varied by changing to intensity of the laser using neutral density filters or a better way is to simply increase the exposure time on the camera to capture more laser pulses. If this is done background images should be obtained for each exposure time. Generally, the intensity only needs to be varied a few (4) levels, but multiple images should be taken and averaged together at each level.

2. **Running Green Card Empty Tunnel:** Another method of providing intensity calibration images is to move the model out of the field of view and obtain images of the laser

sheet illuminating the smoke with the laser tuned away from the absorption line. The advantage of this method is that it can be conducted during the wind tunnel test and the scattering is the same as will be seen in the measurement. It should be noted that background images are needed for this type of running green card preferably with the laser on and no smoke. Generally many more images are needed in this case since the seeded flow field is not uniform and the smoke needs to be moved during the data acquisition so that there are several "good" points for each camera pixel. In addition care must be taken to insure that the Doppler shift caused by the flow does not shift the frequency of the light into the transmission profile of the iodine filter.

3. **Running Green Card with Model:** The final type of green card image is the running green card with model in place. This type of intensity calibration image is taken with the model in place and a seeded flow field with the laser tuned away from the absorption line. Again multiple images are need to cover the entire imaging region due to smoke variations and background images should be taken with the laser on and smoke off.   The advantage of the running green card with a model is that it is definitely the easiest to take since the laser just needs to be tuned outside the absorption line, but at conditions otherwise the same as the data. Unfortunately it may be difficult to obtain background images since the flow may have seeding from "natural" condensation and flow structures cause high intensity contrast edges, which greatly amplifies mapping inaccuracies causing intensity abnormalities in the calibration.

3.2.   PDV Data Collection

After the dot-card and green-card images are taken the actual PDV data is recorded. Generally the laser is tuned to approximately the 50% transmission region and the data shots are recorded. It is usually a good idea to vary the laser frequency slightly within this region. This is particularly true when multiple components are measured since one component may be tuned too far into or too far away from the absorption profile to provide useful results.   In addition, background shots should be taken with the laser on and no seeding. This background can be averaged and subtracted from the data.   Often in the large wind tunnel there is perpetual condensation signal from vortices which may occur due to the model geometry (i.e. a delta wing). If this occurs, the tunnel can be run at a slower speed so that the scattering from the condensation does not corrupt the background images.

3.2.1. Measurement of Observation and Incident Light Vectors

The final piece of information which is needed to convert PDV images into velocity components is the incident and observation unit vectors (for each PDV component). These vectors are defined in Equation 1.1. These vectors allow the calculation of the velocity components from a knowledge of the measured Doppler shift frequency. These vectors are determined by measuring the position of the each component of the system relative to the center of the dotcard in the tunnel. Presently the vector coordinates are obtained by measuring the PDV single/reference camera systems, laser position, and center of the dotcard relative to known locations on the wind tunnel. This should be done as accurately as possible since errors will propagate through all of the velocity measurements. The PDV single/reference camera locations are generally measured by placing a piece of tape on the window to cover the center of the dotcard when an image is taken. By measuring the position of the marker the vector can be obtained. In the future, it is hoped that better instrumentation can be used to improve and reduce the time required for this process. Perhaps by imaging a single target in the tunnel at several positions near the laser sheet and applying the principals of photogrammetry, an in-situ calibration could be accomplished.

3.3. Data Collection Programs

Implementation of PDV requires that the laser frequency be both controlled and monitored while simultaneously acquiring the signal and reference images from each component of the system. This data must be collected and stored along with notes concerning the experimental conditions so that the data can be properly reduced and analyzed. These tasks must be accomplished while maintaining the flow field of interest and providing adequate scattering particles to the flow. It should be clear that implementation of PDV, particularly in large facilities, is aided by automation of the data acquisition process. To this end, several data acquisition programs have been developed. The PDV Scan program is used to automate the process of scanning each Iodine cell that is used in the experimental setup. The PDV 5 program is used to control the data acquisition for a three component PDV system in an experimental facility. These programs provide a graphical user interface for configuration, control, and monitoring of the data acquisition hardware. As data is acquired, it is displayed on the user

interface and stored along with a log file that includes information concerning the experimental conditions and operator notes. These programs are described in the following sections.

3.3.1. PDV Scan

Multiple iodine cells are needed in the current PDV system, one for each velocity component and one for the frequency monitoring system. Before flow field measurements were made, each cell was calibrated. Calibration consists of scanning the laser frequency while measuring the transmission through the iodine cells. This process was automated to ensure that the scanning of the laser and recording of the voltages was performed consistently. The program used for purpose is PDV Scan. The program utilizes the SR245 computer interface to control and monitor laser operation and three Molectron Joule-meters to record Iodine transmission. The physical setup of the wavemeter and the process of converting the resulting scan to plots of frequency versus intensity are discussed in section 3.1.1 of this report. The incorporation of the hardware with the computer and the operation of the software will be described here.

The automated scanning system is composed of a series of electrical and communication connections. These connections are shown in Figure 3.3. The master PC is connected to the SR245 and the three Molectron Joule-meters through a GPIB bus. The SR245 is set to GPIB address 1 and the Joule-meters are set to address 4, 5, and 6. The laser frequency is controlled using a bias voltage applied to the seed laser. The bias voltage is provided by analog output channel 8 from the SR245. The laser pulse build-up-time is an indicator of single frequency operation. The build-up-time is monitored on analog input channel 1 of the SR245. Data acquisition is synchronized using the laser lamp pulse. This signal is connected to digital input 1 on the SR245. To ensure synchronous operation of the Joule-meters, they were armed over the GPIB bus and triggered by the laser using the lamp pulse.

Upon starting PDV Scan, the main panel of the program is displayed. This panel is displayed in Figure 3.4 and all controls necessary for acquiring a scan are located on the panel. By default, the system will initialize the SR245 and two Joule-meters. The Joule-meters are set to external trigger mode and a sensitivity of 200 mV. The user selects an output file by selecting the Output File button. This initiates a File-Select-Popup dialog. Any comments are entered in the comment field and this information is placed in the header of the output file. The starting voltage (Start), stopping voltage (Stop), and voltage step size (Step) for the scan are set and these

parameters are tied to the number of points (# of Points) in the scan. Each time the laser is stepped in frequency, the laser is allowed to settle before acquisition is continued. This parameter is set using the Settle Time control. The laser build-up-time is used to monitor single frequency operation of the laser. If the build-up-time voltage is below a set threshold, the laser is presumed to be operating at a single frequency. This threshold value is set using the BUT Filter control. Finally, at each laser frequency, a umber of points are acquired and averaged to produce an average transmission for the cell at that frequency. The number of points to be averaged is set using the # of Shots control.

The data acquisition process is outlined in Figure 3.5. With the scan parameters set, the scan is initiated using the Scan button. The laser is tuned to the starting frequency by setting the analog output voltage on channel 8 of the SR245. The program delays for a set time (Settle Time) to allow the laser frequency to stabilize. The program then proceeds to collect a predetermined number of shots (# of Shots) at this frequency. This loop is initiated and the PC then arms the SR245 to monitor digital input #1 for a trigger from the laser lamp. The lamp trigger precedes the laser firing by ~200μs. Upon receiving the trigger, the SR245 returns control to the PC. The PC then arms the system to acquire data on the next laser pulse. The PC arms the SR245 and the Joule meters for single-shot acquisition and waits for the next lamp trigger. Upon receiving the lamp trigger, the PC polls the SR245 to read the build-up-time voltage, the PC then reads the Joule meter voltages. The build-up-time voltage is compared to the BUT Filter voltage. If single frequency operation is indicated, the Joule-meter voltages are stored in a buffer. This process is repeated until the predetermined number of shots (# of Shots) are collected and stored in the buffer at this laser frequency. These shots are averaged to produce an average voltage from each Joule-meter at the laser frequency. The laser seed voltage and average Joule-meter voltages are appended to the Output File. The laser is tuned to the next frequency and the process is repeated until the scan is complete.

3.3.2. PDV 5

The PDV 5 program provides a graphical user interface for configuration, control, and monitoring of the data acquisition hardware. As data is acquired, it is displayed on the user interface and stored along with a log file that includes information concerning the experimental conditions and operator notes. The system may be configured for acquisition of one, two, or

three components of data. The optical components of the data acquisition hardware have been described in section 2 of this report. In the following section, a description of the electrical and communication connections of the system will be presented. Following this, the configuration of the data acquisition program will be reviewed, and a brief description of the program controls and menus will be given.

3.3.2.1. Electrical and Communication Connections

The configuration of a three component system includes a series of electrical and communication connections. The communication connections for a three component system are shown in Figure 3.6. Communication channels for the system include a GPIB bus, a local network, and several fiber-optic serial links. The PDV 5.0 program interfaces with a SR245 module and two Molectron Joule meters over a GPIB bus. The SR245 is configured at GPIB address 1. The signal and reference Joule meters are at GPIB address 4 and 5 respectively. Each component of the system communicates with two PixelVision SpectraVideo cameras. This is accomplished using a fiber-optic serial link between the camera and the Lynx PCI interface card in the PC. Finally, all machines are connected to a local network. The network hub supports 10/100 MegaBit communication and the machines are linked to the hub using RJ45 patch cables. The machines are identified by IP address. The master PC, which also controls the SR245 and Joule meters, is at IP 192.168.0.1. The slave PCs, which each control two cameras, are at IP 192.168.0.2 (slave 1) and IP 192.168.0.3 (slave2). The role of the master and slave PCs in the data acquisition process will be covered later.

Electrical connections provide a means of synchronizing the laser and data acquisition system, controlling the laser frequency, and monitoring the laser operation. The electrical connections are shown in Figure 3.7. Synchronization between the laser and data acquisition is accomplished by monitoring the laser lamp pulse on the SR245. The laser lamp pulse is connected to digital input #1 on the SR245. The laser build-up-time, an indicator of single frequency operation of the laser, is monitored using analog input channel 3 on the SR245. The laser frequency is set using the analog output voltage from channel 8 of the SR245. Finally, the camera shutters are gated by a TTL voltage from digital output #2 on the SR245.

3.3.2.2. Operation of the Data Acquisition Software

The role of the data acquisition software (PDV 5) is to interface with the data acquisition hardware and automate the data acquisition process. The process of initializing and using the data acquisition system using PDV 5 is described in the following section. Only the menus and controls that are necessary for this process are described. For a complete review of the menus and controls in PDV 5, the reader is referred to the online help in the program.

Upon startup of PDV 5, a pop-up panel appears where the user may select the components that are connected to the PC. The panel, shown in Figure 3.8, contains toggle switches for the SR245, the Joule meters, and the CCD cameras. The program will initialize all components that are selected by the user. The master PC will be connected to two cameras, the Joule meters, and the SR245. Each slave PC will be connected to two cameras. After initializing the selected hardware for each system, the main panel and main menu will be visible. Selecting the TCP Config menu reveals two options, Master and Slave as shown in Figure 3.9. First, configure the master PC by selecting Master for this machine. A dialog should appear indicating that the master PC has been registered on the network. Next, configure each Slave PC by selecting Slave for these machines. Again, a pop-up dialog will appear on the master PC indicating that Slave 1 and Slave 2 have been connected.

Upon registering as a Slave, PDV 5 will automatically initiate the CCD panel. This panel, shown in Figure 3.10, includes a canvas display for the Signal and Reference CCD images. Images acquired by the Slave PCs will be displayed on this canvas using an 8-bit bitmap. Next, the CCD&PD panel is activated on the master PC using the Control option from the main menu (Figure 3.11) and selecting CCD & PD. This will initialize the CCD&PD panel, shown in Figure 3.12. This panel includes controls for the SR245, the Joule meters, and data acquisition parameters as well as a canvas display for the Signal and Reference images from the cameras connected to the master machine.

3.3.2.3. Data Acquisition Using PDV 5

To begin data acquisition, the user specifies a set of parameters for the data set. These parameters include the seed-laser voltage, the build-up-time filter voltage, the number of images to be recorded, the target file path, the data type, and any user comments. These parameters can be set on the CCD&PD panel or loaded from a script file. These controls are located on the

32

CCD&PD panel (Figure 3.12). The operation of the controls and the format of the script file are described in the online help. The laser bias-seed voltage is set using analog output channel 8 on the SR245. The master PC delays a set time to allow the laser operation to stabilize. Once the acquisition sequence is begun, the master PC sends an arm command to all PCs over the network connection. The arm command clears the cameras and put them in externally gated, image acquisition mode. The master PC then arms the SR245 to monitor digital input #1 for a trigger from the laser lamp. The lamp trigger precedes the laser firing by ~200µs. Upon receiving the trigger, the SR245 returns control to the master PC. The master PC then arms the system to acquire data on the next laser pulse. The master PC delays for 50 ms to ensure that the preceding pulse has cleared. The master PC then instructs the SR245 to send a 50 ms TTL-low signal from the digital output #2 on the SR245. This pulse will open all camera shutters for 50 ms. The master PC then arms the SR245 and the Joule meters for single-shot acquisition and waits for the next lamp trigger. Upon receiving the lamp trigger, the master PC polls the SR245 to ensure that the build-up-time voltage have been recorded. The master PC then reads the Joule meter voltages used in the frequency monitoring system. After the camera shutters have closed, each system (master PC and each slave PC) will digitized and read the images from each camera. These images are stored in local memory and displayed as a bitmap on the local monitor. When these images have been read, the build-up time is checked against the threshold value that indicates single frequency operation. Assuming single frequency operation has been achieved, the master PC requests the stored images from each slave PC and reads these images over the network. At this point, the Joule meter voltages from the frequency monitor are written to a log file, which also contains the seed-laser voltage and a sequentially assigned image name for the current image set. The images from each sub-system are combined into a single file and saved to the master PC hard drive. The sequence is repeated until the desired number of images have been recorded. A flow chart outlining the data acquisition process is shown in Figure 3.13.
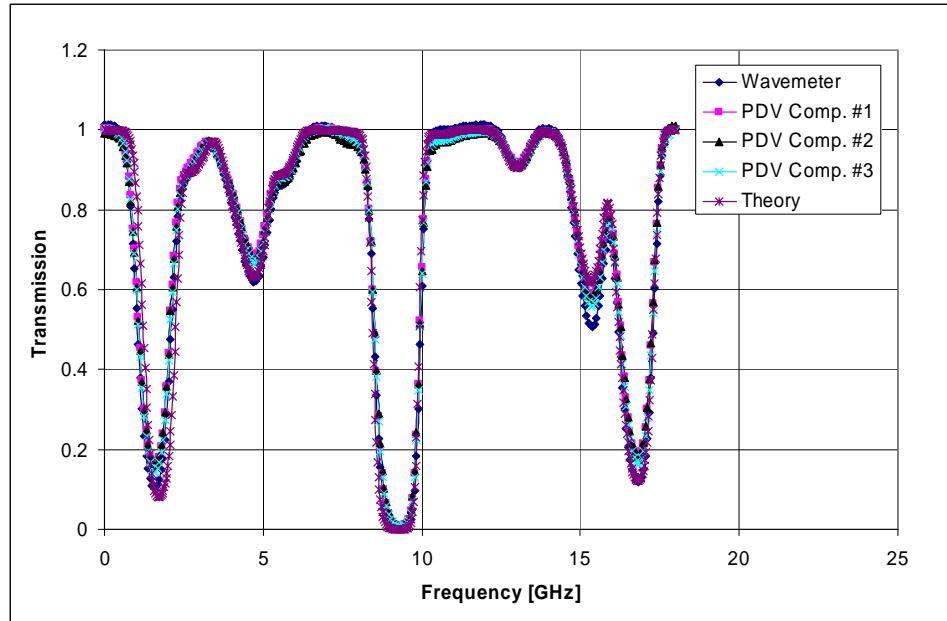
Figure 3.1 Comparison of theoretical and measured iodine absorption lines.
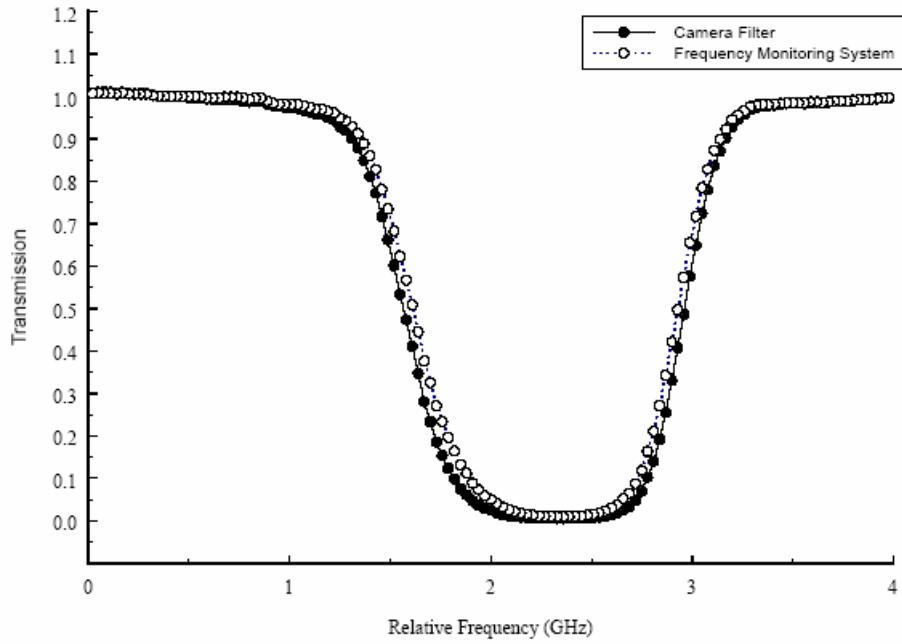
Figure 3.2 Detailed transmission profile of iodine filter for the camera and frequency monitoring
systems utilize in the jet and wind tunnel PDV measurements.
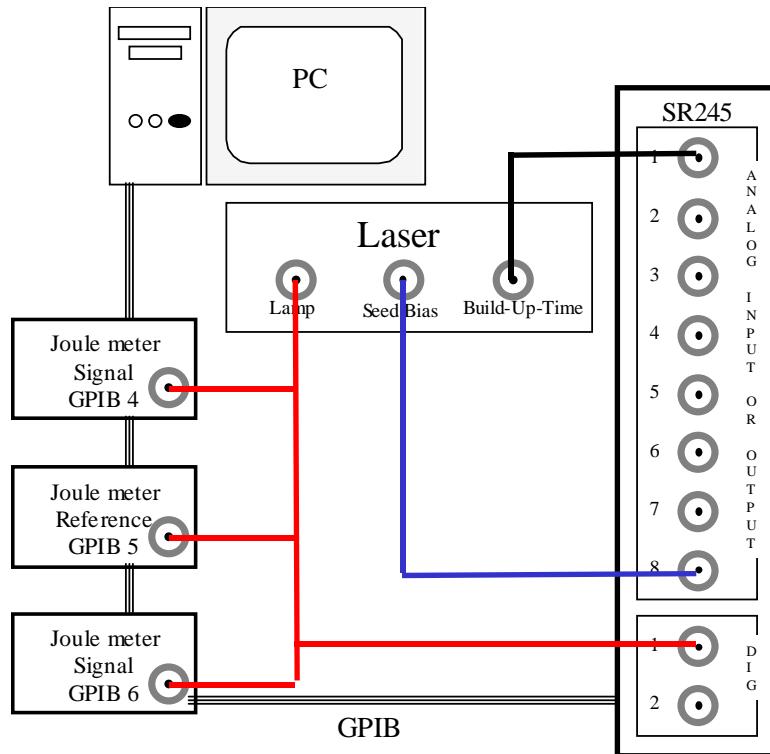
Figure 3.3 Electrical and Communication connections for the Iodine Cell Scan System.
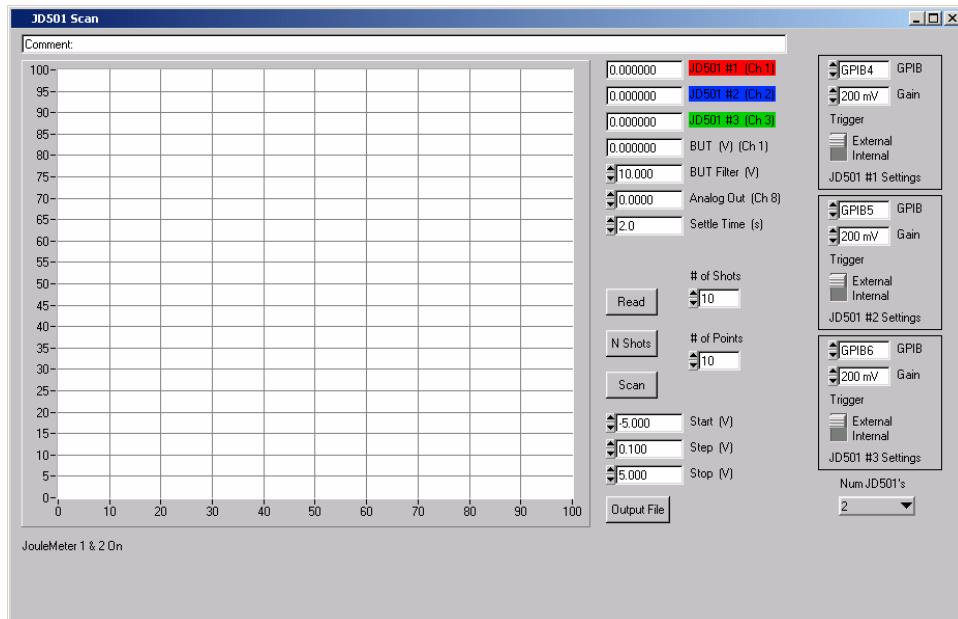
Figure 3.4 Main Panel of the PDV Scan Program.
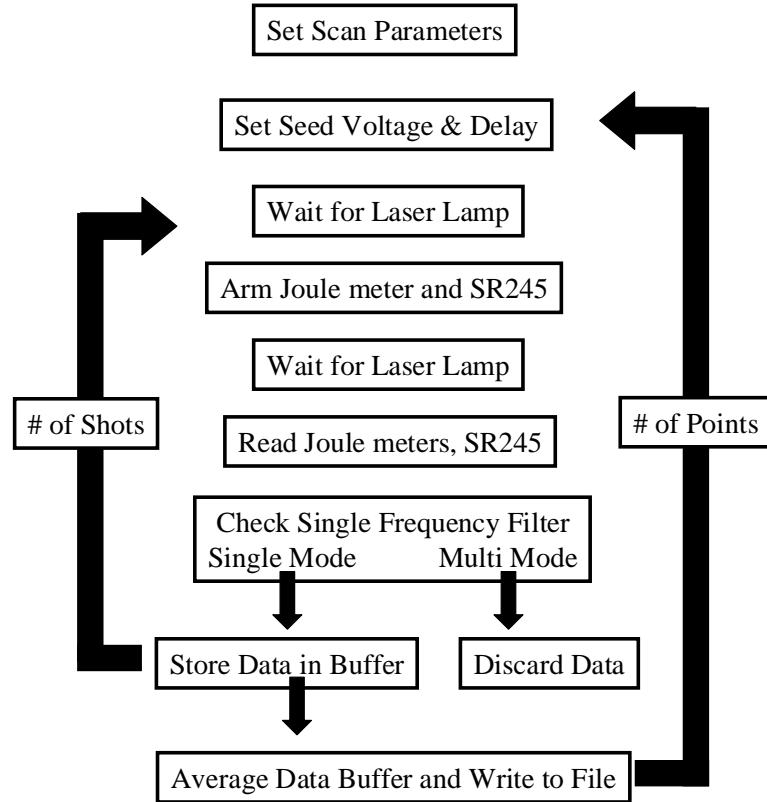
Figure 3.5 Outline of the PDV Scan data acquisition process.
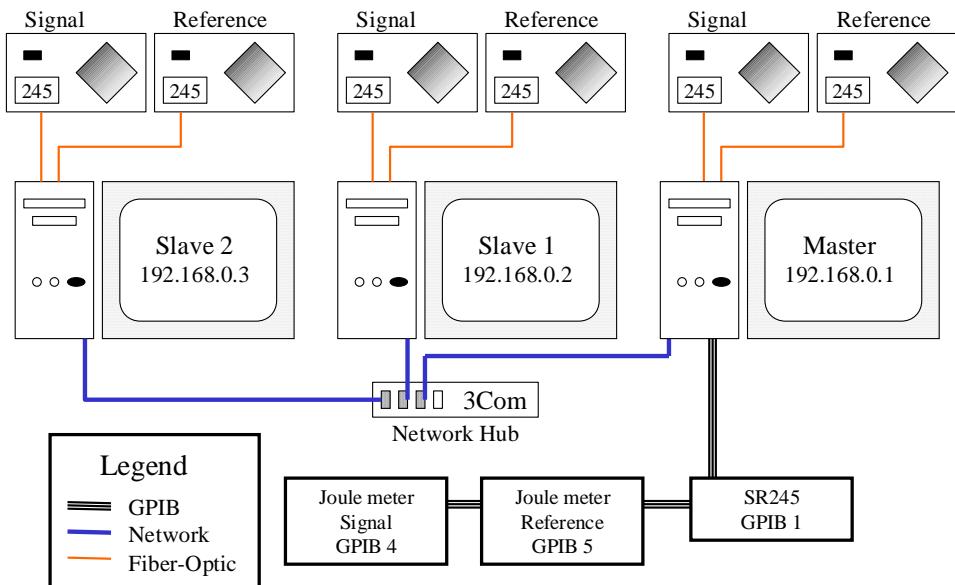
Figure 3.6 Communication connections for the PDV data acquisition system.
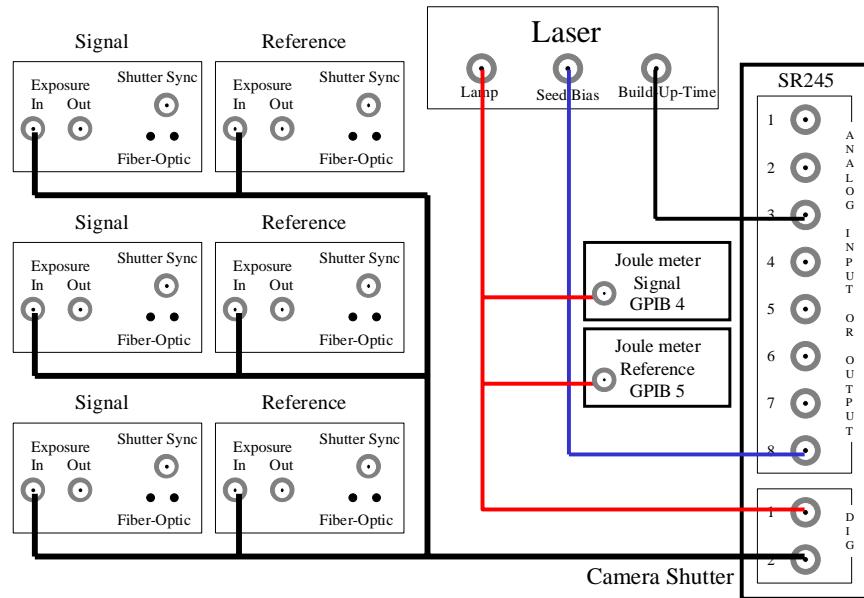
Figure 3.7 Electrical connections for the PDV data acquisition system.
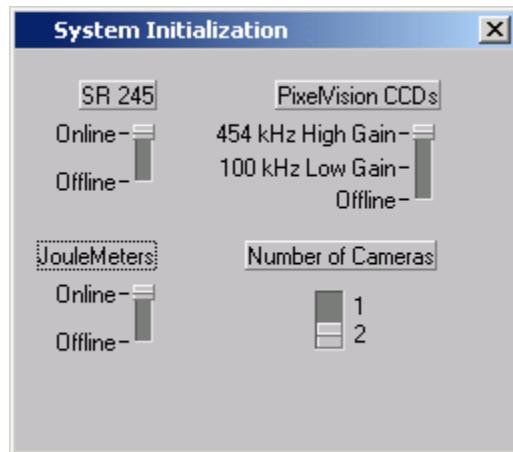
Figure 3.8 PDV 5 startup panel.
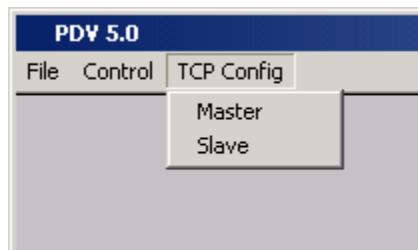
Figure 3.9 Master/Slave configuration option from the PDV 5 Main Menu.
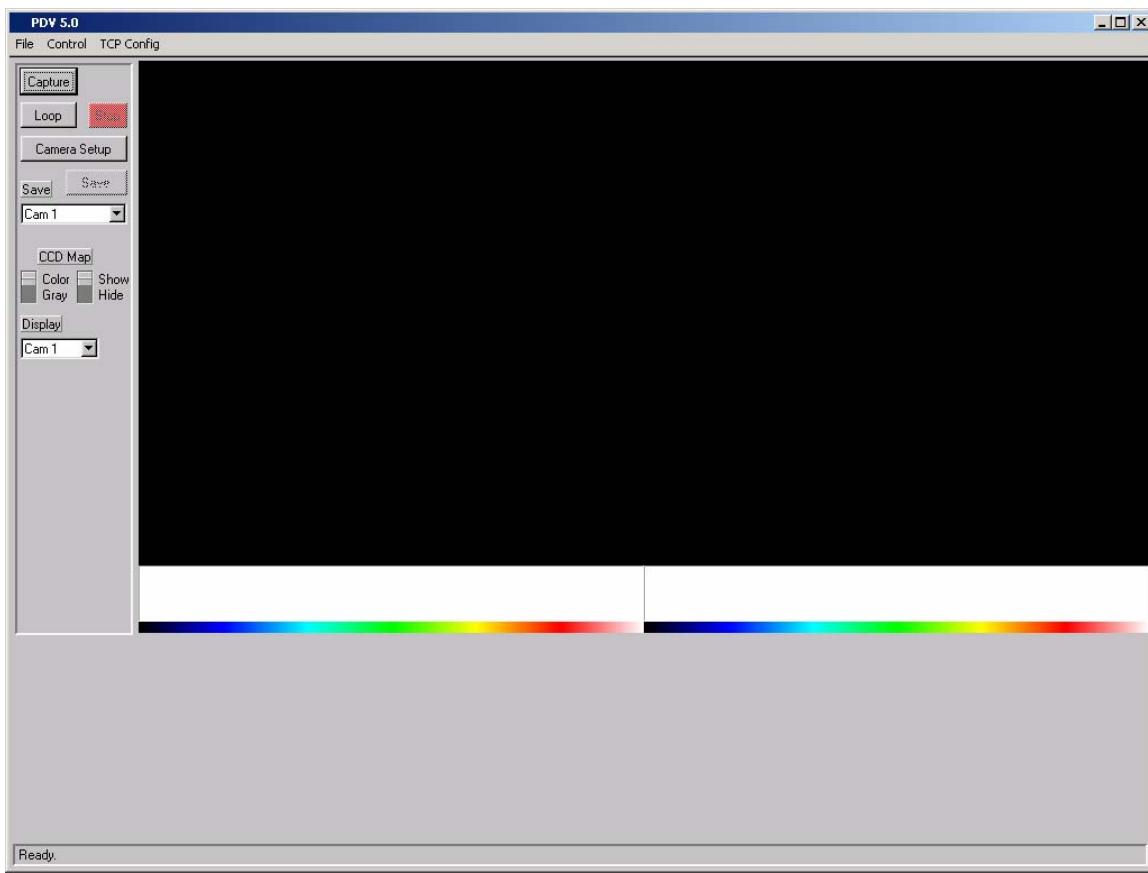
Figure 3.10 CCD control panel for Slave system operation.
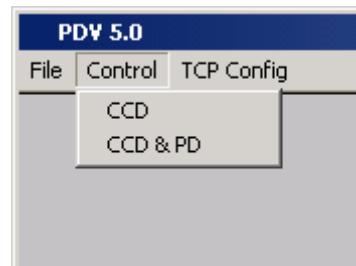
Figure 3.11 CCD&PD control option from the PDV 5 Main Menu.
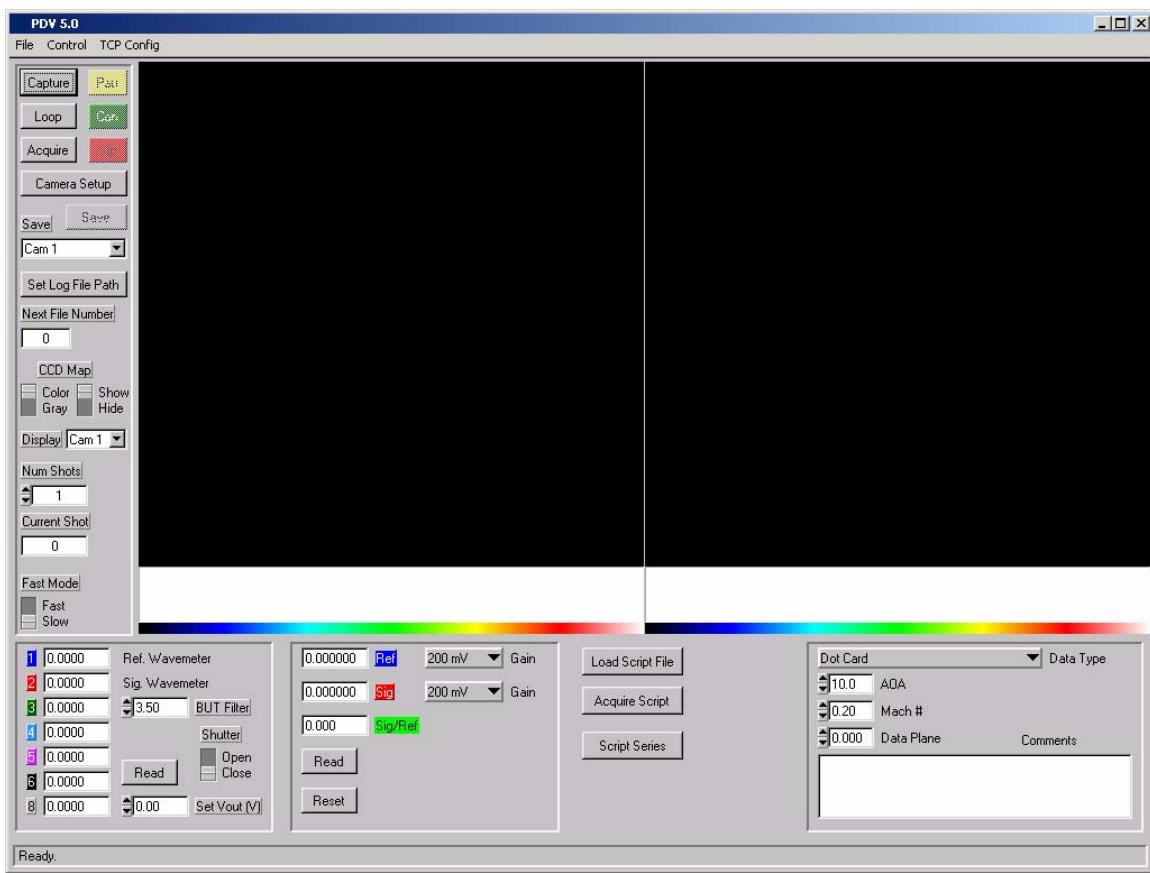
Figure 3.12 CCD&PD control panel for Master system operation.

```
┌──────────────┐      ┌──────────────┐      ┌──────────────┐
│ Load         │  ▶   │ Set Seed Voltage│  ▶ │ Arm Cameras  │
│ Acquisition  │      │   Delay 5 sec. │      └──────────────┘
│ Script       │      └──────────────┘
│ OR           │                              ┌──────────────────┐
│ Set          │                              │ Wait for Laser Lamp│
│ Acquisition  │                              │    Delay 50 ms   │
│ Parameters   │                              └──────────────────┘
└──────────────┘
                                              ┌────────────────────────┐
                                              │  Open Camera Shutters  │
                                              │ Arm Joule meters and SR245│
                                              └────────────────────────┘

                                              ┌──────────────────┐
                                              │ Wait for Laser Lamp│
                                              └──────────────────┘

        ┌──────────────┐                      ┌──────────────────────┐
        │ Display Images│ ◀────────────────── │ Read Joule meters, SR245│
        │ on Local Machine│                   │    Read Cameras      │
        └──────────────┘                      └──────────────────────┘

                                              ┌────────────────────────────┐
                                              │ Check Single Frequency Filter│
                                              │ Single Mode      Multi Mode │
                                              └────────────────────────────┘

                          ┌────────────────────┐        ┌──────────────┐
                          │ Read Images to Master│      │ Discard Data │
                          │ and Store Data       │      └──────────────┘
                          └────────────────────┘
```

Figure 3.13 Outline of the PDV 5 data acquisition process.

Data Type	Description and Purpose
Reference and Camera iodine filter transmission profiles	Transmission profiles are taken in the same range for all PDV signal camera filters and the frequency reference filter. Both a short high resolution scan used for image processing and larger frequency scan should be taken for the frequency/voltage calibration.
Dot card images	Images should be taken for all PDV signal and reference cameras of a uniformly spaced orthogonal dotcard for tie point determination and spatial alignment of all cameras.
Green Card Images	Images should be taken by each signal and reference PDV camera pair at varying intensities (created by varying the laser energy, exposure time, or seeding) of the laser light illuminating a card diffusely (termed a standard green card) or of the laser sheet in a seeded flow (running green card). The laser should be tuned far from any iodine absorption lines to insure there are no variations due to frequency.
Background Green Card Images	Background images should be taken for the green card images with the laser off for a standard green card or with the seeding of for the running green card case.
PDV Data Images	PDV data is taken with the laser, seeding, and flow on with the laser tuned in frequency to the approximate 50% transmission location. This frequency should be varied slight during data acquisition to insure that the Doppler shift does not shift the scattered signal to far into or away from the transmission profile where there is no sensitivity.
PDV Background Images	Background images should be taken for the data images with the seeding off and laser tuned outside of the filter and at the transmission level in which data was taken.
Camera component and	Position measurements should be taken so that the

incident laser positions	incident and observation vectors can be calculated for the laser and each PDV camera component.

Table 3.1 Data collection for a general PDV test.

4. Data Processing Methodology

      After obtaining the PDV data from a test the following five image processing steps are required:

    1.   ***Image mapping*** from dotcard images which includes tie-point determination (finding the pixel locations of each dot) and mapping each image so that they overlap pixel for pixel.

    2.   ***Determinate intensity calibration parameters*** to match the intensity of each signal and reference PDV camera pair.

    3.   ***Apply spatial and intensity calibration to PDV data*** so that the transmission ratio can be calculated for each camera component.

    4.   ***Calculate Doppler frequency shift*** by applying the appropriate frequency function to the measured transmission ratio at each pixel and correcting for the frequency measured by the wavemeter.

    5.   ***Calculate velocity components*** from the measured frequency and incident and observation unit vectors.

The key processing methodology for PDV is summarized in the diagram of Figure 4.1 and described in detail in the following sections.

   4.1.   Image Mapping

      The ratio of the signal (filtered) and reference (unfiltered) images are needed to calculate the transmission ratio of each PDV component. It was necessary to align the views from the two cameras so that they overlapped as nearly as possible on a pixel to pixel basis. To accomplish this spatial alignment (or image mapping) the following steps were taken.

      Images of the dotcard, as described previously, were taken and the approximate pixel coordinates of the three dots in the upper left of each view were identified. Using this information as a starting point, a computer program found the center of each dot by the method of centroids, which is described briefly as follows. First, the image was inverted so that the dark dots were represented by high intensities and the light field was represented by low intensities. Then, a rectangular sub-region was selected based on the initial pixel location information. This sub-region contained a single given dot. The intensity-weighted centroid of this sub-region was

43

calculated, and a new sub-region was defined centered at this centroid. This procedure was repeated until the difference in centroid locations between iterations fell below a threshold. The rectangular sub-region was then deemed to be located over the dot-center, which could be found to sub-pixel accuracy. The procedure was repeated for all the dots in the field that defined the imaging plane. This program generates a file containing the dot locations in the signal (filtered) and reference (unfiltered) camera views (x_i', y_i'). The program also generates a rectilinear set of coordinates (x_i, y_i) corresponding to a common normal view of the dotcard plane. These dot locations, known in the original and mapped coordinates, are referred to as tie-points.

In later stages of the data reduction, the output of the dot-finding program was used by another program to map pairs of signal and reference camera images so that they corresponded on a pixel-to-pixel basis. The mapping program used bilinear interpolation to locate a source pixel in the unmapped image for every pixel in the mapped image. The relationship between a pixel location in the source image, (x', y'), and that in the mapped image, (x, y), was given by

$$x' = a_1 x + a_2 y + a_3 xy + a_4 \qquad \text{Equation 4.1}$$

$$y' = a_5 x + a_6 y + a_7 xy + a_8$$

where the mapping coefficients, a_i, were found for each sub-region of the image by solving two sets of four simultaneous equations based upon the tie-points provided by the dot-finding program. These tie-points defined the corners of the sub-region. The equations were

$$\begin{bmatrix} x_1' \\ x_2' \\ x_3' \\ x_4' \end{bmatrix} = \begin{bmatrix} x_1 & y_1 & x_1 y_1 & 1 \\ x_2 & y_2 & x_2 y_2 & 1 \\ x_3 & y_3 & x_3 y_3 & 1 \\ x_4 & y_4 & x_4 y_4 & 1 \end{bmatrix} \begin{bmatrix} a_1 \\ a_2 \\ a_3 \\ a_4 \end{bmatrix} \qquad \text{Equation 4.2}$$

$$\begin{bmatrix} y_1' \\ y_2' \\ y_3' \\ y_4' \end{bmatrix} = \begin{bmatrix} x_1 & y_1 & x_1 y_1 & 1 \\ x_2 & y_2 & x_2 y_2 & 1 \\ x_3 & y_3 & x_3 y_3 & 1 \\ x_4 & y_4 & x_4 y_4 & 1 \end{bmatrix} \begin{bmatrix} a_5 \\ a_6 \\ a_7 \\ a_8 \end{bmatrix}$$

where the points (x_i, y_i) and (x_i', y_i') were the known tie-points. Note that the location in the source image, (x',y'), was not generally given by integer pixel values. Therefore, the intensity value assigned to the mapped image was calculated as a weighted average of the nearest four pixels. Note that the data acquisition program stores signal and reference image pairs side by

side with multiple components stored vertically in a single file. The mapping procedure produced a new file with the signal image and reference image side-by-side with corresponding pixel coordinates (x, y).

Figure 4.2 shows the dot-card image (averaged from 10 instantaneous images) that was obtained for a single PDV velocity component in the SARL wind tunnel. After the dot finding program is run, the tie point locations are found for each dot, a normal grid is calculated, and the tie point information is output to files for each component and camera view. If we apply the tie points and map the dotcard as shown in Figure 4.2b we can check the mapping procedure and observe the normalized plane in which the data will be mapped onto.

It should be noted that before applying the mapping procedure to green card or PDV data, the images are generally low-pass filtered. The low-pass filter operated by replacing the value at each pixel location with an average of a 5 by 5 or as much as 7 by 7 block of pixels in the region centered at that pixel. This low-pass filtering, or smoothing, was an effort to minimize the effects of laser speckle and came at the cost of some optical resolution. In addition the background (images taken with the laser on and no seeding) is subtracted from all the images. The image mapping procedure is performed on both the green card images (so that the intensity calibration coefficients can be determined) and the PDV data.

During the test, it is possible that that vibrations, etc. could cause a slight misalignment of the cameras. To test for this condition, a running cross-correlation technique was developed. After all signal and reference images had been mapped onto the tie-points alignment was checked by computing the cross-correlation between the signal image and the reference image in each component. The interrogation region included the entire image. The misalignment was generally a bulk shift of the entire image. This bulk shift will appear as the displacement vector between the two images in the cross-correlation. The reference image is then shifted by this slight amount to improve the alignment between the images before the ratio is computed. This running dotcard correction provided a significant improvement to the final data set. Some investigation to developing a running dotcard process for aligning all images is recommended as a means of improving tunnel productivity.

4.2. Determination of Intensity Calibration Parameters

In addition to the mapping procedure described above, an intensity calibration procedure is required before the ratio of the signal to reference images, S_{c12}, can be determined from the camera outputs. The intensity calibration procedure is an effort to remove the differences arising from the beam splitter efficiencies, the optical paths, and the camera sensitivities. If successful, the ratios recorded by the PDV camera system will correspond to the transmission ratio axis of the camera frequency function, ζ_c.

First, the calibration coefficients need to be determined from the green card (or running green card) images described previously. These images are used to scale the reference image intensities to those of the signal images. Regardless of the details of the green card acquisition, the procedure for scaling the images was identical. After background subtraction and smoothing, the images were mapped according to the procedure described above so that the signal and reference images (S_{c1} and S_{c2}, respectively) corresponded on a pixel to pixel basis. The calibration images were then low-pass filtered. Because these files were acquired at a frequency of flat maximum laser transmission, the ratio of the signal to reference images should be unity on the normalized scale of the camera frequency function, ζ_c. Thus, we wished to find calibration parameters that would minimize the difference between the filtered image and the calibrated reference image at each pixel.

Using the following calibration function

$$S_{c2}^{cal}(x, y) = m_{cam}(x, y)S_{c2}(x, y) + b_{cam}(x, y) \qquad \text{Equation 4.3}$$

and the complete set of green card files, linear curve fits were performed at each pixel over a broad range of intensities to determine the slope and intercept values that best related the reference image to the signal image. Here, m_{cam} and b_{cam} are the intensity calibration parameters. In a common least squares methodology the calibration parameters were found so that they minimized

$$\chi^2 = \sum_{i=1}^{k} \left(\frac{S_{c1,i}(x, y) - S_{c2,i}^{cal}(x, y; m_{cam}, b_{cam})}{\sigma_i} \right)^2. \qquad \text{Equation 4.4}$$

Here, i is an index over the sequence of images acquired at varying intensities and σ_i is assumed to be proportional to $\sqrt{S_{c2,i}}$. This is a good assumption when the dominant noise source is

46

photon-statistical and perhaps not so appropriate for speckle-dominated noise. Such a fitting procedure is called a chi-square fit.[17] The slopes and intercepts were then used to convert the intensities of the reference images to the scale of the signal images according to equation 4.3. It should be noted that due to the background subtraction, the values of the intercept b were expected to be close to zero and this was found to be the case. Therefore, this calibration step for electronic gain and optical differences was primarily a scaling with very little offset. As mentioned previously either standard or running green card images can be used. In addition low and high signal level thresholds were set so to avoid saturation and low signal levels which may cause erroneous results. These thresholds were set manually, although later results (Boeing UCAV data) utilized an automated threshold which rejected a multiple of the standard deviation (set generally between 0.5 to 3) from all the intensity data collected. The statistical rejection procedure also avoided intensity outliners.

Figure 4.3 shows the raw data and calibration curves at a typical pixel location calculated for the standard green card and running green card images with the tunnel empty and a model in place for one of the SARL tests (multiple component delta wing model to be presented shortly). As observed the methodologies produce similar results and nearly the same slope. However the standard green card has the lowest deviation between the raw and calibrated intensities. This is due primarily to the fact that tunnel vibrations most likely cause some reference to signal image misalignment, the effect of which is enhanced since the seeding is non-uniform and there can be "sharp" intensity edges which cause additional noise in the data. It should be pointed out, however, that these effects are averaged out when many images are taken. The result is that approximately the same values for the slope and intercept are found in each case.

4.3. Apply Spatial and Intensity Calibration to PDV Data

The previously outlined steps provided all the necessary mapping and calibration data. As described in the PDV data collection procedure given background images and data images are acquired and subtracted so that the bias of stray background light was removed. The foregoing background subtraction step may be represented as

$$S = S_{raw} - B \qquad \text{Equation 4.5}$$

where S is a data image corrected for background light, S_{raw} is the data image as acquired without processing, and B is the background image.

These background-corrected images are low-pass filtered (smoothed) and mapped following the procedure described previously. The low-pass filtering may be represented as

$$S_i^*(x, y) = \frac{1}{n^2} \sum_{j=-(n-1)/2}^{j=(n-1)/2} \sum_{k=-(n-1)/2}^{k=(n-1)/2} S_i^* i(x+j, y+k)$$

Equation 4.6

where n is an integer representing the size of the region used in smoothing. The mapping step may be represented as

$$S_{c1}^*(x', y') \longrightarrow S_{c1}(x, y)$$

Equation 4.7

$$S_{c2}^*(x', y') \longrightarrow S_{c2}(x, y)$$

where the relationship between the source points, (x_i', y_i') and mapped points, (x_i, y_i) was determined as outlined above and the asterisk denotes that no filtering had been applied. The subscript 1 denotes the signal image and the subscript 2 denotes the reference image. As an example Figure 4.4 shows a raw instantaneous PDV data image from the three component delta wing test and the same data after spatial mapping program and intensity calibration has been applied. Even at this stage comparing the signal (filtered left) and reference (right) images the effect of the velocity can be qualitatively observed in the region of the vortices for each PDV component.

The reference images were then calibrated with the previously determined slopes and intercepts, m_{cal} and b_{cal} according to Equation 4.3 so that they ranged on the same scale as the signal images. The signal images were then divided by the calibrated reference images, producing a series of images containing the transmission ratio at each pixel. The transmission ratios derived from the camera images may be represented as

$$S_{c12} = \frac{S_{c1}}{m_{cal}S_{c2} + b_{cal}} \approx \frac{S_{c1}}{m_{cal}S_{c2}}$$

Equation 4.8

where the approximate equality holds because the values of the intercept b_{cal} are so small relative to the product of the reference signal level and the slope. For the same data presented in the previous figure the output of the calibrated reference and signal images after they are divided resulting in the transmission ratio at each pixel location is given in Figure 4.5a. Note also that the slope and intercept could just as easily be computed for the filtered signal (S_{c1}) instead, which was done in some of the experiments conducted during the development of the PDV system.

4.4. Calculate Doppler Frequency Shift

These transmission ratios were then converted to relative frequency through the frequency function, ζ_c, determined previously for the camera filter. Because the laser centerline frequency generally exhibits jitter from pulse-to-pulse (and consequently, from image-to-image), the relative frequency of each unshifted laser pulse is needed in order to calculate the Doppler shift. As described previously, the data acquisition software was designed to acquire a record of the laser reference intensity and signal intensity from the wavemeter for each PDV image taken. The ratio of these intensities, appropriately normalized (using equation 3.2), can be used to calculate the transmission ratio (S_r) for each imaging laser pulse. This transmission ratio is then used to measure the frequency of the laser through the wavemeter frequency function, ζ_r (transmission curve of the wavemeter iodine filter profile). In addition the transmission ratio has been calculate for each signal and reference image pair (S_{c12}) and each PDV component if more than one is taken (i.e. S_{c12}, S_{c34}, S_{c56}). Limits on the intensities which were considered to be "good" for the data set (avoiding areas of saturation or low signal level) were determined in the same method as the mapping procedure. With a knowledge of the frequency function of each PDV component (ζ_{c1}, ζ_{c2}, ζ_{c3}) the Doppler shift corrected for laser frequency fluctuations can be calculated by

$$\Delta f_D = \left[\zeta_c \left(S_{c12} \right) - \zeta_r \left(S_r \right) \right] \qquad \text{Equation 4.9}$$

Again using the same instantaneous data, Figure 4.5b shows the frequency of the Doppler shift after the frequency function has been applied.

4.5. Calculate Velocity Components

The final step in processing PDV images is to determine the velocity after the appropriate calibration steps have been taken. Once the Doppler shift is known, there are two methods used to convert the frequency into a velocity representative of the flow field.

4.5.1. Determination of Velocity in the Direction of System Sensitivity

First and most easily, the velocity in the direction of system sensitivity can be calculated for each PDV component obtained. The direction of this velocity magnitude is given by the unit vector defined by the observation minus incident unit vectors ($\underline{k}_0$ - $\underline{k}_i$) for each PDV component.

The velocity in the direction of system sensitivity may be calculated for each PDV component independently using the modified Doppler shift equation expressed as

$$V_{PDV} = \frac{\lambda}{2\sin(\varphi/2)}\left[\zeta_c\left(S_{c12}\right) - \zeta_r\left(S_r\right)\right]$$

Equation 4.10

Here the term in brackets is the Doppler shift expressed in terms of the camera frequency function and the reference system frequency function. The left-hand side of this equation is the velocity component in the direction of system sensitivity for that particular PDV component. As defined previously the angle ϕ is the angle between the incident and scattering vectors as illustrated in Figure 1.3. Figure 4.5c shows an example of the three component PDV instantaneous image after it has been converted from frequency to the parallel velocity component shown previously. In each of the velocity components the induced velocity from the vortex is clearly visible. Although this is the easiest velocity to calculate the downside is that the direction of the velocity is often not aligned with a reasonable direction or coordinate aligned with a natural flow direction making interpretation of the results sometime difficult. This is the main motivation for utilizing multiple components which are needed to calculate velocity components in directions which are relevant to the model geometry and flow directions.

4.5.2.   Determination of Multiple Velocity Components

The major goal of the current research program was to develop a PDV system which could measure single velocity components in a large scale wind tunnel. The system was to be extended so that multiple velocity components could be measured simultaneously. In an effort to understand the data collection and processing methodology necessary to obtain multiple velocity components in a rectangular orthogonal coordinate system (x, y, z) we return to Equation 1.1. First, recognize that if we vary the observation direction (image the light sheet from cameras observing from different directions) we can write multiple Doppler shift equations for each view. For simplicity we begin by rewriting Equation 1.1 as

$$\Delta f_D = \frac{1}{\lambda}\left(\underline{k}_{oi}\right)\cdot\vec{V}$$

Equation 4.11

where $\underline{k}_{oi}$ is the termed the system sensitivity vector and is the difference between the observation and incident light vectors ($\underline{k}_0$ - $\underline{k}_i$) which will vary for each camera view. Now consider the case where the light sheet is viewed from three different directions. There will be

three different $\underline{k}_{oi}$ vectors and three different Doppler shifts measured at each viewing angle. We can write three equations (one for each view) given by

$$\Delta f_{D1} = \frac{1}{\lambda}\left(\underline{k}_{oi1}\right)\cdot\vec{V}$$

$$\Delta f_{D2} = \frac{1}{\lambda}\left(\underline{k}_{oi2}\right)\cdot\vec{V} \qquad\qquad \text{Equation 4.12}$$

$$\Delta f_{D3} = \frac{1}{\lambda}\left(\underline{k}_{oi3}\right)\cdot\vec{V}$$

Similar to the single component case, the Doppler shift is measured from the transmission ratio of each reference and signal camera at each location and the laser frequency is determined from the wavemeter. This can be expressed as three equations given as

$$\Delta f_{D1} = \left[\zeta_{c1}\left(S_{c12}\right)-\zeta_{r}\left(S_{r}\right)\right]$$

$$\Delta f_{D2} = \left[\zeta_{c2}\left(S_{c34}\right)-\zeta_{r}\left(S_{r}\right)\right] \qquad\qquad \text{Equation 4.13}$$

$$\Delta f_{D3} = \left[\zeta_{c3}\left(S_{c56}\right)-\zeta_{r}\left(S_{r}\right)\right]$$

where S_{c12}, S_{c34}, S_{c45} is transmission ratio determined for each of the three camera views after the mapping and calibration steps described previously, and ζ_{c1}, ζ_{c2}, ζ_{c3} are the frequency functions of the iodine filters in front of the signal cameras in each of the three systems. The Doppler shift is a known quantity for each PDV system. If the optical difference vector ($\underline{k}_{oi1}$, $\underline{k}_{oi2}$, $\underline{k}_{oi3}$) is known from the orientation of each PDV system the only unknown is the velocity vector to be measured. We can write three equations with three unknowns which are the three velocity components (V_x, V_y, V_z).

$$\lambda\Delta f_{D1} = k_{oi1x}V_x + k_{oi1y}V_y + k_{oi1z}V_z$$

$$\lambda\Delta f_{D2} = k_{oi2x}V_x + k_{oi2y}V_y + k_{oi2z}V_z \qquad\qquad \text{Equation 4.14}$$

$$\lambda\Delta f_{D3} = k_{oi3x}V_x + k_{oi3y}V_y + k_{oi3z}V_z$$

To solve this system of equations we can rewrite them in matrix form given by

$$\begin{pmatrix} V_x \\ V_y \\ V_z \end{pmatrix}\begin{pmatrix} k_{oi1x} & k_{oi1y} & k_{oi1z} \\ k_{oi2x} & k_{oi2y} & k_{oi2z} \\ k_{oi3x} & k_{oi3y} & k_{oi3z} \end{pmatrix} = \lambda\begin{pmatrix} \Delta f_{D1} \\ \Delta f_{D2} \\ \Delta f_{D3} \end{pmatrix} \qquad\qquad \text{Equation 4.15}$$

$$\mathbf{V}\left[K_{oi}\right] = \lambda\Delta\mathbf{f_D}$$

The solution to each velocity component is easily solved using Cramer's Rule which is written as

$$V_x = \frac{\det[K_{oi1}]}{\det[K_{oi}]}$$

$$V_y = \frac{\det[K_{oi2}]}{\det[K_{oi}]} \qquad \text{Equation 4.16}$$

$$V_z = \frac{\det[K_{oi3}]}{\det[K_{oi}]}$$

Where $\det[K_{oi}]$ is the determinate of the $[K_{oi}]$ matrix, and $[K_{oij}]$ is the modified matrix obtained by replacing the jth column with the vector $\lambda \Delta \mathbf{f_D}$. As one might expect the velocity vector V, is solvable only if the determinate is nonzero. This occurs if two of the optical difference vectors are the same or one of the vectors is a linear combination of the other two. Unfortunately, this was the case for the first three component test as will be discussed shortly.

This matrix approach is probably the simplest approach for solving three velocity components (since there are canned subroutines to solve a linear set of equations and substitution would be tedious). However, if a camera arrangement is used that is insensitive to one component, (i.e. the z component) we can solve the case for two components by direct substitution. If you consider a two component system, we can write two equations, one for each PDV system viewing angle.

$$\lambda \Delta f_{D1} = k_{oi1x} V_x + k_{oi1y} V_y$$

$$\lambda \Delta f_{D2} = k_{oi2x} V_x + k_{oi2y} V_y \qquad \text{Equation 4.17}$$

By substitution of this set of equations (two equations and two unknowns we can write two equations one for each velocity component in terms of known and measured quantities as

$$V_x = \frac{\lambda \Delta f_{D1} - k_{oi1y} V_y}{k_{oi1x}} = \frac{k_{oi2y} \lambda \Delta f_{D1} - k_{oi1y} \lambda \Delta f_{D2}}{k_{oi2y} k_{oi1x} - k_{oi1y} k_{oi2x}}$$

$$V_y = \frac{k_{oi1x} \lambda \Delta f_{D2} - k_{oi2x} \lambda \Delta f_{D1}}{k_{oi2y} k_{oi1x} - k_{oi1y} k_{oi2x}} \qquad \text{Equation 4.18}$$

All variables in Equation 4.18 are known so first solve for V_y, then substitute to solve for V_x. Equation 4.18 can be evaluated at each pixel location to solve for the V_x, and V_y velocity components.

4.6.   Data Processing Programs

PDView is a software package for manipulation and processing of PDV data.   The package incorporates the tools necessary for PDV data reduction into a program with a Graphical User Interface.   The program supports basic functions such as addition, subtraction, multiplication and division of images. Advanced functions such as filtering, cropping, and de-warping of images are also available. These functions can be performed on single images or in batch mode on a set of images. The data reduction process for PDV has been described in some detail in the preceding section of this report.   A detailed description of the data reduction algorithms will not be repeated here. This section will serve as basic guide through the menus and options necessary for data reduction using PDView.   A more detailed explanation of the functions in the package is available in the Online Help in the program.

4.6.1.   General Functions

The main panel, shown in Figure 4.6, includes the Canvas and the Main Menu.   The Canvas is used to display images and the Main Menu is used to select operations that are performed on the displayed image. Below the Canvas, two lines of text are displayed. The first line displays the file format and the second line displays the file name of the image that is currently displayed. After the file is open, the user may interrogate the image using the mouse and display the image intensity at the position of the mouse. This is accomplished with a Left-Click on the mouse. The mouse position and image intensity are displayed on the first line of text below the Canvas. An enlargement of the image (Zoom) centered on the mouse position is displayed upon a Right-Click of the mouse. The Main Menu contains eight options, File, Image, Filter, Batch, Markers, Map, PDV, and Help as shown in Figure 4.7. Each option is discussed in the following.

The File menu is used primarily to Open and Export images. Under the Load option, the user may select to load an individual image (Image, Reference, Background) or a set of images, (Image, Image List). Reference and Background images are used for performing Image Math operations. Often, it is desirable to perform a set of operations on a batch of images. An Image List file simplifies this process by saving the file names of a set of images in a single file. All images in the list are loaded by selecting the list file. Upon completing image-processing operations, the user often needs to save the resulting data. This is accomplished using the Export

option. The Export opting allows the user to save the displayed image in a user selected file format.

The Image menu includes several operations that can be performed on the displayed image. Among the more useful options are the Graph and Math operations. The Graph option allows the user to display data along a line of the displayed image. The user selects the end points of the line using the mouse and a Pop-up Panel is displayed with a plot of the data from the selected line. An example of the line of data and the resulting Graph are shown in Figure 4.8. The Math menu (Figure 4.9) includes options for performing basic math function on the displayed image. These functions include Subtracting the Background image from the displayed image and Division of the displayed image by the Reference image. The Filter menu provides the user with the ability to apply several versions of High Pass and Low Pass Filters to the displayed image. Non-linear filters such as Median and Edge filters are also available. The Filter Menu is shown in Figure 4.10. The user may preview the results of the filter operation and choose to revert to the raw image if the results are not satisfactory.

Often, the operations available in the Image and Filter menus must be repeated on a series of images. To this end, many of these operations such as Subtracting Background images and Exporting Images can be performed in Batch mode. The Batch menu provides a means of performing these repetitive operations with a single command. The options available in the Batch Menu are shown in Figure 4.11.

4.6.2.   PDV Data Reduction Functions

The process of converting raw PDV images to Doppler shifts and velocities requires that the images are de-warped, normalized using green card data, converted to Doppler shift, and then to velocity. The PDView functions that are used in this process are described in the following section.

The first step to image de-warping is the location of the markers on the dot card. The Marker option is used to locate the markers (dots) that are used in the image alignment and de-warping process. The menu has several options as shown in Figure 4.12. The Locate option is useful for investigation of individual dots. The Locate option can be used to interrogating the dot card and refine the marker finding parameters. The Mark Rows & Columns option is used to automatically locate a series of dots on an image. These dots must be arranged in a uniform

pattern on the image. The information used to locate a set of dots can be saved into a formatted file for later retrieval. This file, referred to as a Script File, can be loaded using the Load Marker Script option.

Before locating any markers, the Marker Panel shown in Figure 4.13 is displayed. The first parameter of interest on the Marker Panel is the Marker Size. This parameter refers to the diameter of the markers in units of pixels. The second option of interest is the Mark Image/Negative switch. The algorithm that is used to locate markers searches for the location of the first moment within a window on the image. The first moment is defined as a maximum. If the dots are dark and the background is bright, the program must first make a negative of the image and then locate the markers. With these two options set, the user may investigate individual markers by selecting them with the mouse. The program will locate the nearest marker, and this location will be displayed below the Canvas. Once the proper settings of marker size and Image/Negative switch have been validated, the dots can be marked automatically using the Mark Rows & Columns option.

To locate a set of markers using the Mark Rows & Columns option, several fields on the Marker Panel must be filled in. The Marker Size and Image/Negative fields have been discussed. The user must set the number of Rows and Columns of markers to be located. The file containing the image to be marked is selected by Right-Clicking the Image field. This initiates a File Select Pop-up dialog that allows the user to select an image file. A similar process is used to select the Marker file. The Marker file will contain the resulting marker locations. The Grid file is a user-defined file that contains a uniform grid of marker locations. This is the Tie-Point file for mapping images. The spacing of the Tie-Point markers is defined using the dS field. With these parameters set, the user selects the Mark Three button. This initiates a process where the user defines three key markers for the program. These markers are used to initiate the automatic marker recognition process. After located the three markers, the user selects the Run Script button and the remaining markers are located. The marker locations are written to the Marker file and the Tie-Point locations are written to the Grid file.

The signal and reference images from each view must be mapped onto the Tie-Points. This process serves to align and de-warp the images. This process is accomplished in batch mode using the Map Batch option from the Map menu shown in Figure 4.14. Selecting the Map Batch option will display the Map Batch panel, shown in Figure 4.15. This panel is designed to

carry out several steps in the PDV data reduction process. The user enters a list of images to be processed using the Image list field. The target for the mapping, the Tie-Points, is selected using the Grid field. A Background image may be selected and subtracted from each image before mapping. User defined filters can be applied to each image both before and after mapping as well. The signal and reference images for each component of the PDV system are combined and stored into a singe file by the data acquisition program. This means that for a three-component system up to six regions of the image must be processed. The Marker File button is used to select the Marker file for each region of the image. A corresponding Output Path button is used to select a target path for the image that results from each mapping region. The mapped files will have the same name as the input file but they are stored in different directories and have a user-defined extension. With the parameters selected, the batch is mapped by selecting the Map Batch button.

The process of developing the Green Cards is controlled under the PDV Menu using the Green Card option (Figure 4.16). The Green Card Panel (Figure 4.17) is displayed and the user fills in the appropriate fields. The Signal list and Reference list refer to a list file with the names of mapped signal and reference green card images. The program computes a slope and intercept at each pixel that meets the criteria for the minimum number of valid pixels. The Slope and Intercept images are stored in files defined by these fields on the panel. The process is executed by selecting the Process button. The resulting Slope and Intercept images will be displayed on the Canvas of the main panel. The user can interrogate the images to locate problem areas.

The conversion of the mapped PDV images to Doppler shift is initiated by selecting the Doppler Shift option from the PDV menu (Figure 4.16). The Doppler Panel, shown in Figure 4.18, is displayed. The user supplies a list of Signal and Reference images to be processed. A file containing the wavemeter ratio that was collected with each image is entered into the Wavemeter List field. The Slope and Intercept Green Card images from this view are also selected. Finally, the transmission profile for the wavemeter and the camera Iodine filter are selected. The user may select to apply a Range filter or a spatial filter to the processed images before they are stored to the selected Output directory. The images will retain the image name and carry the *.dop file extension. This process is repeated for all three views from the PDV system.

The final step in the data reduction process is the conversion of the Doppler shift data to velocity. This is initiated by selecting the Velocity option from the PDV Menu. The Velocity Panel, shown in Figure 4.19 is displayed. The user enters the positions of each camera view, the Laser, and the center of the dot card. The Laser frequency is entered in wavenumbers. The velocity panel will operate on a single set of images or a list of images. The file is entered into the Doppler List field for each view. The data is processed by selecting the Process button and the resulting velocity data is written to the user-selected Output directory.

Data Taken	**Processing Steps**	**Verification Checks**

Dot Card Images → **Image Mapping**
- Pick 3 dots in upper left corner of each image
- Determine tie points from centroid analysis
→ View centroids on reconstructed dot card images or apply tie points and map dot card which should result in an orthogonal grid.

Green card (static or running) images and background images with laser on and smoke off → **Determine Intensity Calibration Parameters**
- Subtract background images
- Apply low pass filter
- Apply least squares fit between signal and reference image
- Calculate slope and intercept to calibrate reference image intensity to signal image intensity at each pixel
- Apply low pass filter to slope and intercept if needed.
→ View slope and intercept images. Slope image should be smooth and uniform. Intercept image should be nearly zero everywhere.

Apply image mapping procedure and intensity calibration to green card images. Divide signal and reference images and average all images. Resulting image should be unity everywhere.

PDV Data Images taken over a range (3) of frequencies. Background images taken with The laser on, smoke off, at frequency where data was taken. → **Apply Spatial and Intensity Calibration to PDV Data**
- Subtract background images
- Apply low pass filter
- Use tie points to map image
- Apply slope and intercept to calibrate reference and images.

Filter profiles of wavemeter filter and camera components. Photodiode (Joulemeter) values from wavemeter. → **Calculate Doppler Frequency Shift**
- Divide calibrated signal and reference image pairs and determine transmission.
- Compute Doppler shift from signal camera's filter profile and laser frequency as determined from wavemeter.
- Average frequency images.
→ Check that there are no strong gradients which may be due to image misalignment.

Physical locations of camera model, and laser coordinates. → **Calculate Velocity Components**
- Calculate incident light unit vectors and observation unit vectors for each PDV comp.
- Calculate sensitive vectors for each camera component.
- Calculate velocity components.
→ Check free stream velocity away from the model.

Figure 4.1 Diagram of main processing steps in obtaining velocity information from PDV images.

Raw Dotcard Image

Mapped Dotcard Image

Figure 4.2 Dot-card images for tie point calculations of three component PDV measurements. The top image is the average dot-card image with the bottom image the same dot-card after mapping.

Running Green Card Empty Tunnel

Standard Green Card
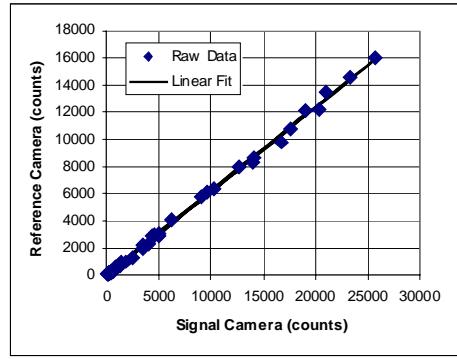
Running Green Card with Model

Calibration curves and raw data for
the pixel location in PDV
component #1 (100,200)

Figure 4.3 Calibration curves calculated from standard green cards, empty tunnel running green
cards, and model running green cards.

0   45000

PDV Image after smoothing

0   45000

PDV Image after mapping
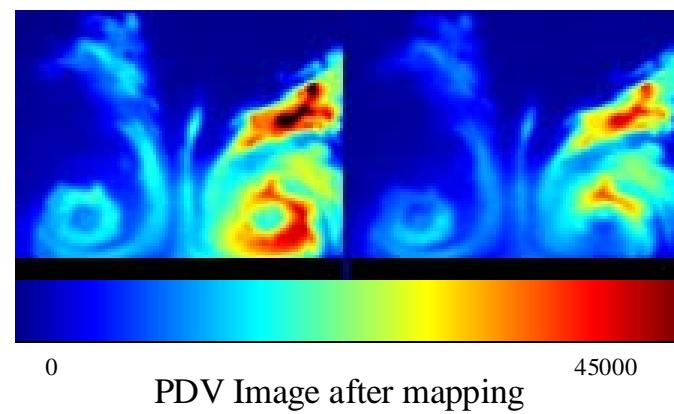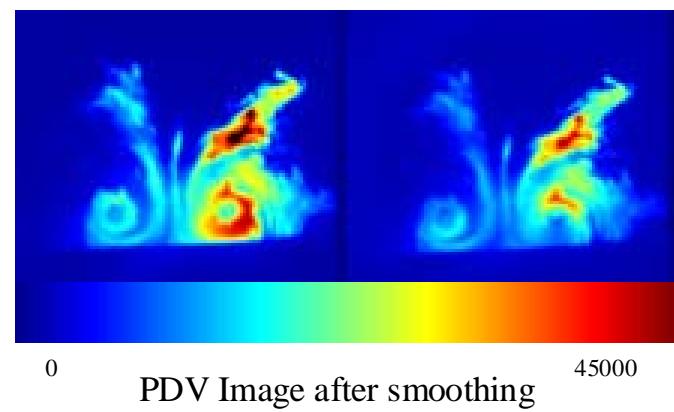
Figure 4.4 Raw PDV image after smoothing (top) and mapping (bottom) using tie points from dotcard.
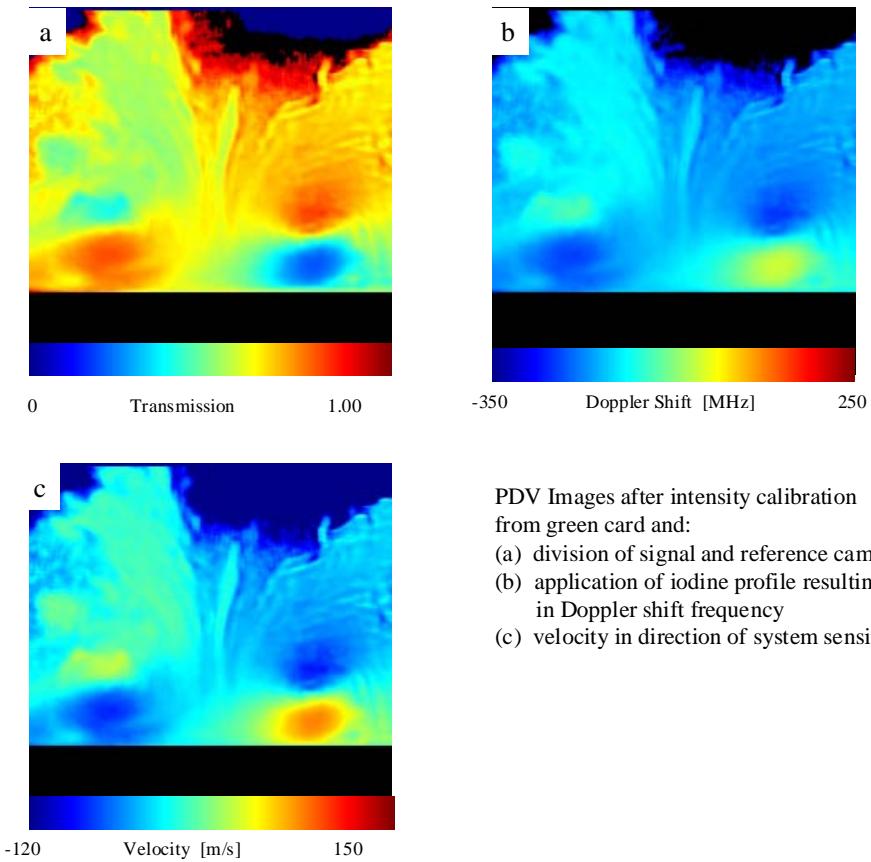
Figure 4.5 PDV Images after intensity calibration from green card and division of signal and reference camera (a), application of iodine profile resulting in Doppler shift frequency (b), and velocity in direction of system sensitivity (c).
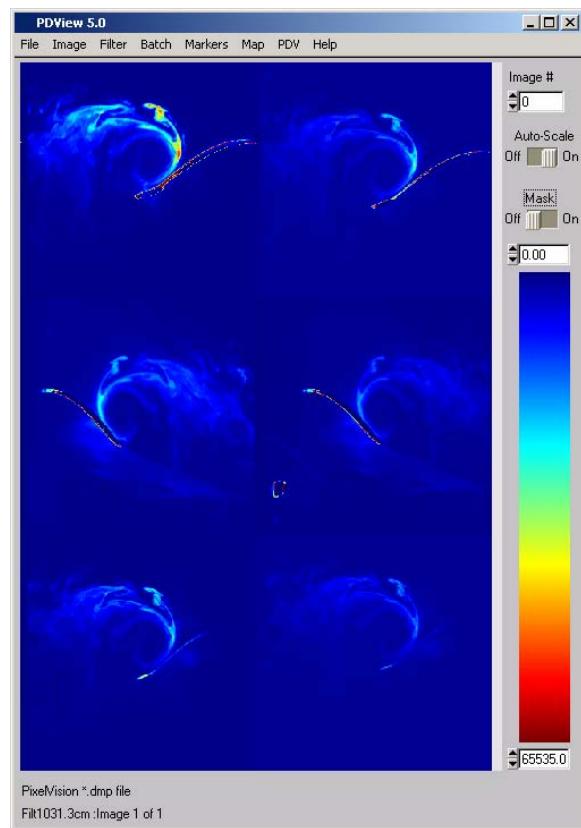
Figure 4.6 PDView Main Panel.

Figure 4.7 PDView Main Menu.
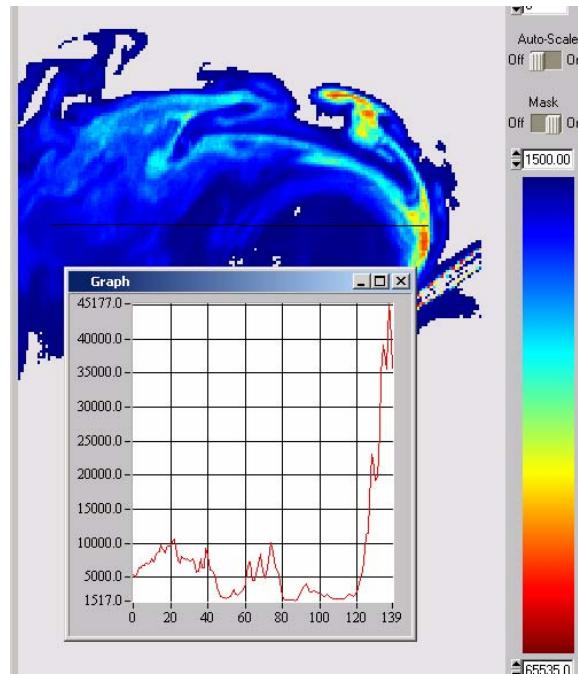
Figure 4.8 PDView Graph Panel.
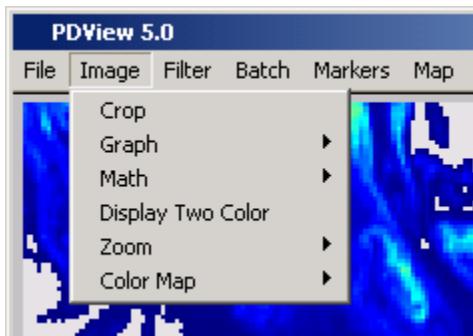
Figure 4.9 PDView Image Menu options.
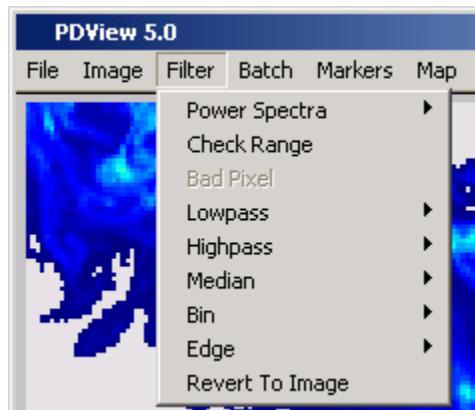
Figure 4.10 PDView Filter Menu options.

Figure 4.11 PDView Batch Menu options.
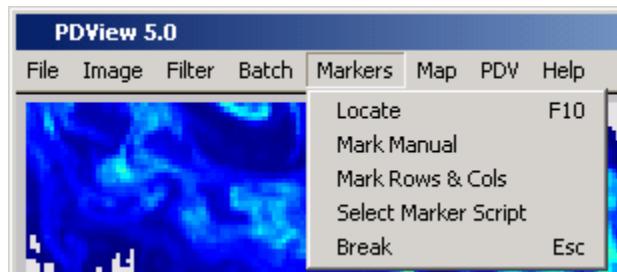
Figure 4.12 PDView Marker Menu options.
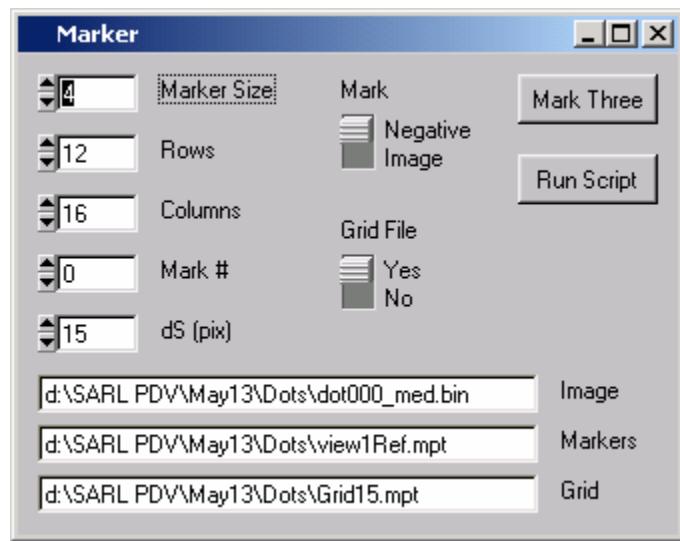
Figure 4.13 PDView Marker Panel.
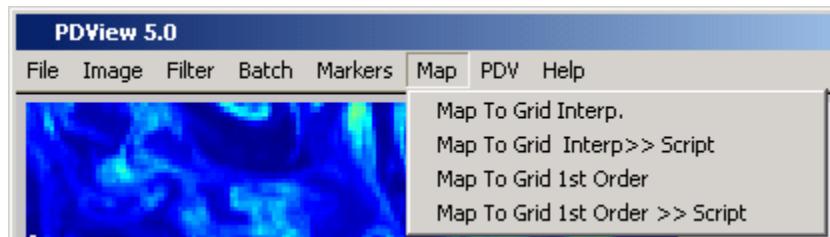
Figure 4.14 PDView Map Menu options.
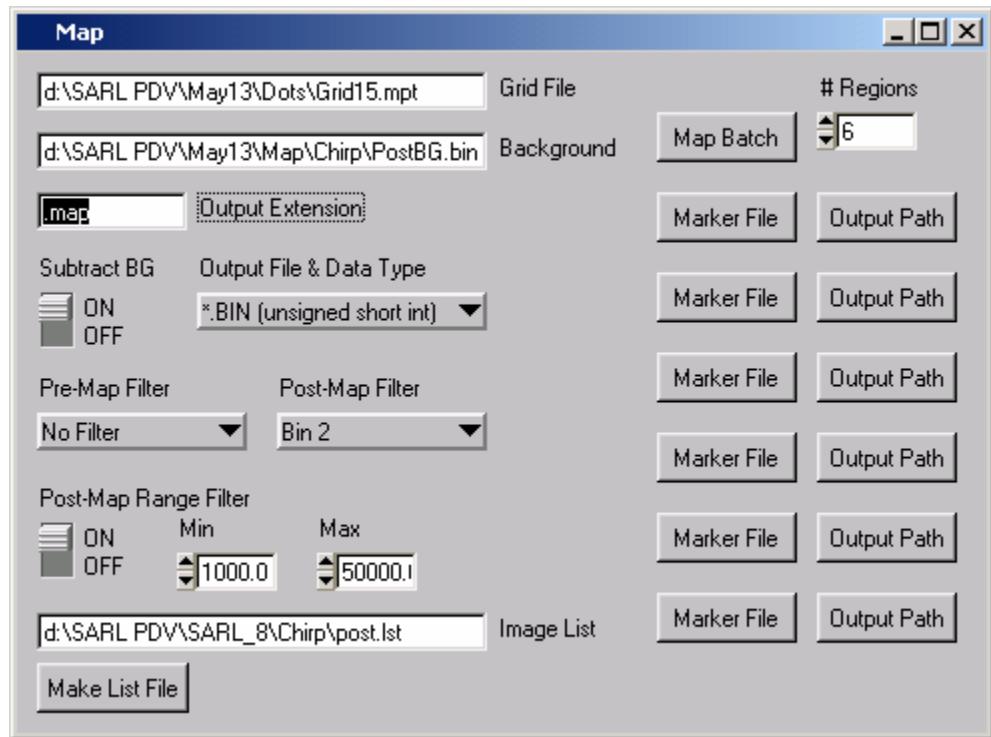
Figure 4.15 PDView Map Panel.
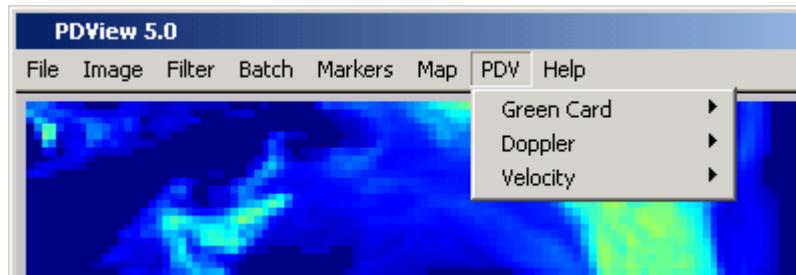
Figure 4.16 PDView PDV Menu options.
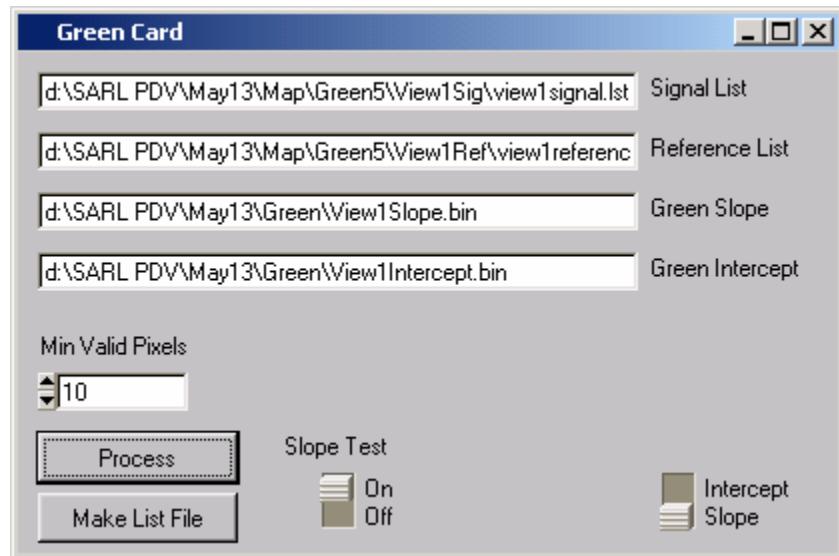
Figure 4.17 PDView Green Card Panel.
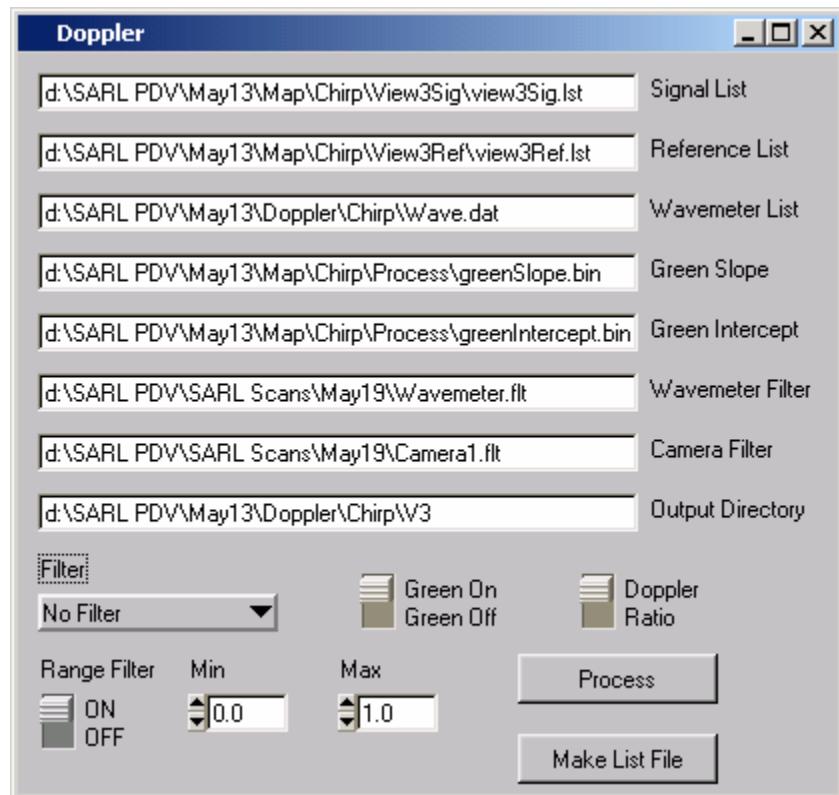
Figure 4.18 PDView Doppler Panel.
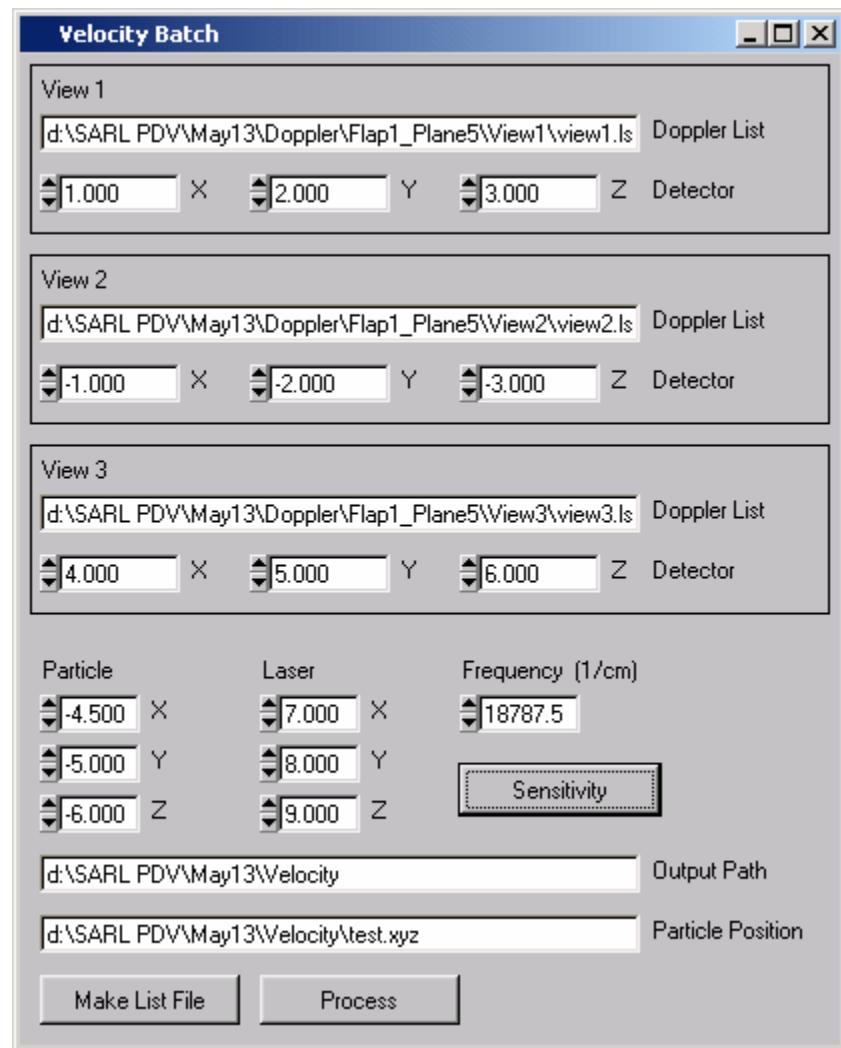
Figure 4.19 PDView Velocity Panel.

5. Flow Fields Investigated

Following is a description of the flow fields which were investigated in the study as the PDV system was developed for large wind tunnel tests. This is proceeded by a description of the two facilities which were used to develop the PDV system. A small scale jet facility was used to test and evaluate PDV components and methodologies. The SARL facility, a large scale subsonic wind tunnel, was the target for the final PDV system. Single component measurements were used to develop, evaluate, and prove a PDV concepts. Multiple component tests used to develop the PDV system and methodology so that two or three components could be measured simultaneously. Finally, aircraft model tests were conducted to evaluate problems and formulate solutions associated with measurements on models with a complex geometry. The final three component PDV test was conducted on the Boeing UCAV model.

5.1. Facilities

The jet experiments were performed on an axisymmetric jet created through a Mach 1.36 converging-diverging nozzle designed by the method of characteristics (12.7 mm exit diameter). The typical PDV arrangement for the small scale jet experiment is given in Figure 5.1. The jet can be operated from dry air high pressure storage tanks at a perfectly expanded pressure of 283 kPa and the stagnation temperature was nominally 296 K. The exit velocity of the jet was computed to be 399 m/s from isentropic theory. The flow was seeded using ethanol vapor injected upstream of the stagnation tank which would condense out and form small particles (on the order of 50 nm in diameter) at the jet exit. In order to verify the measurements made with PDV, profiles across the jet were measured with a two-component LDV system.   The LDV system utilized the green (514.5 nm) and the blue (488 nm) wavelengths from an argon-ion laser and a TSI color-burst system was used to compute the Doppler shifts. The collection angle for the two components was 15 degrees from the forward scattering axis.   From these two-component LDV measurements, it was possible to find the mean velocity component in the direction measured by the PDV system. Three traverses through the jet axes were taken at three axial locations that corresponded to the regions in the PDV imaged area. These traverses were at axial locations of 3, 5 and 7 jet diameters. The flow was seeded with 0.5 µm aluminum oxide

particles. In the measurement results section and in the error analysis to follow, comparisons will be made between the PDV and LDV results.

The delta wing experiments were performed at the Subsonic Aerodynamic Research Laboratory (SARL) wind tunnel in the Air Force Research Laboratory's Air Vehicle Directorate at Wright-Patterson Air Force Base (WPAFB). Figure 5.2 gives a schematic of the entire facility. It is an open-circuit, low-speed wind tunnel with a 3.05 x 2.13 m test section. In the inlet, a movable smoke-generating rig utilizing Rosco theatrical fog (primarily propylene glycol) was available to seed the flow. This seeding apparatus permitted the seeding of a stream tube in the flow having an approximate area of 500-1000 cm^2. Based on comparable seeding systems used in other studies, the seed particles were expected to have diameters characterized by a log-normal probability distribution with a most likely diameter on the order of 1 μm. [18,4] Thus, the scattering for the large scale wind tunnel experiments was expected to be in the Mie regime.

5.2. Single Velocity Component Measurements

In order to initially evaluate the PDV system developed as part of this program there were two flow fields utilized to evaluate the error and sources of uncertainty in laboratory and large scale environments. The laboratory scale facility utilized was the supersonic jet facility described previously. This facility provided a known flow which was used to identify system errors, test system programs, and evaluate measurement uncertainty. The first large scale experiment which was utilized to access the applicability of the PDV system to large scale wind tunnel environments was empty tunnel experiments. The empty tunnel experiments were followed by a 70° delta wing at an angle of attack of 23 degrees. Initial experiments focused on accessing the initial accuracy of the technique and determining improvements before attempting multiple component tests. First, results from the single component test are described.

Table 5.1 lists some of the important parameters for the PDV system as it was arranged for the single component jet and wind tunnel experiments. Some of the quantities listed here will be referred to in the uncertainty analysis to follow. The laser tuning coefficients are characteristics of the seed laser. They were determined by comparing a scan of the laser to the model of the iodine spectrum supplied by Forkey et al.[15] The angle ϕ between the laser propagation direction and the scattering direction is a right angle in the jet experiments and just slightly obtuse in the wind tunnel experiments affording relatively flat views of the laser sheet.

The angle Ω specified in the table assumes that the velocity vector in the jet case is directed entirely along the jet axis, a good assumption for the mean flow in the center of the jet. For the wind tunnel case, the angle Ω is specified only for the empty tunnel measurements when the assumed direction of the velocity vector is in the downstream tunnel direction. The next two listings in the table are the relative errors in velocity per degree of error in the angular measurements. It is seen that the choice of ϕ is a good one from the point of view of error propagation because the velocity measurements are relatively insensitive to small errors in ϕ. In the wind tunnel however, Ω is not well chosen to measure the free-stream velocity. A different PDV system geometry would be selected if that were the goal of these experiments. As implemented here the resolution of the PDV technique was 0.16 mm for the jet facility and 0.98 mm for the wind tunnel facility. The slopes of the frequency functions give an indication of a lower limit on the frequency (or velocity) range measurable by the system. The wind tunnel arrangement has a range on the order of 440 MHz (140 m/s) compared to 610 MHz (230 m/s) for the jet arrangement.

5.2.1. Single Component Small Scale Jet Experiments

To demonstrate its capabilities, the PDV system was tested on a small-scale jet. This flow field was selected because it was expected to offer a minimum of complications. It could be well seeded (at least in the core) so that high signal levels were achieved. It provided easy optical access with very little secondary scattering from the flow facilities. The apparatus itself was relatively small and the PDV system and laser could be isolated from the flow facility so that the effect of vibration was negligible. In addition to measuring the mean flow velocities, instantaneous measurements were attempted so that the effects of large-scale structures on the jet velocities could be discerned and so that measurements of fluctuations could be made.

The flow was seeded with ethanol, which was injected into the stagnation chamber. Initially, this ethanol evaporated in the stagnation chamber. As the static temperature dropped in the accelerating flow of the nozzle, the ethanol formed small particles of condensate, which served as the seed particles. It was estimated that the particle size was on the order of 30 nm, based on similar experiments by other researchers.[19],[20] These particles were far smaller than the wavelength of the incident light, 532 nm, and so the scattering was in the Rayleigh regime ($d/\lambda < 0.1$). The laser sheet contained the axis of the jet, with the direction of laser propagation

72

making an angle of 10.1° with the jet axis. The scattering direction was normal to the laser sheet. The direction of PDV sensitivity, based on this geometry, was 0.697i+0.123j-0.707k, as seen in Figure 5.1. The measured velocity component was at an angle of 45.8° with the jet axis.

Results are first presented for the Mach 1.36 jet. Figure 5.3 is an example of the signal and reference images for an instantaneous velocity measurement as well as the resulting velocity image. Flow is from bottom to top and the imaging region extends from x/D=2.22 to x/D=7.91. For these measurements, the laser was tuned to the low frequency shoulder of the absorption line. One explanation for this decision has already been given: this side of the line has a shallower slope, resulting in a wider range of measurable frequencies (and velocities), and this is desirable in a high-speed flow. It was also thought that because of seeding considerations, measurements in the shear layer would be more successful using this scheme. The seed species was ethanol condensed by the cold jet core. The jet mixed with ambient air towards its periphery, which diluted the seed, and warmed as it slowed. This caused the ethanol seed to evaporate and shrink. It was expected that the reference signal levels would be lower at the edges of the jet and the filtered signal levels, correspondingly, even lower. It therefore seemed preferable to make the low-speed, low-signal region of the flow the high transmission region to ensure that adequate signal was seen through the filtered camera. This was accomplished by tuning to the low-frequency shoulder. The three images of Figure 5.3 show the basic patterns that have been described. In the reference image, slow-speed regions appear to yield lower signal levels. In the filtered image however, these same slow-speed regions yield higher signal levels. Note particularly that the bright structure to the left of center in the signal image corresponds to low-speed flow in the velocity image.

Figure 5.4 gives four examples of instantaneous velocity measurements by the PDV method in the jet together with the velocity gray scale. The unsteady large-scale structures in the flow are quite evident. Regions of relatively low and high velocity are seen where the jet core is first compressed and then expanded by structures at the periphery of the flow. The periphery of the flow is rather sharply delineated. These sharp features are partly a characteristic of the flow (the large-scale structures) and partly a result of thresh-holding. Thresh-holding was applied when the images were divided to produce the transmission ratios. When the filtered and reference image intensity dropped below 2000 counts, that pixel was set to 0 in the velocity image.

Figure 5.5 gives the average velocity based upon a series of 100 instantaneous images. The direction of PDV system sensitivity was 0.697i+0.123j-0.707k, which meant that the measured velocity component made an angle of about 45.8° with the jet axis. Fluctuations in either the magnitude or direction of the jet velocity were sensed by the PDV system. On average, however, the jet velocity direction was assumed to be axial, implying that the average PDV measured component had a magnitude equal to 69.7% of the magnitude of the full velocity vector. Also shown in Figure 5.5 are plots of the velocities across jet diameters at three axial stations (3, 5 and 7 x/D). Both PDV and LDV measurements are presented. Average values of the velocities as determined by PDV and LDV at each station are given in Table 5.2. It is seen that these values are in good agreement at all locations, having values within 6% of each other. Averaging over the three stations, the core velocities for the jet were 260.7 m/s by LDV and 254.3 m/s by PDV, these values agree to within 2.4%. Both techniques yield mean core measurements that are considerably below the value obtained from isentropic theory for the Mach 1.36 jet, 278m/s. This may be because the nozzle was not running quite at design or because of the effect of losses a few diameters downstream of the exit. Both methods confirm the expected loss of core velocity with downstream position.

Immediately downstream of a jet exit, there is a top hat profile characterized by a broad core of nearly uniform velocity with a thin shear layer around the circumference in which the velocity drops quickly to the ambient value. Further downstream, the shear layer thickens and the top hat region becomes smaller and smaller. Both measurement techniques showed this expected decay of the velocity profile as the shear layer expanded into the core of the jet.

Despite our strategy to obtain adequate signal levels at the edges of the jet, acceptable PDV data did not extend very far into the shear layer. Two explanations are proposed. First, the previously discussed volatility of the PDV seed species, ethanol, resulted in diminished signal strength, particularly at this modest supersonic Mach number. Second, the intermittent nature of the shear layer meant that even with adequate seeding, a high percentage of the images might not contain velocity data at the edges of the shear layer. With only 100 images, we could not be assured of having enough valid data points to obtain accurate mean readings very far into the shear layer. It should be noted that this weakness in the present measurements is not a limit of the PDV system itself, but more a characteristic of the seeding available at the time of the test. The LDV technique was much more successful at measuring into the shear layer because it

suffered from neither of these problems. With LDV, the seed species were 0.5 μm aluminum oxide particles which had no thermodynamic sensitivity. Furthermore, many more data points (about 5000 as opposed to a maximum of 100) contributed to each mean reading in LDV. Therefore, the LDV measurements did extend far into the shear layer. In defense of PDV, both McKenzie and Smith have shown that with thermodynamically insensitive seeding, PDV can also resolve jet velocities throughout the shear layer.[19,20] For seed, McKenzie used smoke generated from a commercial fog fluid, and Smith used sheared pyrogenic anhydrous silica.

Figure 5.6 gives the RMS velocity measurements obtained by PDV along with plots of the RMS velocity obtained by PDV and LDV at the previously given axial stations. The image and the plots show the expected trend of a lower turbulence level in the core with increasing turbulence levels as the periphery of the jet is reached. Note that fewer points were used to calculate the RMS velocity in the shear layer than in the core. Again, this is because of the intermittent nature of the shear layer. From the LDV measurements, it can be seen that the centerline turbulence increases with downstream distance. The PDV results agree relatively well with the LDV results at the $x/D = 7$ station. As we move upstream, the LDV method shows that the centerline velocity fluctuations fall to about 4 m/s. The PDV measurements follow the LDV results fairly well off the centerline, but apparently reach a minimum of about 9 m/s. As discussed in the error analysis, this minimum is believed to represent a combination of the noise of the measurement technique and the true fluctuation in the flow added in quadrature. The noise in the Doppler shift measurement corresponding to this minimum velocity fluctuation would be about 24 MHz.

The PDV technique was able to reveal instantaneous structure in the Mach 1.36 jet, measure mean core velocities in the jet to within 2.4% of the value obtained by LDV, and show the turbulent structure of the jet via statistical measurement. These RMS measurements were limited by PDV system noise to a minimum of about 9 m/s.

5.2.2.   Single Component: Large Scale Wind Tunnel Experiments

Much of the interest in PDV is rooted in its presumed ability to provide high spatial resolution measurements in large facilities, such as the big wind tunnels of industry and government. One purpose of the tests in the Subsonic Aerodynamic Research Laboratory at Wright Patterson was to confirm this presumption. The delta wing flow field was selected

because of the interest described previously in understanding the interaction of leading-edge vortices with tails. Furthermore, our collaborators at Wright-Patterson could provide a model and test conditions for which computational fluid dynamic results had been previously obtained.[21,22]

The model was a 70 degree sweep delta wing with sharp leading edges, set at an angle-of-attack of 23 degrees. Measurements were obtained on the wing at four different chord locations (85.7, 97.1, 102.9, 114.3% chord) at a free-stream Mach number of 0.2. This corresponded to a free-stream velocity of 68 m/s. The Reynolds number based on the root chord was 1.87×10^4. At this condition, no vortex bursting was present over the model surface.[23] Measurements were also made of the same model equipped with vertical tails shaped like those of the F-15. These tails had a 35° leading edge sweep and an unswept trailing edge. Their trailing edges were aligned with the trailing edge of the wing and their position was chosen to lie along the vortex core trajectory for the clean delta wing. Further details of the model are available from Beutner.[21] These measurements were made at the same chord locations, angle-of-attack, and free-stream velocity as the measurements for the clean wing.

As seen in Figure 5.7, the laser sheet was oriented span-wise across the tunnel with a propagation direction normal to the surface of the model. The direction of PDV sensitivity, based on this geometry, was -0.210i-0.003j+0.978k. The velocity component measured was thus predominantly vertical and slightly upstream. Note that this direction was chosen because its velocity component was strongly affected by streamwise vortices and was the simplest to implement in the tunnel with the current optical access.

Prior to measuring the complicated flow above a delta wing, measurements were made in the wind tunnel without a model in place at Mach numbers of 0.2 and 0.3. The empty tunnel velocities correspond to velocities of 68 and 96 m/s. Here the purpose was simply to gain some insight into the system performance at this new scale. The expected velocity components in the direction of PDV sensitivity and the measured velocity components are given in Table 5.2 and discussed in the error analysis. In terms of mean velocities, the differences between measured and expected values were 1.7 m/s and 0.5 m/s for the Mach 0.2 and Mach 0.3 cases, respectively. In terms of frequency, these differences amounted to 5.3 and 1.6 MHz and in terms of relative error they amounted to 12% and 2.5%, respectively. These latter values may seem unacceptably large, but we should note that the PDV system was not optimized for stream-wise velocity

measurements. The component of the free-stream velocity measured was quite small (14-20 m/s), meaning that a constant error that might be acceptably small relative to a larger velocity component would produce a large relative error in this context. An analysis by Beutner et al. (1998) using the same data set, but with independent data processing routines, yielded similar results.[21] In the empty wind tunnel, turbulence was expected to be less than 0.1%; therefore, any significant RMS measurement of velocity could be attributed almost entirely to PDV system noise. RMS velocity fluctuations in the wind tunnel for the Mach 0.2 and 0.3 flows were 3.8m/s and 3.0 m/s. These measurements were based upon 75 and 61 images, respectively.

Figure 5.8 shows instantaneous PDV measurements above the 70° sweep delta wing at a 23° angle-of-attack at Mach 0.2. These measurements were taken at four constant chord locations approximately normal to the wing. As indicated previously, the measured component was primarily in the vertical direction with a small upstream component. Each of the instantaneous images clearly shows the vortex structure that is characteristic of the flow over a delta wing at an angle-of-attack. The strong negative velocities are indicative of the large streamwise velocity component in the vortex core (the jet-like behavior) coupled with a large downward component on the inboard side of the vortex. Furthermore, the strengthening of the vortices with streamwise location is also evident as expected in a leading-edge vortex on a delta wing. The variation in the regions of the images where velocity data is presented was caused by the movement of the seed. The four images presented here were selected because they had relatively full seed distribution. The most heavily seeded regions of the flow tended to be the cores themselves where natural condensation was present in addition to the smoke. Other regions had intermittent seeding from the smoke generator. So much seed was concentrated in the cores, in fact, that secondary scattering was visible upstream of the light sheet. This secondary scattering may have biased data in some regions of the imaging plane. In the first three images, the delta wing itself is in the field-of-view. No reliable data can be extracted from these regions due to the strong scattering from surfaces. Similarly, the sting supporting the wing corrupted the data in the center of the flow field. Nevertheless, large areas of the imaging region were available for velocity measurements.

Figure 5.9 to Figure 5.12 show averaged PDV measurements at the locations described above based on 50, 50, 62 and 59 images, respectively. A plot of the velocity along a line drawn through the cores is also given for each image. The nearly linear region in these profiles is

indicative of the vortex cores. The trajectories of the vortices can be calculated based upon the average images that are located above the model, Figure 5.9 and Figure 5.10. The vortex angle of inclination, α was found to be approximately 7°, and the vortex sweep angle, Λ_c, α_c was found to be 76.5°. The latter angle was in agreement with a value inferred from Beutner [21] to within 0.7°. It is not surprising that the physical locations of the vortex trajectories should be found in agreement. This agreement confirms that the spatial scales have been calculated correctly. The strengthening of the vortices that was seen in the instantaneous images is also seen here. Compared to the instantaneous images, the average images show greater fill, but it should be remembered that the values far from the cores are based on fewer measurements than those near the cores because of the inconsistent seeding. Note that far from the cores, the PDV measured value approaches the value obtained in the empty tunnel run at Mach 0.2. A CFD solution using the Baldwin-Lomax closure model was obtained by Rizzetta for a similar flow field. This result is shown beneath each of the PDV measurements.[22] The overall flow structure and the ranges of velocity found in the flow are in approximate agreement, but the vortex core diameters measured by PDV are only one-third to one-half what the CFD solution indicates. This may be due to the insufficient grid resolution in the CFD solution or failure to adequately model secondary separation on the delta wing.[21] Note, finally, that in both the PDV measurements and the CFD solution, the free-shear layer can be observed rolling up from the leading edge of the wing in the results at 86 and 97% root chord. In the former case, the roll up occurs at approximately the 14± cm position and in the later case at ±15 cm.

Figure 5.13 to Figure 5.16 show average PDV measurements for the case with tails at the same chord locations as seen in the clean delta wing case. These measurements were based on 89, 45, 82, and 48 images for the respective cases. The tails were located along the projection of the vortex core trajectories on the wing surface. Flow visualizations by Beutner indicated that vortex bursting occurred at approximately the mid-chord location on the wing. Thus, the measurement planes of the current experiment were downstream of the mean burst location.[21] The bursting, characterized by a dramatic growth of the vortex cores, is a result of the presence of the tails although it occurs well upstream of them. These images show a much more diffuse vortex structure, which is consistent with the vortex bursting. No comparison with CFD results is presented here because the CFD solution was not able to predict the burst location correctly and thus was fundamentally different from the physical flow. It is interesting to note that a rather

strong positive z-component of velocity exists on the inboard surface of the tails, suggesting that the vortex trajectory, although burst, passed predominantly inboard rather than outboard of the tails.

In the large-scale facility, the PDV technique was able to produce mean measurements accurate to within 1.7 m/s in the empty tunnel. The technique also produced mean measurements of the complicated flow-field above a delta wing at an angle-of-attack, with and without tails. These measurements were made in an environment that was challenging from the points of view of flow seeding, vibration and scale. Chiefly because of the inhomogeneous and fluctuating quality of the seeding combined with the small data set, statistical measurements of the temporal flow variation were not successful.

5.3.   Multiple Velocity Component Measurements

Once the single component tests were conducted and evaluated, the PDV system and programs were expanded so that multiple velocity components could be measured simultaneously. Measurements were first conducted in the small supersonic jet facility described previously and then conducted in the large scale wind tunnel facility. The jet experiments were unique in that only two PDV camera systems were utilized and the computation of the third velocity component was made possible by utilizing two laser sheet orientations. In addition, the jet was forced using laser excitation so that the large scale turbulent structures in the shear layer could be measured. Three component tests which were performed in the large scale wind tunnel on the the 70° Delta wing model at a 23° angle of attack resulted in the ability to compute two velocity components. Although the third velocity component could not be computed (due to reasons which will be described shortly) the feasibility of multiple component measurements in a large facility was still demonstrated and uncertainty evaluated.

5.3.1.   Small Scale Multiple Velocity Component Jet Experiment

The PDV multi-component measurement system was applied to the small scale supersonic Mach 1.36 jet. These experiments allowed us to confirm the ability to resolve three velocity components using the PDV system developed and has been described in detail by Crafton, Elliott, et.al.[24] Figure 5.17 shows the experimental arrangement used for the jet study. The arrangement utilizes two PDV camera systems and two laser light positions so that all three

velocity components could be resolved. In order to obtain three mean velocity components from two PDV camera systems, two orientations of the incident laser directions were used in the study. The PDV camera positions were kept the same for both laser sheet arrangements. The combination of this data results in three independent system sensitivity vectors. Table 5.3 gives the incident, observation, and optical difference vectors for the arrangements used in this study. The SR boxcar integrator and computer interface was again used to control the laser, calibrate the iodine cells, and monitor the laser frequency. The data collection software described previously allows the frequency of the laser to be recorded with each data shot which was stored in a log file. By automatically monitoring the BUT, data shots were not stored if the laser was unseeded. The PDV data was analyzed in the same procedure as outlined previously. Once the Doppler shifts were calculated for each vector, the three velocity components could be calculated using equation 4.15.

Similar to the single component measurements, the jet was seeded with ethanol vapor which condensed in the free stream forming small particles (~50 nm) which could accurately follow the flow features. The jet was operated at Mach 1.34 with a stagnation temperature and exit velocity (based on isentropic theory) of 300K and 399 m/s respectively. In addition to measuring the perfectly expanding supersonic jet using the three component PDV system, measurements were also taken of the large scale structures induced in a supersonic shear layer using laser energy perturbation. This is accomplished by focusing a second laser beam to perturb the shear layer at the exit of the nozzle with approximately 30 mJ in a 10 ns pulse from a second Nd:YAG laser. The interrogation laser beam is then delayed (by 170 and 220 μs) from the perturbation pulse. This allowed the formation of a large scale structure in the shear layer to be controlled so that PDV phase averaged three component velocity measurements could be obtained. This not only was a good laboratory scale experiment to test the PDV system and data reduction routines, but also is an interesting flow field to quantify the evolution of the large scale structure as it convects downstream.

Figure 5.18 shows the streamwise velocity component for the unexcited jet. The maximum streamwise velocity is approximately 410 m/s which is slightly higher than the isentropic value. This is due to the presence of the shock/expansion diamonds which are observed in the jet core caused by the operating pressure being slightly high and therefore the jet is under expanded. The out of plane velocity component was computed to be nearly zero as

expected. Figure 5.19 shows the comparison of the mean and RMS streamwise velocity measured using PDV and compared to the LDV data taken in the same flow field at a position of z/D =3 downstream of the nozzle exit. As shown, the agreement between the mean measurements is excellent, but the RMS measurements are slightly low in the shear layer region similar to the single component measurements. This is most likely due to the fact that the seeding is provided by condensation particles which may slightly bias the instantaneous measurements since it does not mark the atmospheric air that the jet exhausts into. This should be considered as a problem with the seeding available for this jet experiment and not a problem with the PDV measurement system. The RMS is slightly higher in the core region of the jet most likely due to speckle noise in the images.

Figure 5.20 shows three component velocity measurements for the Mach 1.34 jet with laser excitation. The measurements were taken 170 μs and 220 μs after the initiation of the laser perturbation pulse. The color contours indicate the out of plane velocity component with the vectors indicating the streamwise and spanwise velocity components (with the convection velocity subtracted from the streamwise component). Clearly visible is the large scale structure that is formed on the shear layer shown to the right. The PDV technique had the required sensitivity to capture the change in the core velocity due to the growing structure. Additionally one can observe the change in the spanwise component of velocity, which indicates that a vortical structure is present. For the later time the velocity field shows the effect of the large scale structure as it convects downstream and grows as it encompasses more fluid from the jet core and atmosphere.

This experiment demonstrated that a three velocity component measurement could be made using PDV, but it should be emphasized that this is an extremely simple flow to measure. This is due to the absence of walls or windows and the environmental conditions associated with the tunnel. Walls and windows cause background intensity difficulties and the wind tunnel environment introduces problems such as vibration, noise, and temperature fluctuations.

A similar uncertainty analysis as was conducted previously showed that the random plus total uncertainty for the three component test was 17 m/s. This uncertainty is dominated by speckle noise with an uncertainty in the mean measurements reduced by about 10 m/s from this level. The error reported in the mean measurements compared to isentropic theory was approximately 7.2 m/s which is less than 2% of the jet core velocity.

81

5.3.2.   Large Scale Multiple Velocity Component Delta Wing Experiment

Figure 5.21 gives the camera arrangement used in the multi-component PDV test, which was conducted in the SARL wind tunnel on the 70° Delta wing model at a 23° angle of attack. Two coordinate systems are shown. First is the tunnel coordinate system (x, y, z) with the downstream direction aligned with the x axis. Second is a model normal coordinate system (x', y', z') rotated about the y axis to align with the model at 23° angle-of-attack. PDV data was taken at five streamwise positions (although data was corrupted for one case), as well as, runs with the model moved away from the measurement plane to provide "empty tunnel" data for an error estimate. Table 5.4 and Table 5.5 give the observation unit vector for each camera component ($\underline{k}_{o1}$, $\underline{k}_{o2}$, $\underline{k}_{o3}$) and incident light unit vector ($\underline{k}_i$). These tables also include the system sensitivity vector $\underline{k}_{oi1}$, $\underline{k}_{oi2}$, $\underline{k}_{oi3}$ for each camera view at the two upstream and two downstream locations. The system sensitivity vectors are given in both tunnel (x, y, z) coordinates and model coordinates (x', y', z'). The laser and camera viewing angles were chosen so that the views would be clear of any surface reflections from the delta wing model. While this solved one problem, it created an unforeseen problem for data reduction. The tunnel was operated at Mach 0.2 for all the measurement locations resulting in a free stream velocity of approximately 68 m/s. PDV data was taken at four streamwise measurement locations, 62.8%, 85.7%, 97.1%, and 108% as percentages of the chord length.

Figure 5.22 to Figure 5.24 show the average velocity images measured parallel to the PDV system sensitivity for each camera component with the vectors of PDV sensitivity (k_{oi}) given in Table 5.4 and Table 5.5 for each component. Note that the vectors change slightly for the two upstream and downstream positions due to the need to move the laser sheet to cover this range of streamwise positions. For all cases, the laser propagation direction was the same and the scales on the images are such that the view is always looking upstream from behind the model. Z' = 0 is measured perpendicular from the model surface and Y' is measured from the center of the tunnel. The first PDV component was placed above, upstream and to the side of the model (see Figure 5.21). Looking at the parallel velocity computed from component #1 (Figure 5.22) the vortices are clearly visible with the cores positioned spanwise at approximately ± 7.0 cm at 62.8% root chord and expanding to ± 11.0 cm at 108% root chord. Since the streamwise velocity component is negative, the freestream velocity appears negative and the vortex cores have about twice the value of the freestream velocity as expected. Due to the rotation of the

82

vortices, the top and bottom indicate higher and lower velocities. One disturbing feature is the strong lower velocity indicated by small diameter circles (~ 2cm in diameter) around each vortex core. This is likely due to some image alignment mismatch between the reference and signal cameras. This region of the vortex is has a very discrete edge due to the high amount of seeding from constant condensation particles occurring in the vortex. This sharp edge therefore amplifies any difficulties which may occur in image alignment. After the test was completed it was found that this view had a loose mirror and so this problem is not totally unexpected. Fortunately, this camera view was not needed in the subsequent analysis when the components are resolved.

The second PDV component was located downstream and slightly lower in the tunnel (see Figure 5.21 for orientation) with the velocity parallel to system sensitivity given in Figure 5.23. Now we can see that the free stream is positive and the velocity is maximized in the core of the vortex as expected. Note that rings observed previously are no longer apparent indicating that the signal and reference camera alignment remained in tack during the test. The growth of the vortices is clearly visible as downstream locations are traversed. There is a slight velocity gradient from the top to the bottom of the vortex, but the velocity is strongly dominated by the increase in velocity in the vortex core. The bottom of the left vortex in the image shows a much greater decrease in velocity than the right vortex. Many different processing parameter variations were investigated and no change in this result was indicated. It was surmised that the most likely explanation was that this viewing angle was actually viewing the bottom portion of the vortex through the downstream portion of the vortex core. Since there is always strong condensation in the vortex core the intensity was sufficiently decreased since at this viewing angle we are practically looking through the vortex core instead of across it which has much less effect.

The third PDV component was located to the side upstream and above the model (see Figure 5.21 for orientation) with the resulting parallel velocity given in Figure 5.24. Again, the velocities are negative in the free stream due to the x direction of PDV system sensitivity. The two vortices are again clearly visible. This PDV velocity component however is dominated by the spanwise velocity, the effects of which are much more evident in this view where the vortices appear more distinct. It should be noted however, that there is again some asymmetry in the apparent strength of the two vortices. This could be due to the change of observation vector across the image, but may also be caused by asymmetry in the model orientation in the tunnel.

Additionally it is observed that there is very little vertical velocity component difference in all three components since only the effect of the vortex on the streamwise and spanwise component is evident. As indicated in the discussion of these three velocity components, it is very difficult to highlight details of the flow since the components are not aligned with any normal axis. Features of the free stream and flow structures (i.e. vortex) combine in ways that make it difficult to separate these effects. This is one of the main criticisms with PDV and is what motivates the desire to reduce the data to components relevant to the flow field. It should be noted however that the "oblique" velocity components are still useful for validation of CFD modeling since they can be easily computed from single or multiple components.

The goal of using multiple viewing angles in PDV is to resolve three velocity vectors in a coordinate system which is "natural" to the flow being measured. Using three cameras it should then be possible to compute three velocity components using the methodology described previously associated with Equation 4.16. Unfortunately for the present case this was not possible since the $\det[K_{io}]$ is nearly zero. This was not realized until after the test was conducted and was an unfortunate mistake. If the determinate is nearly zero (which it is -0.017 for our present case) then the three equations with three unknowns are unsolvable. Another way of considering this is to observe that rows 1 and 2 can be added together to form row three (2*row 1 + row 2 = row 3) therefore the system sensitivity vector is not independent for the three views. This can also be realized by considering that the incident and observation vectors all lie in a plane and therefore there is no sensitivity to the velocity component out of the plane. This geometry was intentionally selected to reduce background reflections. Unfortunately these aspects are obvious in hind sight and were avoided in future tests.

With this problem in mind, however, it is possible to obtain the velocity for two components using any two camera pairs. First, a new model oriented coordinate system was defined in which X' is the axial component relative to the delta wing surface, y' is the spanwise component, and Z' is the component normal to the delta wing surface. The coordinate system, which is now aligned relative to the delta wing body at an angle of attack, is shown in Figure 5.21. This is the same as rotating the original coordinate system about the y-axis -23 degrees. Table 5.4 and Table 5.5 gives the resulting system sensitivity vectors for each PDV component. Now it is clear that all three cameras are sensitive to velocity components in the spanwise and streamwise directions with little or no sensitivity in the Z' direction, which will be neglected.

Therefore any two PDV camera systems can be used to solve for the spanwise (Y') and axial (X') velocity components using equation 4.18.

Figure 5.25 to Figure 5.28 show the axial (X') velocity calculated from the above procedure for the four axial root chord locations studied (62.8%, 85.7%, 97.1%, 1.08%) for the 70° delta wing at 23° angle of attack. The two vortices created above the delta wing are clearly visible where the axial velocity is greatly increased in the core of the vortex as expected. As the vortices evolve downstream the axial component of the core velocity decreases in magnitude, but increases in diameter. There is some asymmetry in the vortex on the left side of the image. This could be due to slower velocity under the vortex due to separation, but may be due to secondary scattering effects. This region of the vortex is viewed through the vortex core from PDV component #2 used in the computation. The behavior of the right hand vortex however, is as expected. Figure 5.29 gives the peak axial velocity in the vortex core as a function of axial distance from this data. The increase in peak streamwise velocity in the vortex core is at the level expected for this test compared to what is observed in computations (before the interaction with vertical fins which were part of the computation).[22] It is observed that the velocity in the core decreases slightly (10 to 13%) with streamwise distance and increases in size downstream as the vortex grows. Also apparent in Figure 5.29 is the fact that the lower velocity wake is observed at the off body location of 108% root chord. In addition, the lower streamwise velocity due to the shear layer created from the leading edge of the delta wing is observed outboard of the vortex core.

Figure 5.30 to Figure 5.33 gives the spanwise velocity component for the 70° delta wing at 23° angle-of-attack. The spanwise velocity clearly picks up the velocity gradient one would expect at the top and bottom of the vortex. The directions and magnitudes of the velocity are within the expected range. There may be a slight bias in the lower portion of the left vortex since this portion of the vortex is viewed through the vortex core itself. Again, the right vortex seems to be more uniform showing no evidence of having problems. The spanwise velocity also captures the vortex growth in diameter and spreading rate as they propagate downstream as expected.

It is clear from the above results that two independent velocity components have been successfully resolved in the large scale facility. Another interesting test is to utilize different green card images (i.e. the empty tunnel running green card) and observe any changes in the

computed velocity field. Figure 5.34 compare the axial and spanwise velocity calculated with the standing green card and empty tunnel (model pitched down away from the field of view) running green card images for the 108% chord location. There is very little difference in the two approaches indicating that the running green card, which are the less difficult to acquire, may be sufficient for future tests. In general however, more calibration options can aid in problem solving.

Another method to process the data for comparison is to use different PDV camera locations to compute the axial and spanwise flow velocities. Figure 5.35 gives the velocities calculated from the three PDV camera location combinations (1&2, 2&3, and 1&3) for the 108% chord location. When component 1 (which had some alignment problems) is utilized, there is more variation or noise observed in the results due to mapping misalignment problems discussed. The axial and spanwise components calculated from PDV components 1 and 2, however, show approximately the same trends in the velocity induced by the vortices as discussed above.

One useful flow field that serves as a check to the accuracy of the PDV measurement system is to run the wind tunnel without a model in the measurement plane (i.e. empty tunnel tests). Although this provides a known flow field to measure, we should recognize that it avoids some of the difficulties associated with a model including obstructions and surface reflections. Figure 5.36 shows the axial and spanwise empty tunnel velocity measurements from the current set of experiments. The average freestream tunnel velocity in this coordinate system is 66.9 m/s with a standard deviation of 1.6 m/s. Transforming the (69.2 m/s) freestream velocity into this cordinate system one would expect to measure an axial (X') velocity component of 63.7 m/s which is a difference of 3.2 m/s or 5%. The average spanwise velocity component is expected to be zero and is measured to be -4.8 m/s with a standard deviation of 1.9 m/s. This is slightly more than is expected and may be due to the angle variation across the image or incorrect measurement of unit vectors. Otherwise this appears to be consistent with our earlier findings from single component measurements that the PDV system is capable of measuring velocities within approximately 2 m/s.

5.4.   Aircraft Model Investigations

In addition to the large scale wind tunnel tests of the delta wing at an angle of attack, two other models have been studied in the SARL facility as part of the present study. The goal of

these studies was to investigate the feasibility of utilizing PDV to measure the flow field around more complex models. The complex models are of interest since viewing may be obstructed by control surfaces or the presence of a canopy or fuselage causing additional surface reflections and contaminate the image. Here we will describe just a few of these results with further details given in the conference and journal papers that were written.[21,24,25,26,27,28,29,30]

5.4.1.   Boundary Layer Interference Model

The first is the Boeing Boundary Layer Interference Model (Figure 5.37). This model has a complex geometry with a fuselage, high aspect ratio main wing, and a highly swept strake. PDV was used to investigate the interaction of the forebody vortex, strake vortex, and wing flow field. Measurements were taken at an angle of attack of 20 degrees with the laser sheet propagating from the top to the bottom of the wind tunnel at an angle of 15 degrees. Two systems were utilized to make two component PDV measurements. The first PDV system viewed the laser sheet from upstream and to the top of the model with a system sensitivity unit vector of (-0.273i, 0.0j., 0.926k). Figure 5.38 shows PDV measurements on a full-span plane, 3.8 cm upstream of the wing-strake junction and 10.2 cm downstream of the wing-strake junction. The strong vortex which has developed off the strake leading edge, can be seen and has already coalesced with the weaker forebody vortex. The dominate velocity component in this view is in the vertical (Z) direction. The system sensitivity vector brings out the left and right vertical velocity distribution (as opposed to the spanwise velocity identifying the vortex in the 3D Delta wing measurements discussed previously). As the vortex pair propagates downstream 10.2 cm past the wing strake junction, the vortices are still identifiable. After interacting with the pressure gradient fields over the wing however, the vortex weakens in strength (i.e. the velocity difference left to right is more spread out). The background scattering from the wing and model have been reduced in this view by adjusting the filtered and nonfiltered background levels until no discontinuities are observed. However, scattering from the laser beam focused onto the model still causes problems as observed at the bottom of the image.

The second PDV view is from the side and upstream of the model with a system sensitivity vector of (-0.304i, 0.406j, 0.848k). The same view and streamwise locations were measured with this PDV velocity component. These results are presented in Figure 5.39. Note that the same vortex structure is observed, but now there is a spanwise component to the vortices.

Instead of having a vertical velocity gradient, the gradient is angled at approximately ±40 degrees. Again, it is observed that the vortex decreases in strength as it propagates downstream and increases in diameter. It is interesting to note, however, that the velocity gradient across the leading edge shear layer for the upstream strake position is evident as it interacts with the vortex. These measurements were able to resolve complex flow interactions with multiple vortices and multiple lifting surfaces. This test demonstrates another significant motivation for developing the PDV instrument. For complex flow fields, PDV can provide fast, detailed measurements of complex flow interactions, particularly vortices. The resolution of these flow fields by point-measurement techniques would require prohibitively long test times, and the complexities of the flow fields are at the edge of the typical Reynolds-averaged CFD codes used in industry. Therefore, PDV represents a powerful tool not only for the CFD developer, but also for the aircraft designer. The PDV data shown here is a small fraction of the total data taken for this test, which is described in further detail by Beutner et al.[30].

5.4.2.　56° Delta Wing Aircraft Model

A second aircraft model tested in the SARL wind tunnel facility as part of this program was the 56° delta wing generic fighter configurations shown in Figure 5.40. Images and discussion given here summarizes the results from the article by Beutner, Elliott et al.[29] In this paper, a full analysis of this flow field is given with a description of the data analysis program used. This model had a realistic body including, a canopy and vertical tail and interesting fluid dynamic interactions with strake cortex and wing vortex systems. Although the configuration does not represent any aircraft currently or previously considered, it does have several features that are interesting from a fluid dynamics viewpoint (i.e the interactions of strake and leading edge vortices which will be observed shortly). The model was tested at a 23° angle of attack at Mach 0.2. Four different streamwise views were measured in the present study two of which are indicated in Figure 5.40. The sheet had a general propagation from the top to the bottom of the wind tunnel. Two PDV measurement locations were utilized in this test, one was mounted on the top of the tunnel having a PDV sensitivity vector of (-0.253i, 0.0 j, 0.968k) and the second viewing angle, mounted to the left of the model resulting in a PDV sensitivity vector of (-0.296i,0.421j,0.857k).

Figure 5.41 shows the PDV velocity data for top and side PDV detector locations for the location streamwise location 108mm upstream of the wing/strake junction (location A). Clearly visible from both PDV components is the velocity field imposed by the strake vortex which results in a velocity gradient across the vortex indicating its rotation imposed on the flow. It should be noted that there is some data dropout due to the surface scattering of the laser beam as it strikes the model, but the effect of the vortex on the flow field is still resolved. Figure 5.42 shows the two PDV views at a streamwise location corresponding to the trailing edge of the canopy. In general, these are the same views as before but with slightly different sensitivity vectors (due to the change of light sheet position to location B). Clearly observed is the development of the strake vortex which now has propagated outboard across the wing surface. In addition to the strake vortex, the presence of a stronger wing vortex is indicated which has developed further outboard. The PDV velocimetry data indicates the increase in strength of the wing vortex as a stronger velocity gradient across the vortex core. Later PDV locations indicate the interaction of these vortices, which burst further downstream.

5.4.3.   Boeing UCAV Model

The final aircraft model which was tested as part of PDV system development was a Boeing UCAV model which is shown in Figure 5.43. The UCAV model was a hybrid design and built by John Hopkins University Applied Physics Laboratory with an internal metal structure to withstand the aerodynamic loading and external shape constructed from a rapid prototype stereo lithography polymer. The model has a lambda wing with a span of approximately 4 feet and length of 3 feet. Control surfaces on the trailing edge were adjusted from -20 to +20 degrees for the current tests, the test configurations are listed in Table 5.6. The UCAV model was provided by Dr. Charles Tyler who has conducted both computational (second order three dimensional Euler simulation) and experimental studies (i.e. aerodynamic force and moments, pressure sensitive paint, and deflection using Moiré Interferometry) of the flow field around the model.[31] The long term goal of this study is to develop new tools so that CFD and experiments utilizing rapid prototype manufacturing techniques can be combined more efficiently to investigate future aircraft designs. Measurements were taken at five measurement planes (measured along the model surface relative to the wing/body junction) as shown on Figure 5.43. Table 5.6 gives the positions of the trailing edge control surfaces which were investigated

with the measurement planes taken at each setting. Note that for all cases investigated, only four out of the five measurement planes were computed. This was due to experimental difficulties, seeding, or time constraints which limited the number of planes and number of images taken for each case. All the experiments conducted for the PDV test were at a Mach number of 0.2 (which is approximately 68 m/s for the atmospheric conditions of these experiments) and 20 degrees angle of attack measured with tunnel off conditions. Please note from the start that these should be considered preliminary measurements since we are continuing to look for improvements and resolve problems with the data which will be discussed shortly.

Three component PDV measurements were taken with the cameras arranged as shown in Figure 5.44 and incident and observation vectors given in Table 5.7. The laser beam was introduced from the top of the tunnel. The sheet made an angle of approximately 20 degrees with respect to the free stream direction. This resulted in a sheet that was oriented normal to the model axis. Two dual camera PDV systems were located on the side of the tunnel with the third camera located on the top of the tunnel. Large mirrors were utilized for all views. This allowed the cameras to be placed as close to the tunnel walls as possible and still provide an adequate normal view of the laser sheet. One would like to select camera views that result in optimized sensitivity for calculating the three tunnel oriented velocity components. The views are generally constrained however, by providing a clear view of the sheet and avoiding background reflections, and obstructions due to the model geometry. Due to the large scale of the model, semi-span measurements were taken over half the model. Spatial mapping and tie point determination was conducted similar to the delta wing utilizing a dot card. Due to previous success, running green cards were utilized for intensity calibrations of the cameras as discussed previously. Seeding was provided using theatrical smoke. The smoke was moved across the measurement plane during the test to minimize secondary scattering. If the entire tunnel were seeded, the scattering and absorption of out-of-plane particles would affect the signal and obscure the entire plane of interest.

Figure 5.45 to Figure 5.48 show the 3D velocity measurements for the streamwise planes with the trailing edge control surface set at zero degrees. Note that the black line on the model indicates the laser sheet position on the model surface. This was measured using mapped images of the laser sheet at reduced power and the model has been placed to indicate its approximate position. For the first measurement plane, located 1.0 inche upstream (Figure 5.45) of the

wing/body junction, a vortex (which we will term the inboard vortex) is clearly visible. The inboard vortex is generated by the vorticity sheet shed off the sharp 90 degree leading edge extension (or strake). The velocity induced by vortex created by the inboard vortex has a peak streamwise velocity near the core and induces typical velocity vectors in the spanwise and vertical directions reflecting the presence of the induced vorticity. Additionally the vorticity sheet is visible on the outboard side of the vortex. Moving to the next measurement location located at 3.0 inches downstream of the wing/body junction (Figure 5.46) the inboard vortex has increased in diameter significantly with the streamwise velocity of the vortex core decreasing to free stream levels. The appearance of a second outboard vortex created from the leading edge of the wing is visible. The outboard vortex has a significantly higher streamwise velocity in the core. Unfortunately, the presence of surface reflections does not enable the velocity near the surface to be completely resolved (i.e. the negative y component of the vortex). At the measurement plane of 5.0 inches downstream of the wing/body junction, (Figure 5.47) the inboard vortex continues to increase in size. At this location, the vortex has characteristics of bursting as evidenced by the large decrease of streamwise velocity in the vortex core. This velocity eventually goes slightly negative (-0.15 m/s) by the last measurement location (Figure 5.48). The decrease in the streamwise velocity of the vortex core to zero and even negative velocities has been reported by other investigators of delta wings at high angles of attack.[32] As the outboard vortex develops it grows in strength and moves further outboard, but then the velocity in the vortex core decreases by the last measurement location suggesting that it may also have burst.

Figure 5.49 to Figure 5.52 show the 3D velocity fields taken using PDV for the trailing edge control surfaces set at an angle of -20 degrees. Similar trends in the formation of the inboard and outboard vortices and resulting velocity are observed. However, both vortices appear to move slightly upward although the spanwise position is approximately the same as before and the streamwise velocity is slightly decreased. Again, a large decrease in streamwise core velocity gives evidence of bursting in both vortices by the last measurement plane (Figure 5.52). For the first measurement plane, 1.0 inch in front of the wing/body junction, the streamwise velocity of the vortex does appear to be slightly lower than the previous case. Otherwise the trends appear to be the same. A secondary vortex may also be forming beneath and outboard the wing vortex, but is obscured by the surface reflections from the model.

For the case taken with the control surface deflection angle at +20 degrees (Figure 5.53 to Figure 5.56), the velocity fields are almost identical to the 0 degree deflection angle case. This data shows initially strong vortices from the body leading edge extension and wing leading edge. Again the inboard and outboard vortices eventually grow in diameter and burst downstream as indicated by a low streamwise velocity in the core. The final configuration for which measurements were taken has a trailing edge control surface set at -20 degrees for one the side of the aircraft (left) and the control surface set at +20 degrees for the opposite side of the aircraft (Figure 5.57 to Figure 5.60). Again the same vortex structures and their development is observed which is representative of the -20 degree case described previously.

Several difficulties were faced during this test and most were resolved. The data taken during the UCAV test was by far the most difficult to process and the processing algorithms and were improved during data reduction. Two equipment malfunctions greatly decreased the amount and quality of data that could be taken. First, considering that PDV system develop utilizes six cameras for a three component measurement we had to replace three of the cameras during the test due to breakdowns which were generally associated with the mechanical shutter. In addition, due to failures of the Joule-meters during the test we were only able to scan and obtain the absorption profiles of one iodine cell at a time. Previously using the photo-diode and box car integrator system, all of the iodine cells could be scanned simultaneously. This guarantees that the absorption profiles are correct relative to each other. Since only one filter could be scanned at a time there could be a frequency shift introduced in the profiles relative to one another since there was no independent frequency reference during the scan. This was an unfortunate situation which resulted in requiring a relative shift to be placed on the filter profiles. This shift was determined by calibrating the velocity to expected levels away from the vortex in the free stream. The solution was found to require a shift of approximately 120 to 165 MHz of the reference filter profile and a shift of -5 to 55 MHz of the third PDV component filter profile. For one measurement, the second PDV component filter was shifted by –20 MHz as well. This seemed to result in the most reasonable velocity magnitudes for the three components away from the vortex (which are expected to have a nearly streamwise velocity magnitude and slightly positive vertical and spanwise components) and resolve the problem. In previous experiments, this type of "flow field calibration" was not required and therefore independent velocity measurements could be made within the uncertainties given. It is noted however that the need

for this shift was related to a calibration error. This calibration error was related to the normalization step in the filter and has been resolved. The impact on the final data was minimal so the reprocessed data was not included in the final report.

Only running green card images were taken for the present tests. In the future, it is suggested that static green card images also be taken so that errors can be more easily corrected when they occur. Although the UCAV data had more difficulties than the data previously taken, it enabled us to improve the processing programs. In order to get a good intensity calibration between the signal and reference cameras, we previously set and arbitrary intensity threshold for data to be analyzed. In the improved data reduction software, it automatically scans through the data images and determines the intensity thresholds for each pixel based on a percentage of the standard deviation. It was found that utilizing intensities in the range of 0.5 to 3.0 standard deviations from the mean resulted in the most accurate intensity calibration. Next, there has always been a problem with the cameras slightly shifting positions during a test. One can consider three problems which are introduced by image misalignment. First, he image has been shifted relative to it's own spatial and intensity calibration map. Second, the signal and reference images do not align pixel to pixel and therefore when they are divided sharp light and dark regions occur. Third, the divided images result in inaccuracies as the three velocity components are solved for from the multiple views. It turns out that the second problem is the most severe. During the acquisition of the Boeing UCAV data, one data set had a significant spatial shift in one component. For this reason, a routine was developed to conduct a cross-correlation procedure so that the images could be corrected and the data recovered. The evidence of an image shift is characterized by sharp bright and dark region or shadowing. These features result in artificially high and low velocities. After the reference image is shifted by the determined amount (~2 pixels in this case) this abnormality can be corrected.
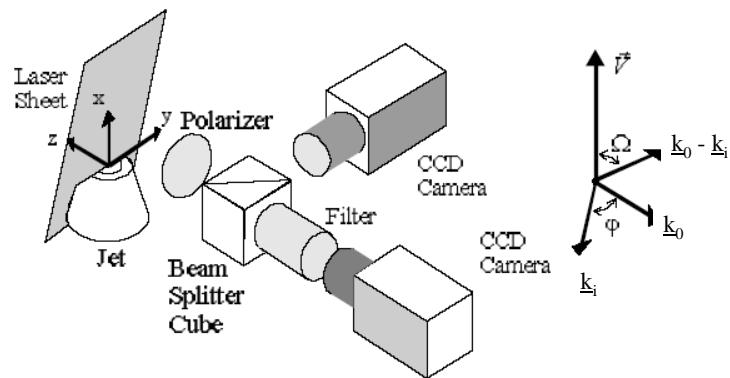
Figure 5.1 PDV arrangement and coordinate system for jet experiments.
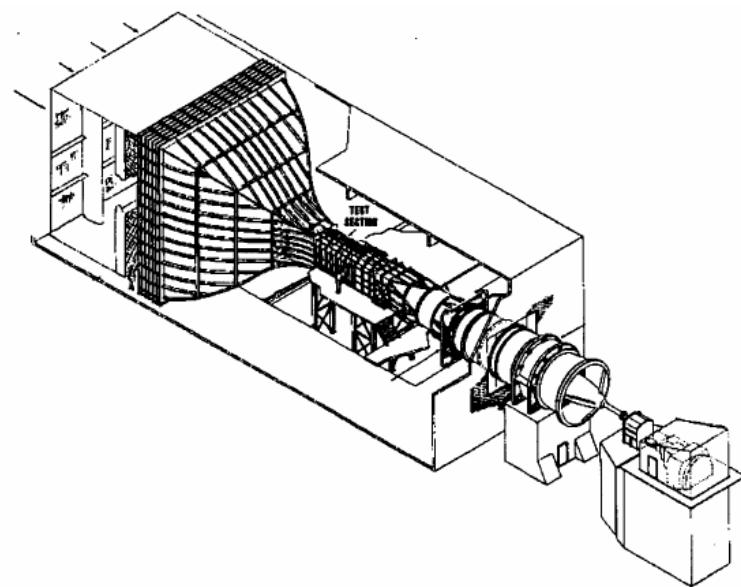
Figure 5.2 Schematic of the Subsonic Aerodynamic Research Laboratory (SARL)..
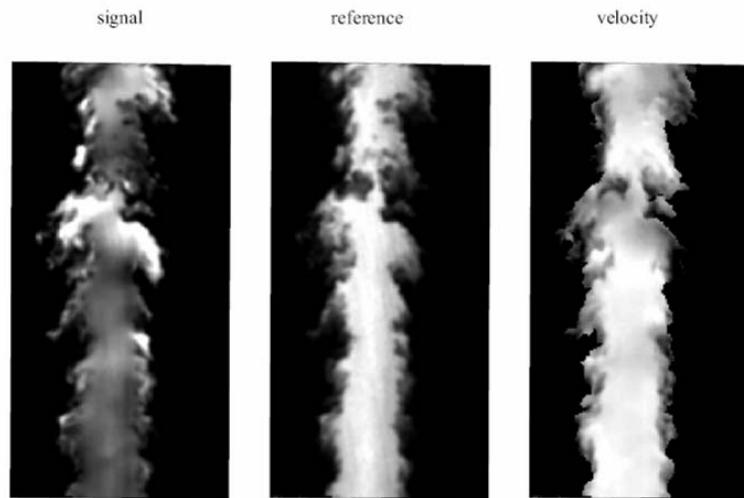
Figure 5.3 Example signal, reference and processed PDV velocity images for the single component measurement system.
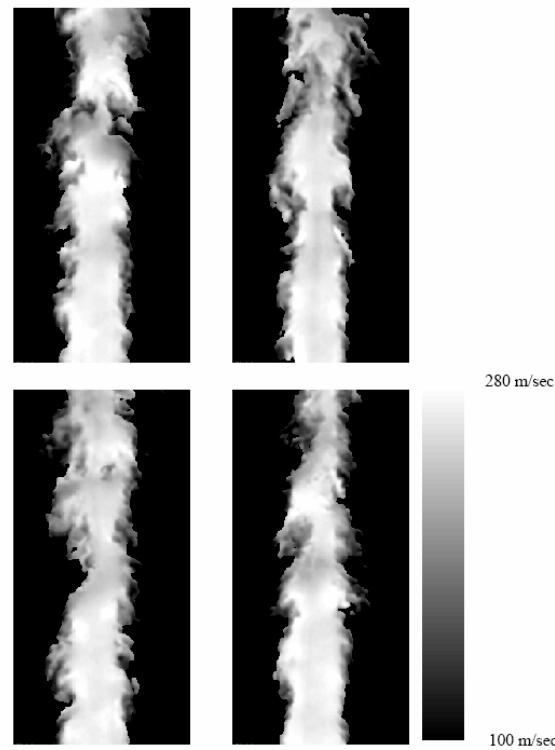
Figure 5.4 Instantaneous velocity measurements in a Mach 1.36 axisymmetric jet measured using PDV. The direction of PDV sensitivity is 0.697i+0.123j-0.707.
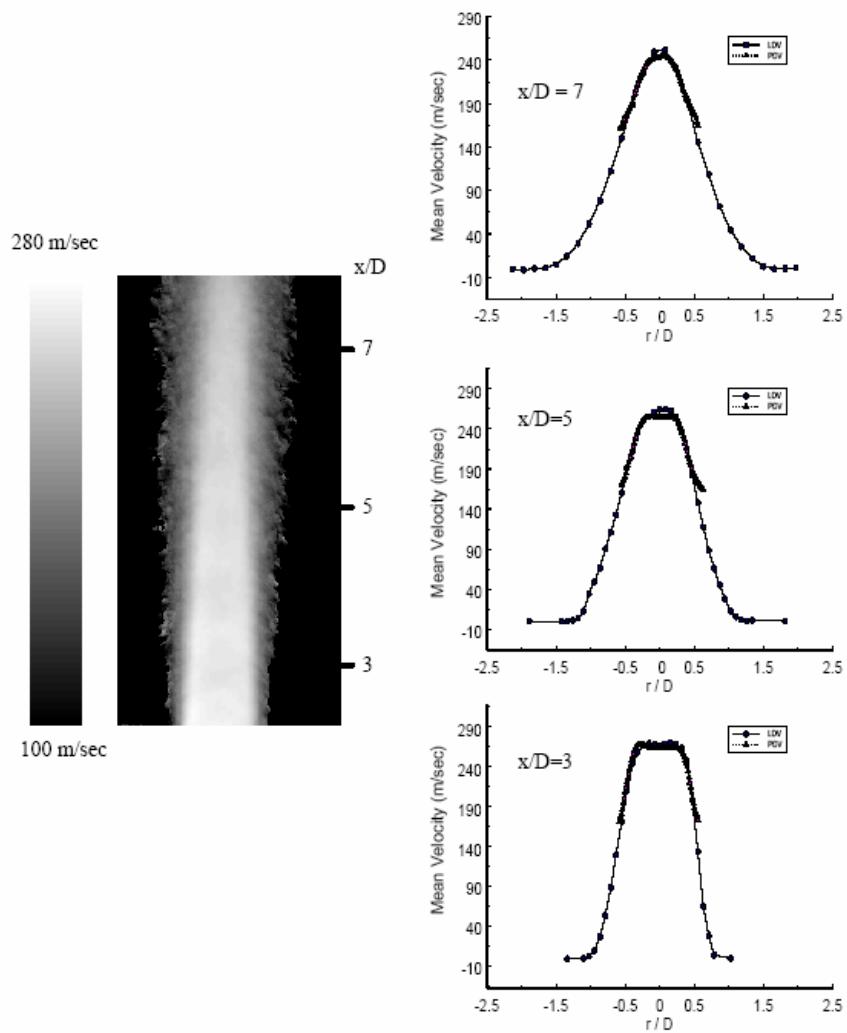
Figure 5.5 Average velocity measured in the Mach 1.36 Jet with PDV and comparison with LDV measurements at three streamwise locations. The direction of PDV sensitivity is 0.697i+0.123j-0.707.
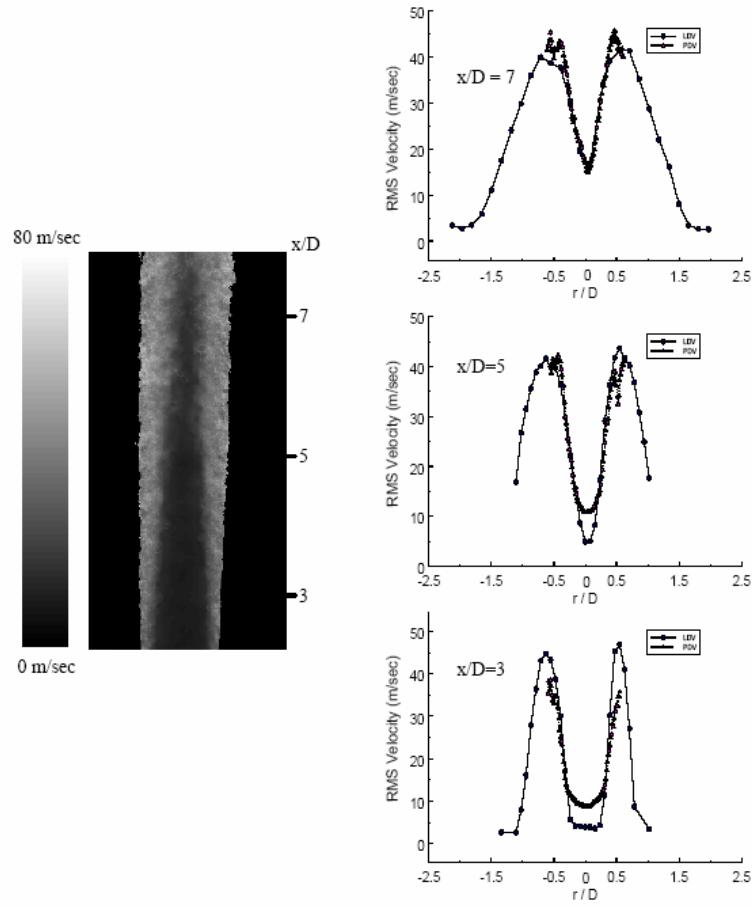
Figure 5.6 RMS velocity fluctuations measured in the Mach 1.36 Jet with PDV and comparison with LDV measurements at three streamwise locations. The direction of PDV sensitivity is 0.697i+0.123j-0.707.
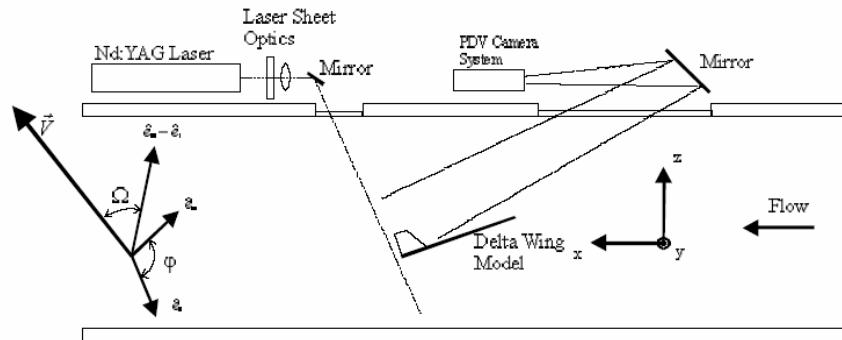
Figure 5.7 Schematic of optical and model orientation for PDV measurements of flow field induced by a delta wing at an angle of attack of 23 degrees.
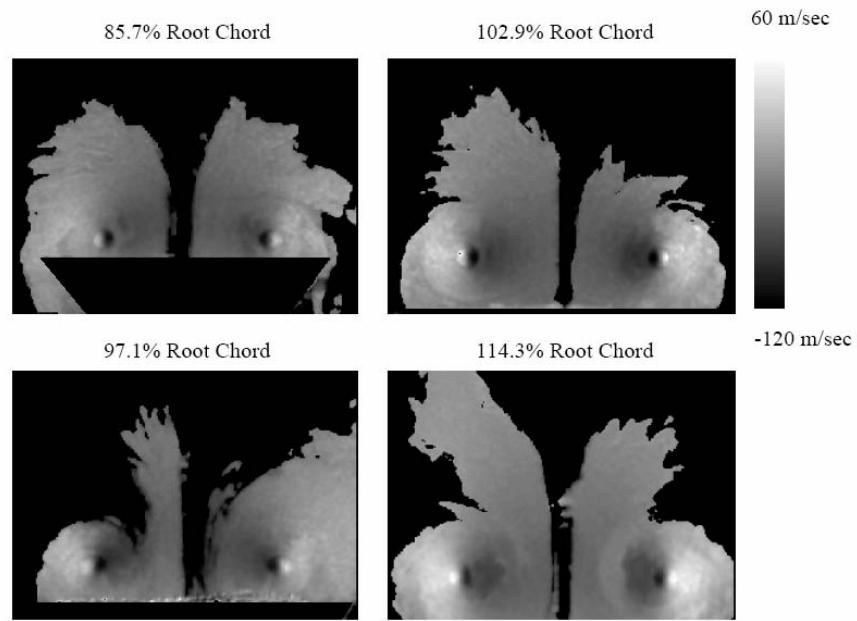
Figure 5.8 Instantaneous PDV measurements above a 70° swept delta wing at a 23° angle of attack at Mach 0.2 and four streamwise locations. Direction of PDV velocity sensitivity is -0.210i - 0.003j + 0.978k.
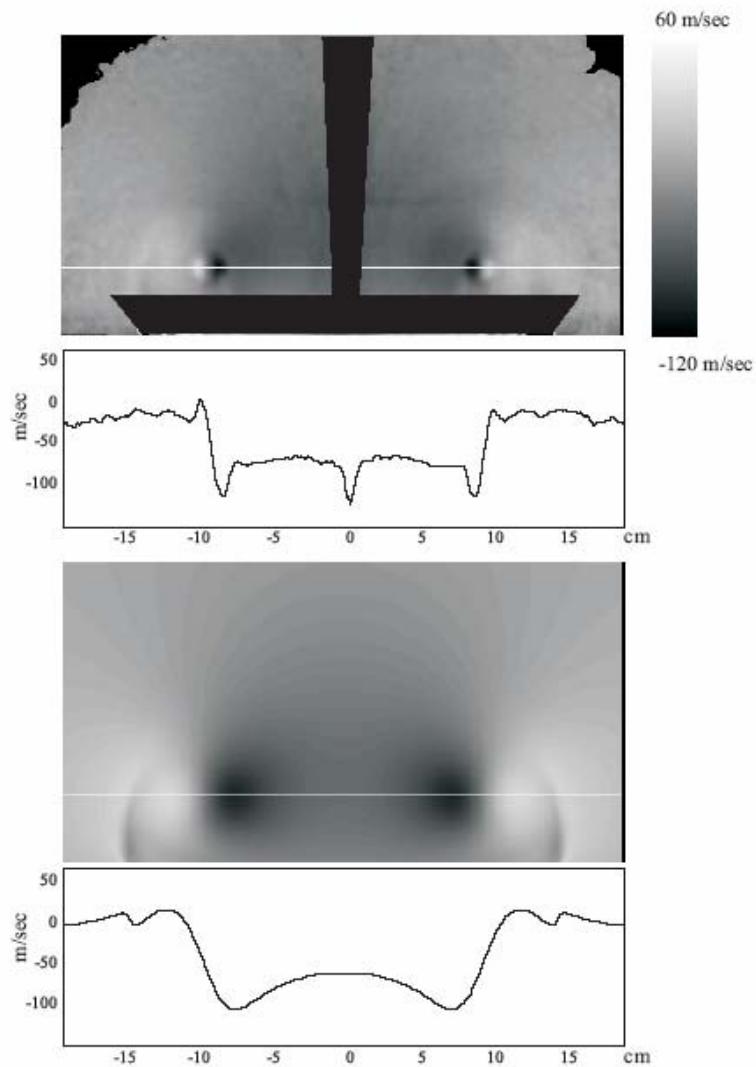
Figure 5.9 Average PDV measurement (top) of delta wing at 86% root chord with comparison to a CFD result (bottom). Direction of PDV velocity sensitivity is -0.210i - 0.003j + 0.978k.
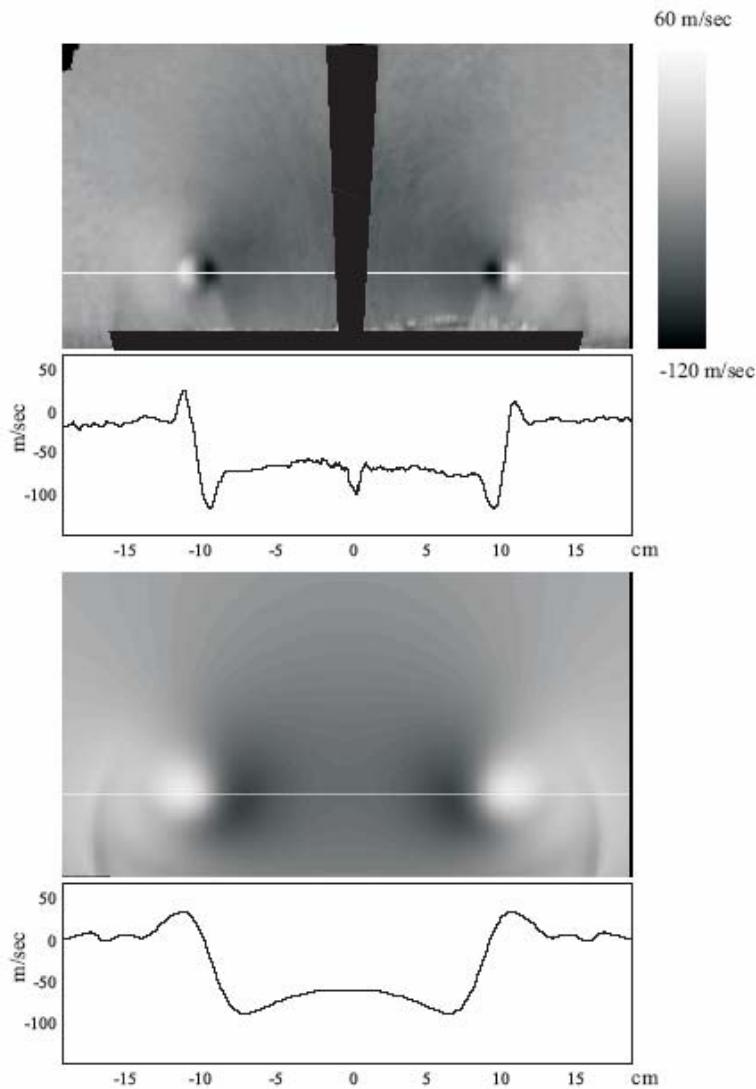
Figure 5.10 Average PDV measurement (top) of delta wing at 97% root chord with comparison to a CFD result (bottom). Direction of PDV velocity sensitivity is -0.210i - 0.003j + 0.978k.
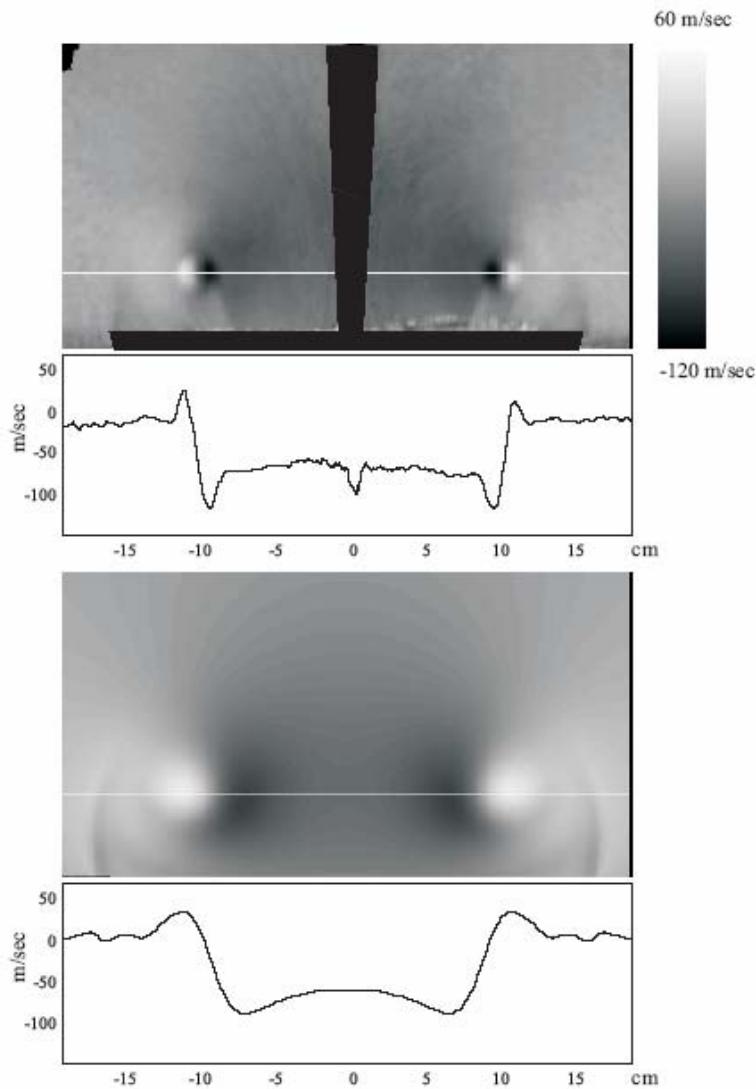
Figure 5.11 Average PDV measurement (top) of delta wing at 103% root chord with comparison to a CFD result (bottom). Direction of PDV velocity sensitivity is -0.210i - 0.003j + 0.978k.
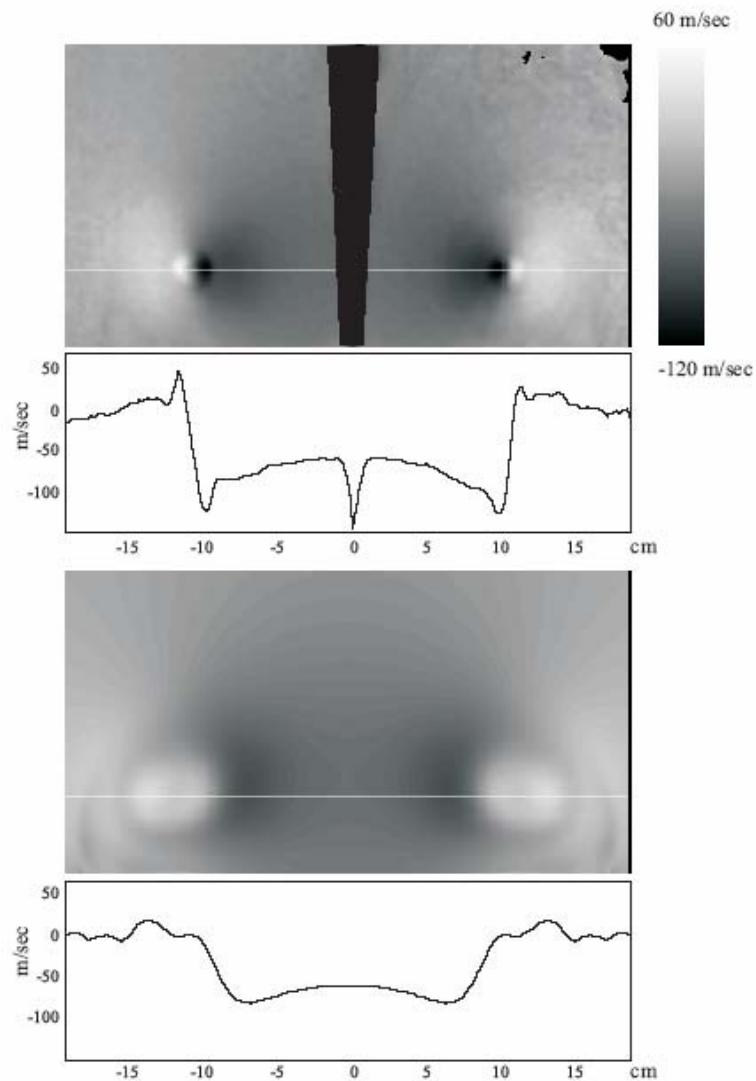
Figure 5.12 Average PDV measurement (top) of delta wing at 114% root chord with comparison to a CFD result (bottom). Direction of PDV velocity sensitivity is -0.210i - 0.003j + 0.978k.
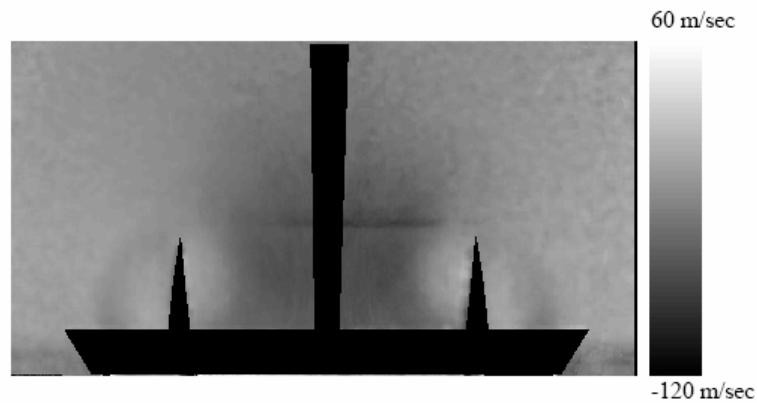
Figure 5.13 Average PDV measurement of delta wing with tails at 86% root chord. Direction of PDV velocity sensitivity is -0.210*i* - 0.003*j* + 0.978*k*.
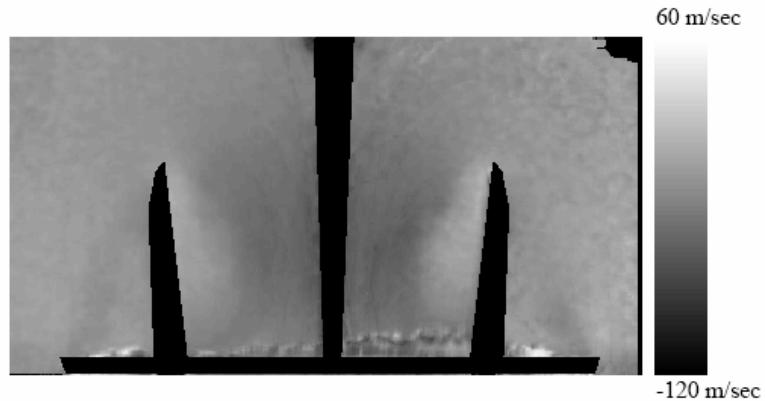
Figure 5.14 Average PDV measurement of delta wing with tails at 97% root chord. Direction of PDV velocity sensitivity is -0.210*i* - 0.003*j* + 0.978*k*.
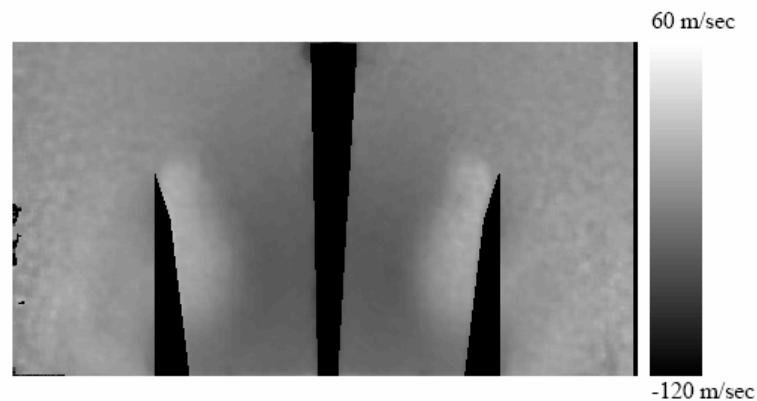
Figure 5.15 Average PDV measurement of delta wing with tails at 103% root chord. Direction of PDV velocity sensitivity is -0.210i - 0.003j + 0.978k.
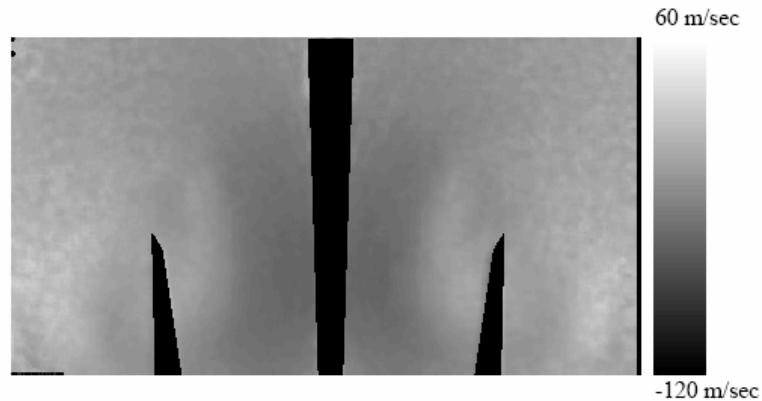
Figure 5.16 Average PDV measurement of delta wing with tails at 114% root chord. Direction of PDV velocity sensitivity is -0.210i - 0.003j + 0.978k.
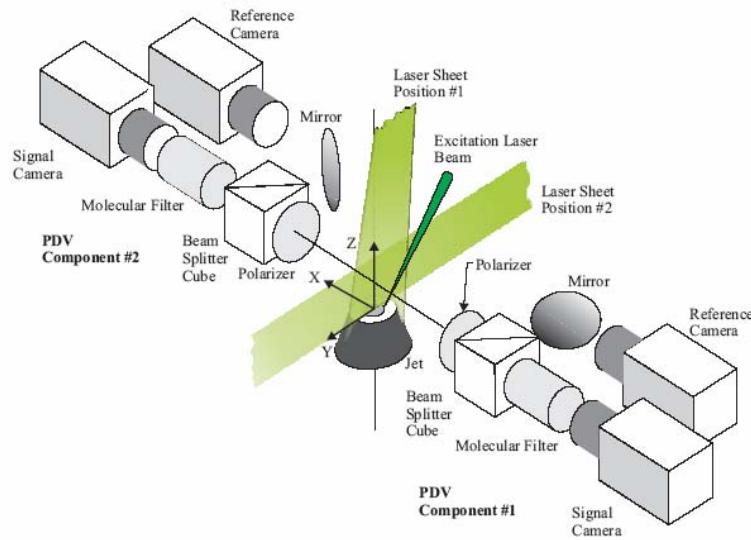
Figure 5.17 PDV camera and laser arrangement for multiple component Mach 1.36 jet measurements.
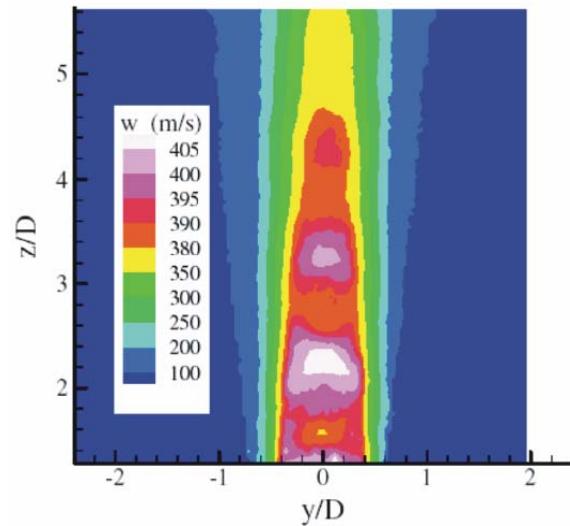
Figure 5.18 Streamwise velocity contours of unexcited Mach 1.34 jet measured using three component PDV.
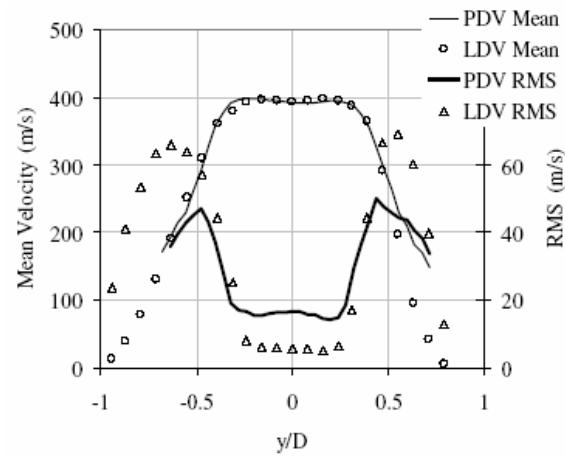
Figure 5.19 Streamwise mean and RMS velocity profiles of the unexcited Mach 1.34 jet measured using PDV and LDV at x/D = 3.0.

170 μsec Time Delay

220 μsec Time Delay
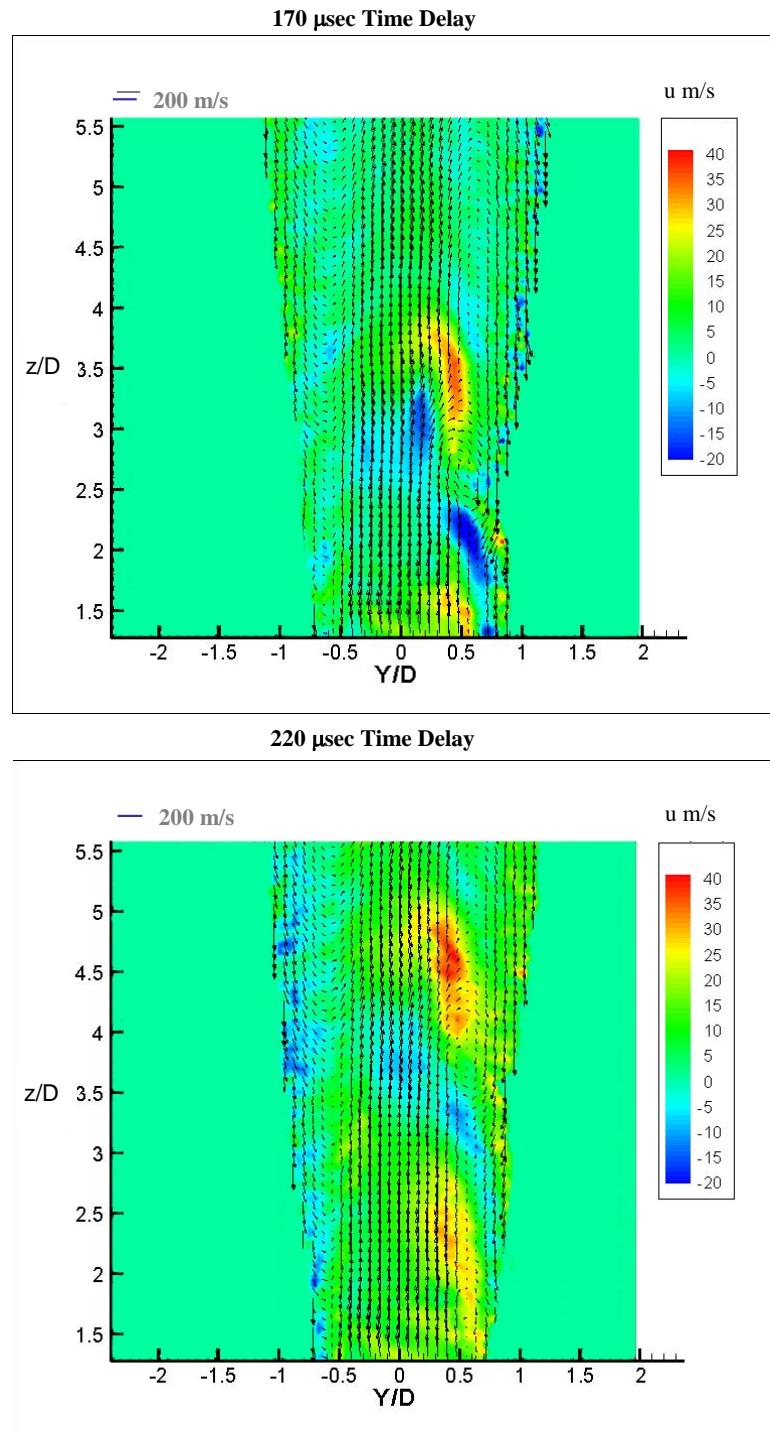
Figure 5.20 Three components of velocity measured using PDV in a Mach 1.34 jet with laser excitation at 170 and 220 μs. The convective velocity (200 m/s) has been subtracted.
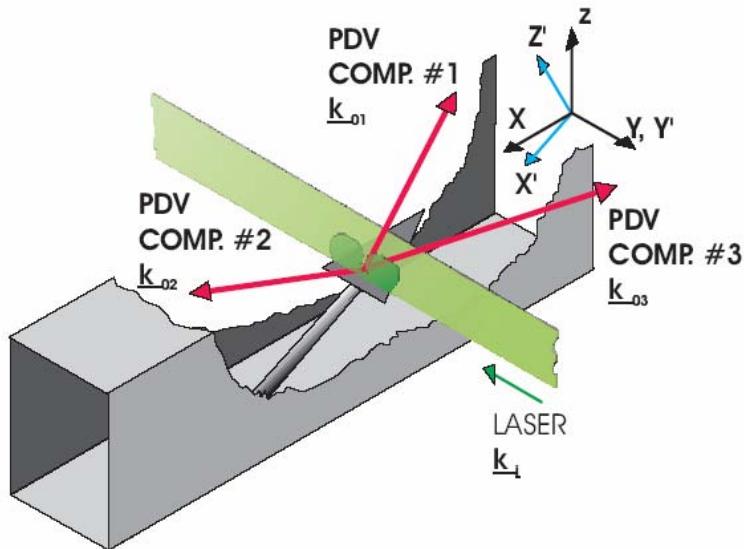
Figure 5.21 Camera and laser coordinate system for three component PDV test in the SARL.
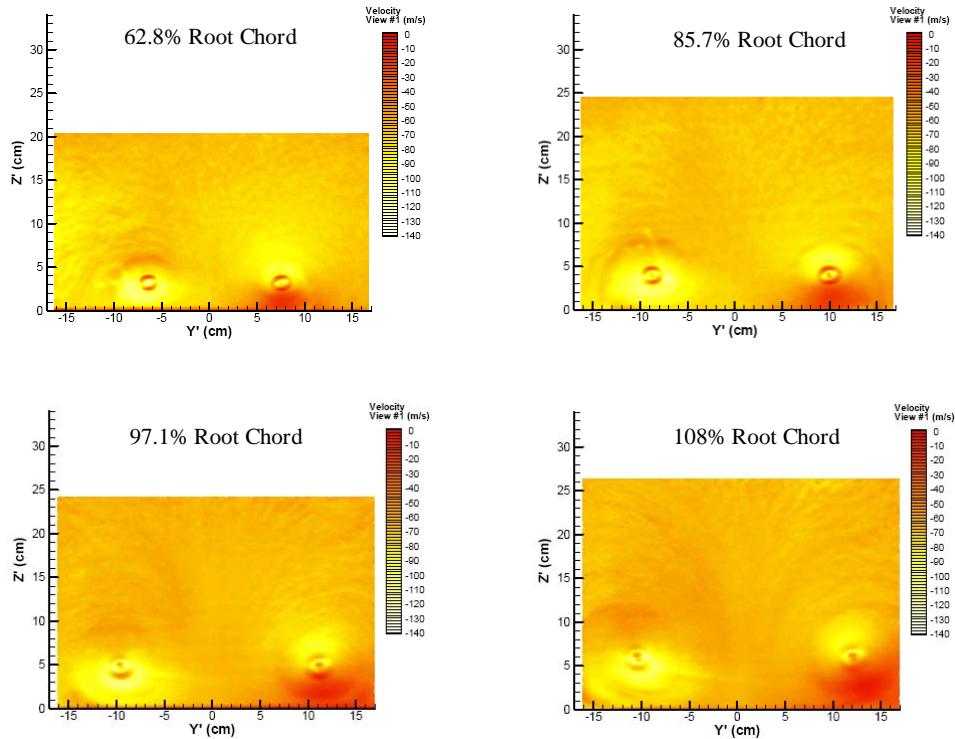
Figure 5.22 Velocity parallel to system sensitivity of PDV component #1 for the flow over a 70°
delta wing at 23° angle of attack in a Mach 0.2 flow. The system sensitivity vector for
the two upstream locations is (-0.811, 0.509, 0.318) and (-0.841, 0.539, 0.290) for the
two downstream locations.
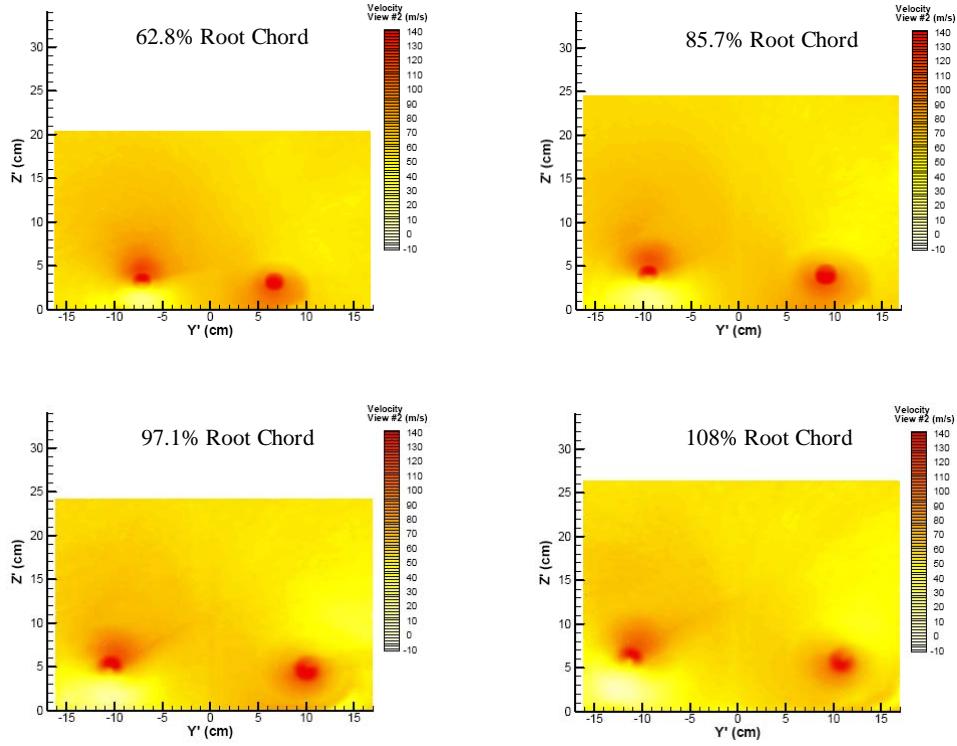
Figure 5.23 Velocity parallel to system sensitivity of PDV component #2 for the flow over a 70°
delta wing at 23° angle of attack in a Mach 0.2 flow. The system sensitivity vector for
the two upstream locations is (0.766, 0.446, -0.325) and (0.726, 0.409, -0.353) for the
two downstream locations.
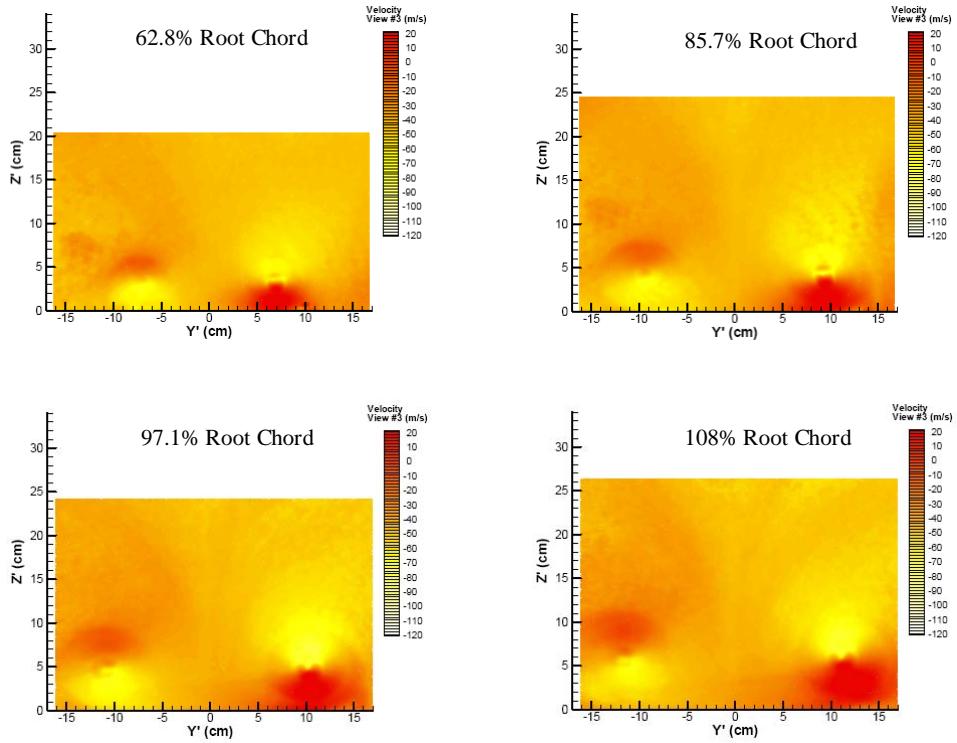
Figure 5.24 Velocity parallel to system sensitivity of PDV component #3 for the flow over a 70°
delta wing at 23° angle of attack in a Mach 0.2 flow. The system sensitivity vector for
the two upstream locations is (-0.817, 1.48, 0.319) and (-0.846, 1.45, 0.294) for the two
downstream locations.
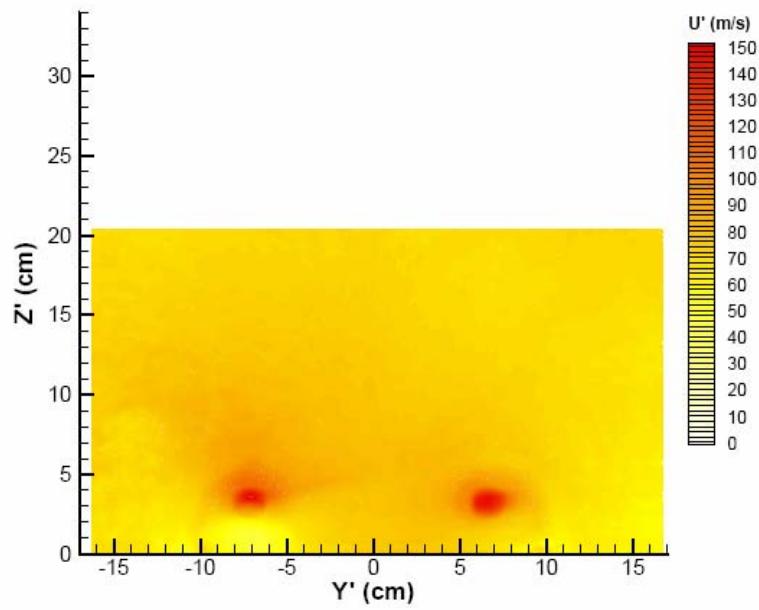
Figure 5.25 Axial velocity (X') velocity component at 62.8% root chord for the flow over a 70°
delta wing at 23° angle of attack in a Mach 0.2 flow.
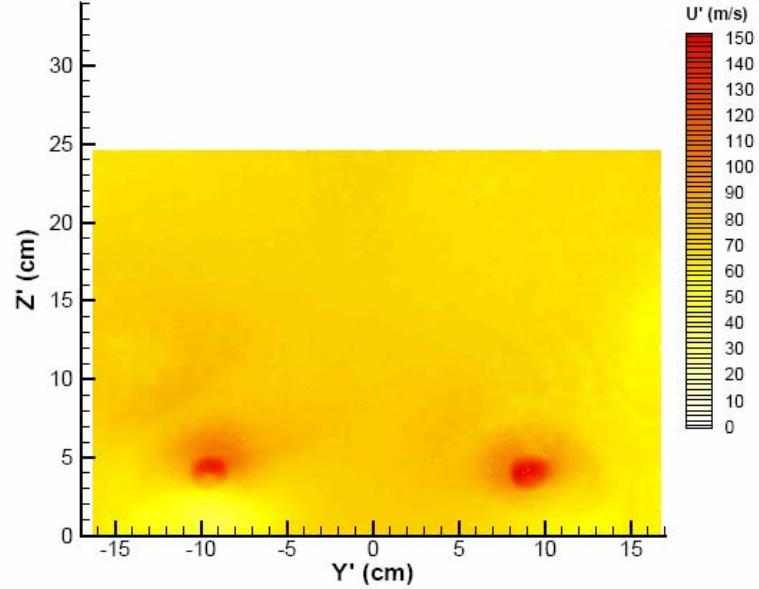
Figure 5.26 Axial velocity (X') velocity component at 85.7% root chord for the flow over a 70°
delta wing at 23° angle of attack in a Mach 0.2 flow.
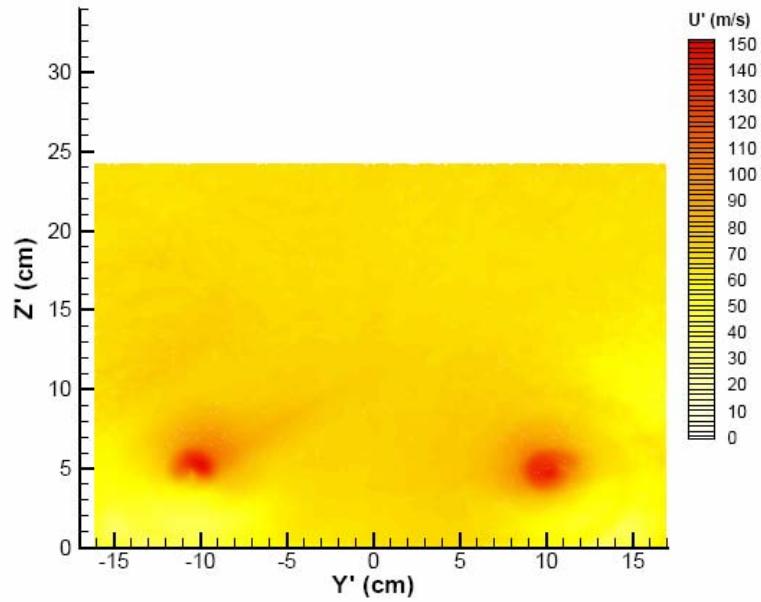
Figure 5.27 Axial velocity (X') velocity component at 97.1% root chord for the flow over a 70°
delta wing at 23° angle of attack in a Mach 0.2 flow.
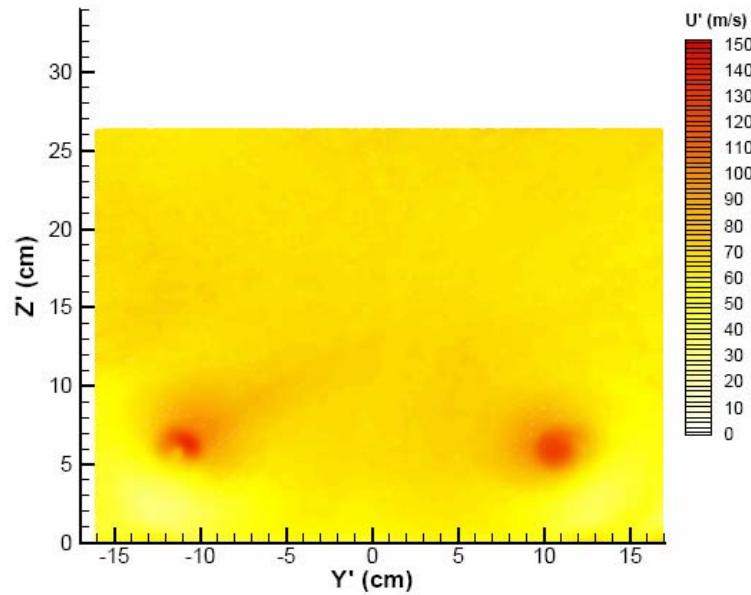
Figure 5.28 Axial velocity (X') velocity component at 1.08 % root chord for the flow over a 70°
delta wing at 23° angle of attack in a Mach 0.2 flow.
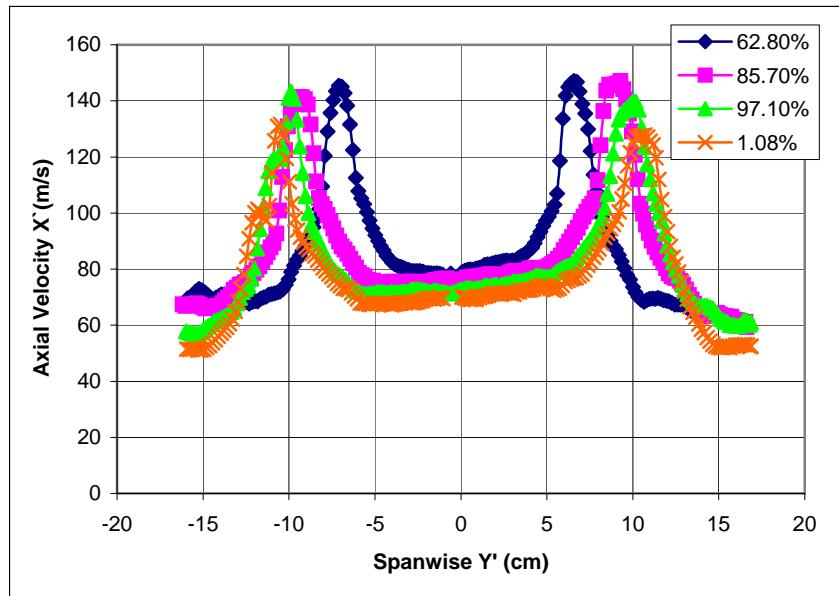
Figure 5.29 Axial velocity (X') velocity profile through peak velocity core of vorices at various streamwise locations given as percentage of root chord for the flow over a 70° delta wing at 23° angle of attack in a Mach 0.2 flow.
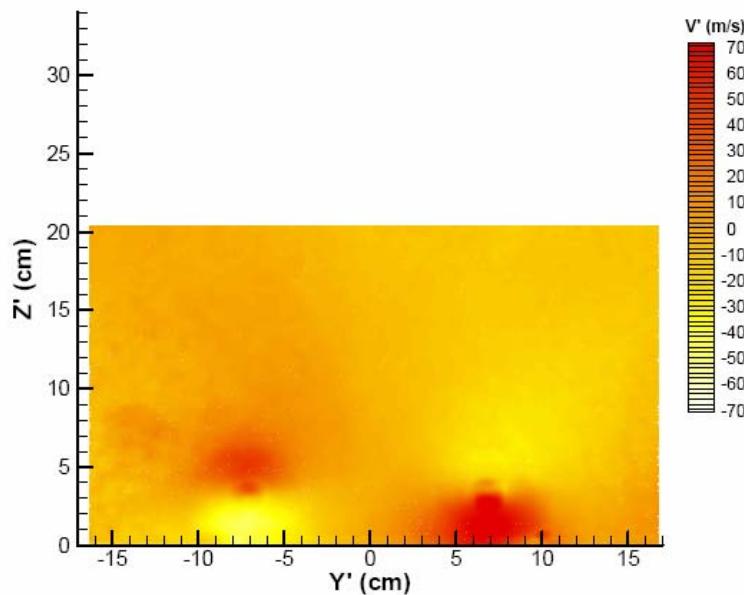
Figure 5.30 Spanwise velocity (Y') velocity component at 62.8% root chord for the flow over a 70° delta wing at 23° angle of attack in a Mach 0.2 flow.
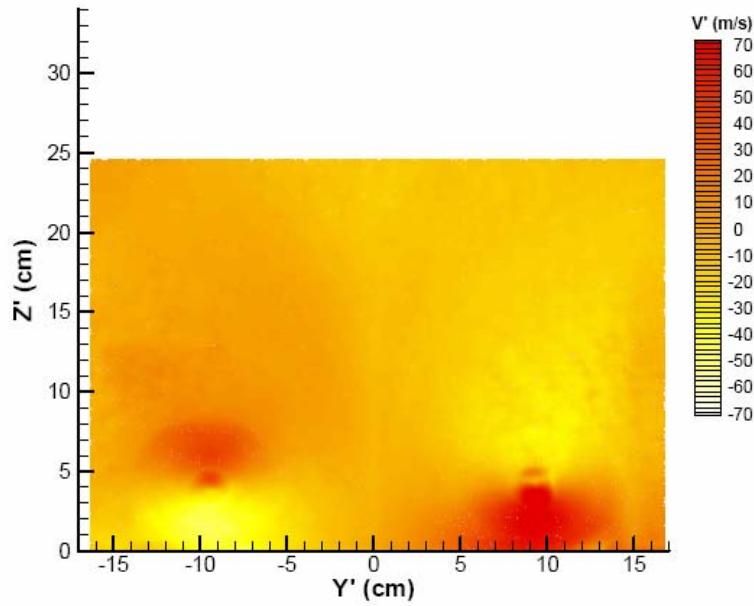
Figure 5.31 Spanwise velocity (Y') velocity component at 85.7% root chord for the flow over a 70° delta wing at 23° angle of attack in a Mach 0.2 flow.
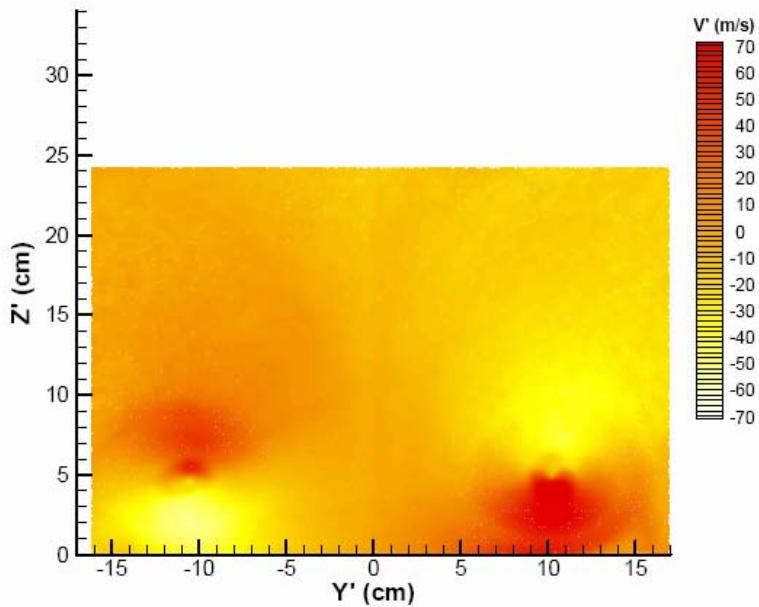
Figure 5.32 Spanwise velocity (Y') velocity component at 97.1% root chord for the flow over a 70° delta wing at 23° angle of attack in a Mach 0.2 flow.
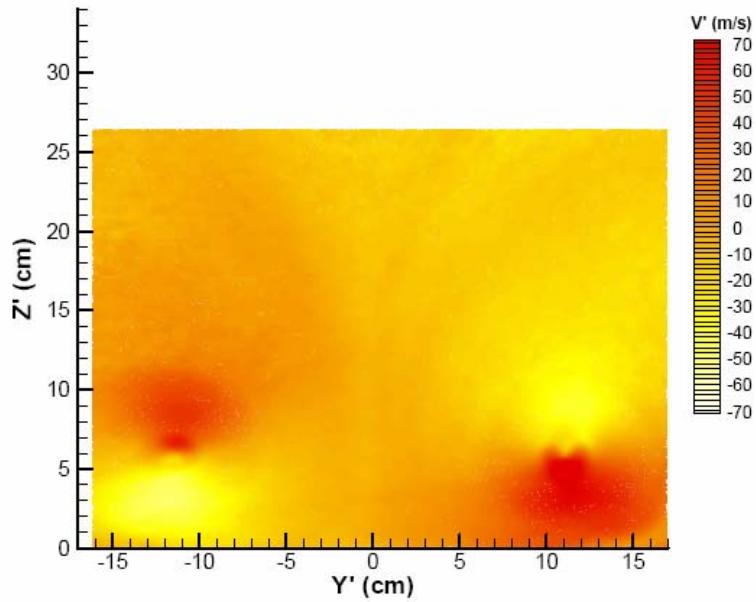
Figure 5.33 Spanwise velocity (Y') velocity component at 1.08% root chord for the flow over a 70° delta wing at 23° angle of attack in a Mach 0.2 flow.
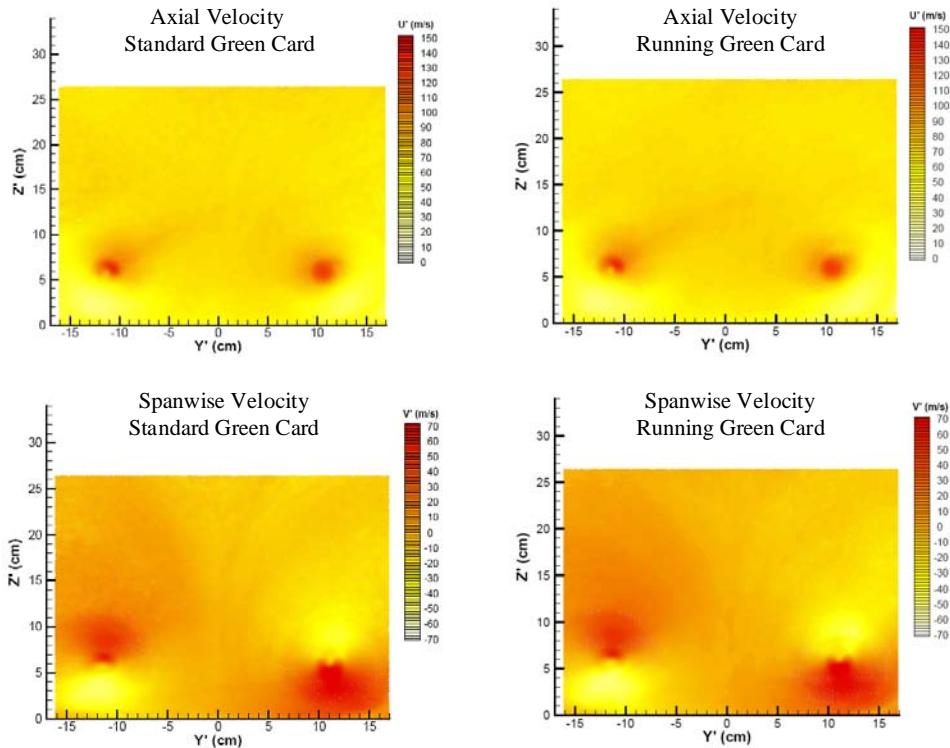
Figure 5.34 Axial and spanwise velocity (Y') velocity components at 1.08% root chord for the flow over a 70° delta wing at 23° angle of attack in a Mach 0.2 flow measured using standard green card and empty tunnel running green card images for calibration.
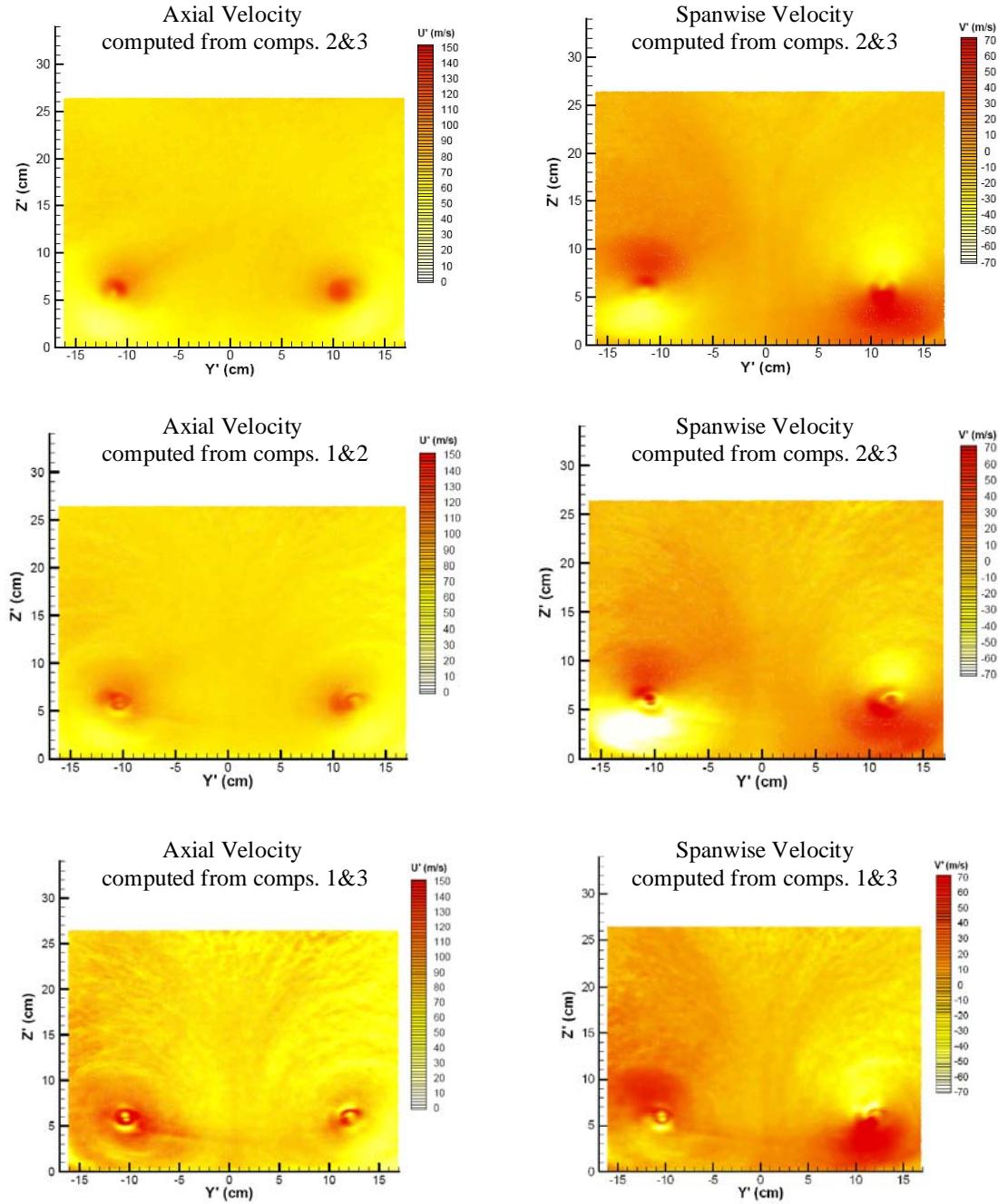
Figure 5.35 Axial and spanwise velocity components at 1.08% root chord for the flow over a
70° delta wing at 23° angle of attack in a Mach 0.2 flow derived from PDV components
of 2&3, 1&2, and 1&3.
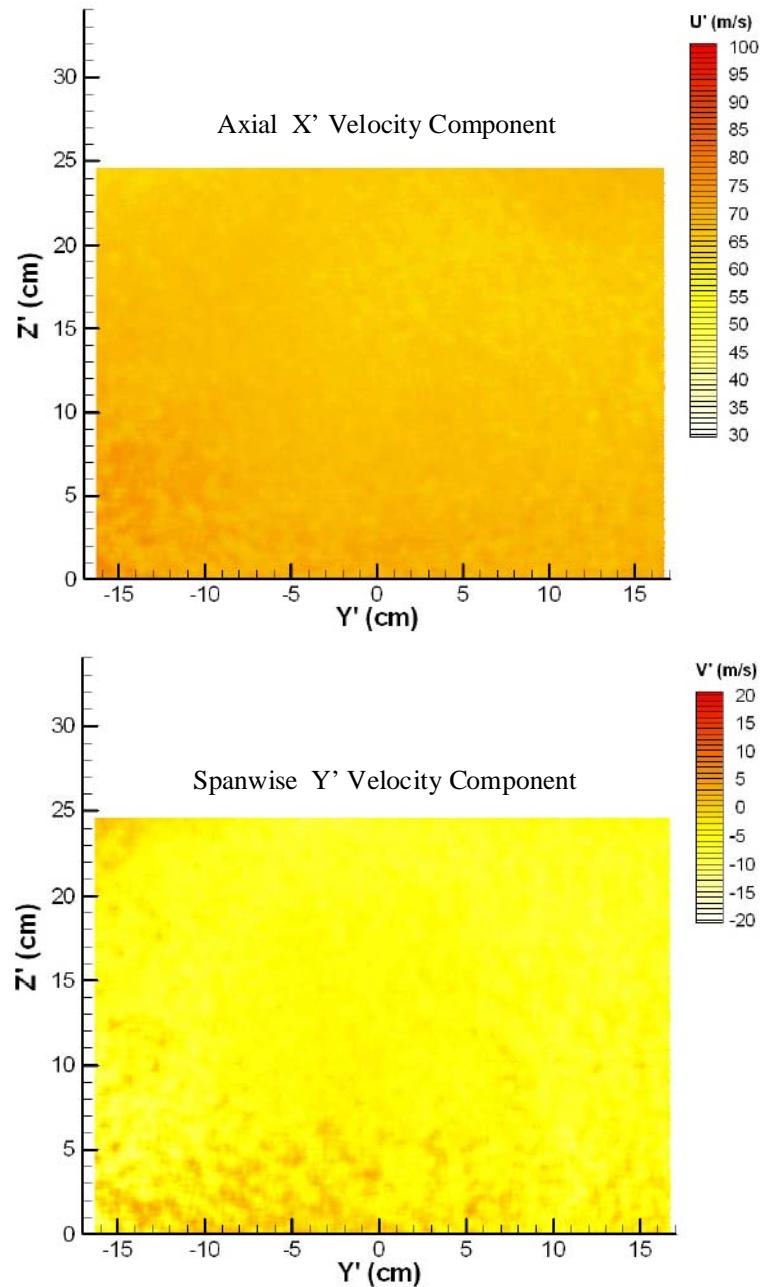
Figure 5.36 Axial and spanwise velocity components for the empty wind tunnel tests at Mach 0.2 measured using PDV.
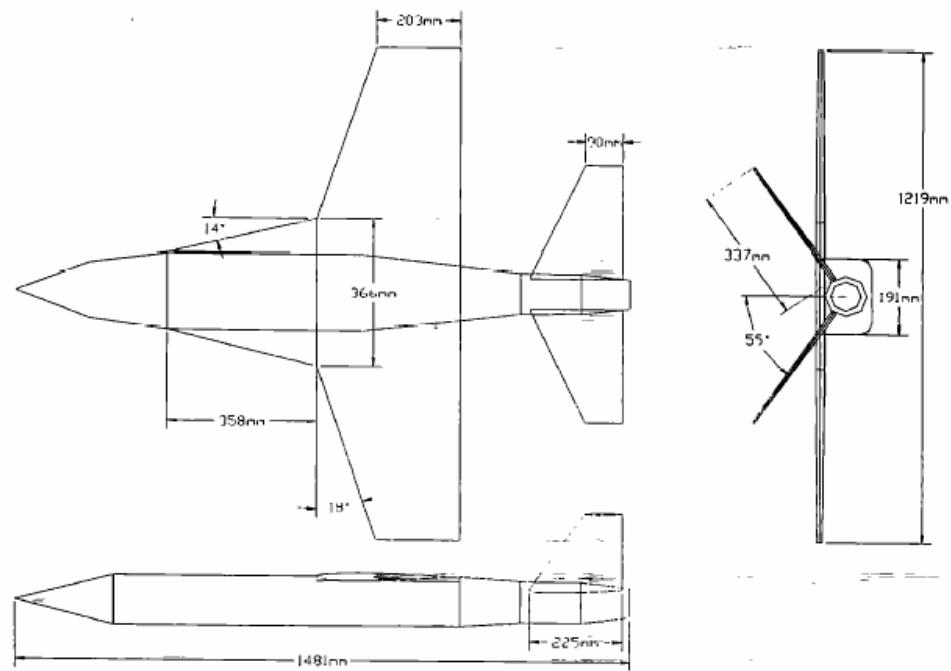
Figure 5.37 A Schematic of Boeing interference model.
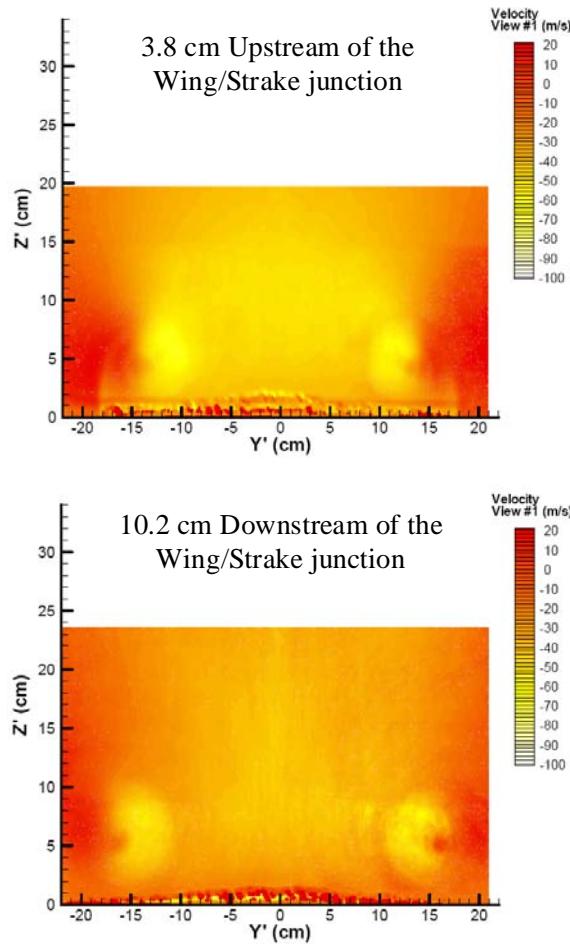
Figure 5.38 PDV measurement of Boeing interference model at an angle of attack of 20 degrees measured 3.8 cm and 10.2 cm upstream and downstream of wing strake junction. The system sensitivity unit vector for this top view is (-0.273i, 0.0j, 0.962k).
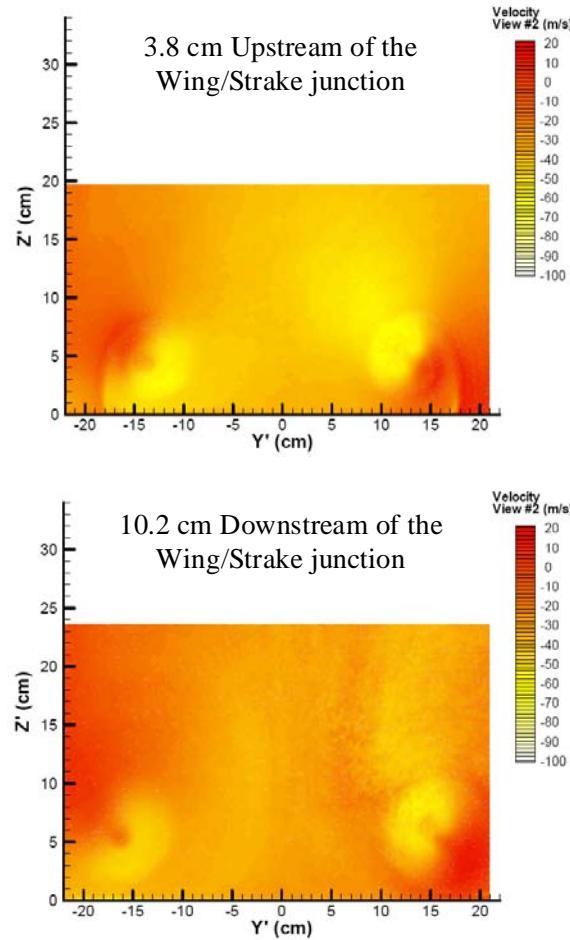
Figure 5.39 PDV measurement of Boeing interference model at an angle of attack of 20 degrees measured 3.8 cm and 10.2 cm upstream and downstream of wing strake junction. The system sensitivity unit vector for this side view is (-0.304i, 0.406j, 0.848k).
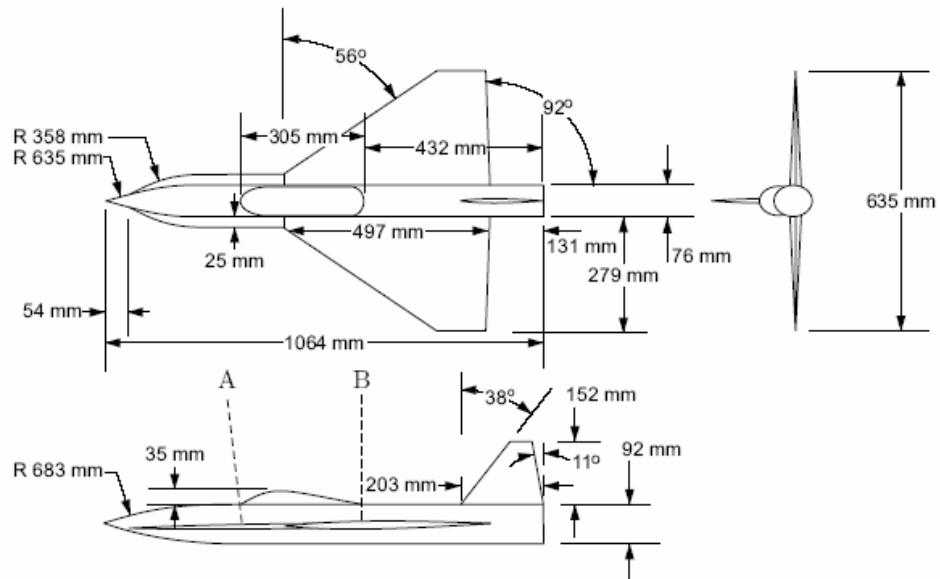
Figure 5.40 56 degree delta wing generic fighter model. PDV laser sheet locations are shown 108 mm.

a. Velocity field on plane labeled A obtained with the top-mounted detector

b. Velocity field on plane A with side-mounted detector
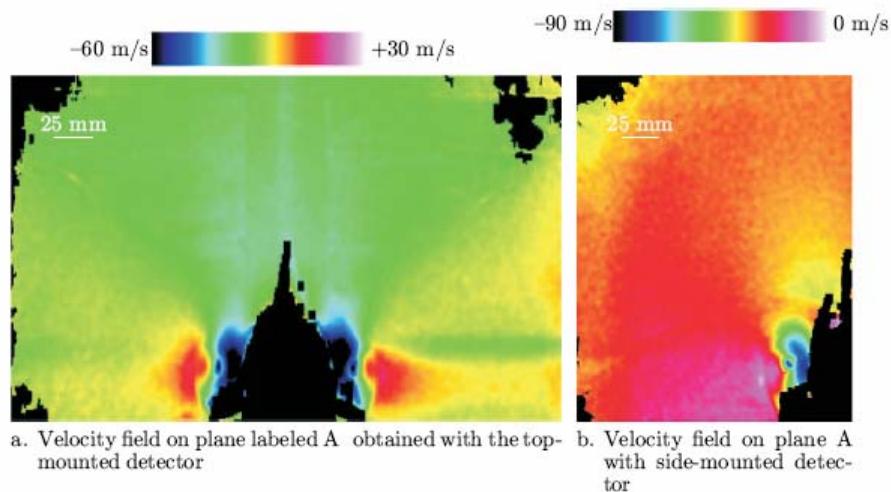
Figure 5.41 PDV velocity field of 56° delta wing model at 23° angle of attack in a Mach 0.2 free stream measured at plane A (108 mm upstream of wing strake junction) with top-mounted (-0.253i, 0.0 j, 0.968k) and side-mounted (-0.296i,0.421j,0.857k) cameras.
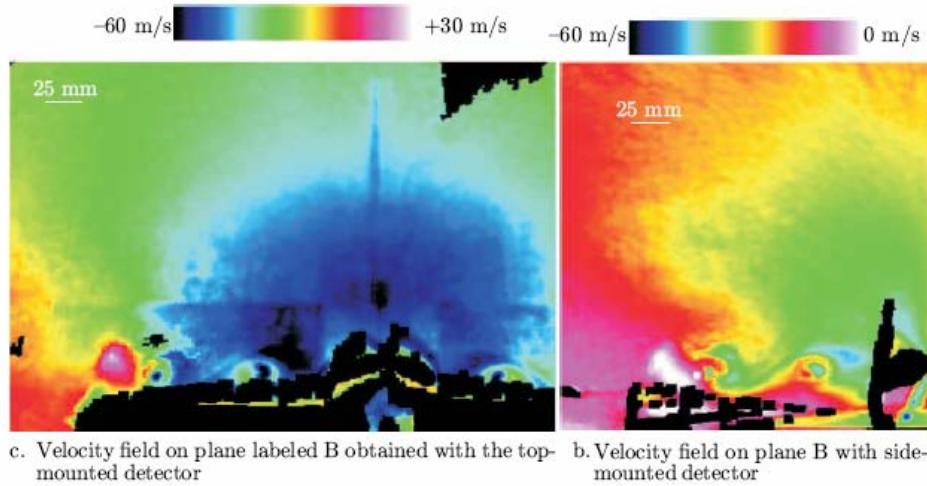
c. Velocity field on plane labeled B obtained with the top-mounted detector

b. Velocity field on plane B with side-mounted detector

Figure 5.42 PDV velocity field of 56° delta wing model at 23° angle of attack in a Mach 0.2 free stream measured at plane B (trailing edge of canopy) with top- mounted (-0.253i, 0.0 j, 0.968k) and side-mounted (-0.296i,0.421j,0.857k) cameras.
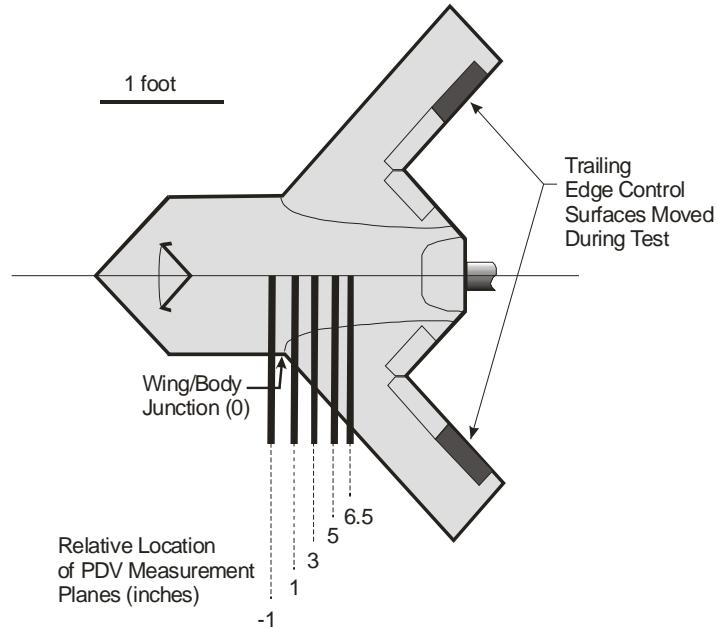
Figure 5.43 Schematic of Boeing UCAV model used in 3-D PDV tests.
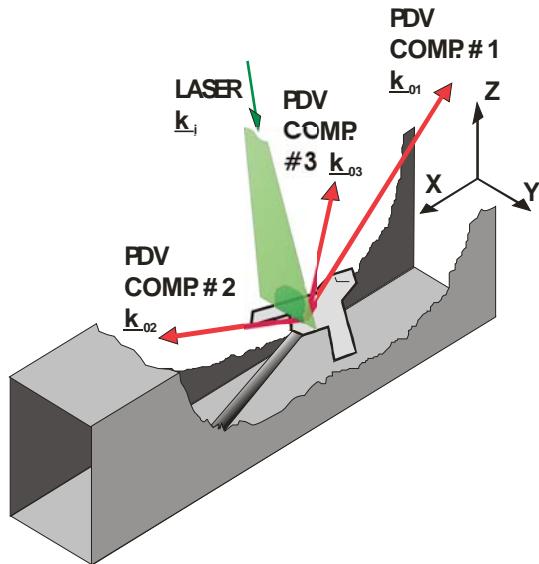
Figure 5.44 Camera and laser coordinate system for three component PDV Boeing UCAV test in the SARL.
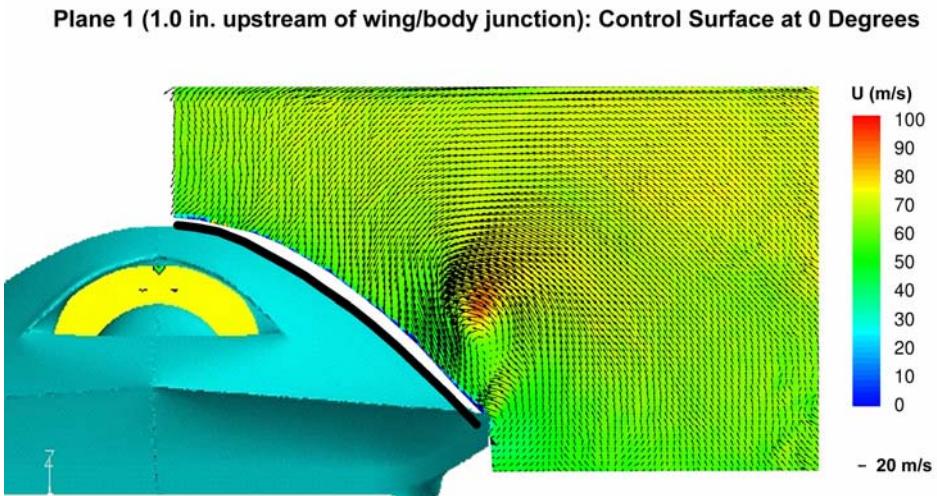
Figure 5.45 Three component velocity field measured using PDV of the Boeing UCAV model. The semi-span measurement plane is located at 1.0 inches upstream of the wing/body junction. The control surface deflection is 0 degrees (a positive angle is up).

Plane 3 (3.0 in. downstream of wing/body junction): Control Surface at 0 Degrees
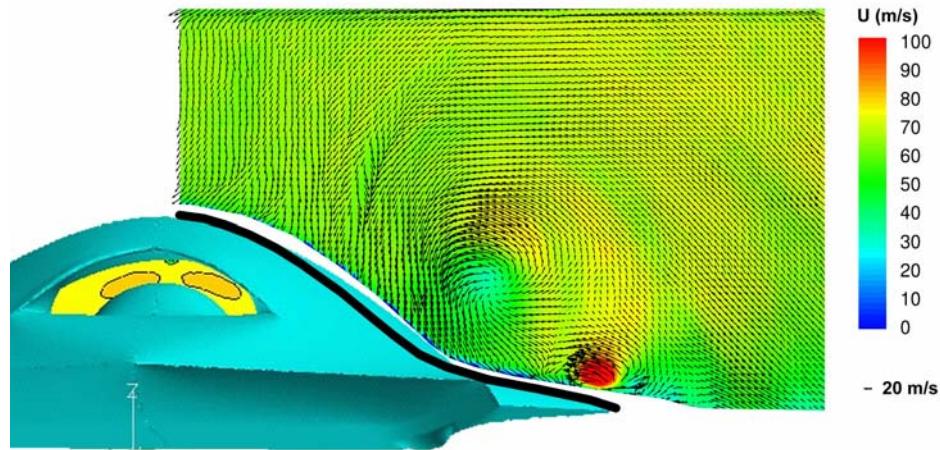
Figure 5.46 Three component velocity field measured using PDV of the Boeing UCAV model. The semi-span measurement plane is located at 3.0 inches downstream of the wing/body junction. The control surface deflection is 0 degrees (a positive angle is up).

Plane 4 (5.0 in. downstream of wing/body junction): Control Surface at 0 Degrees
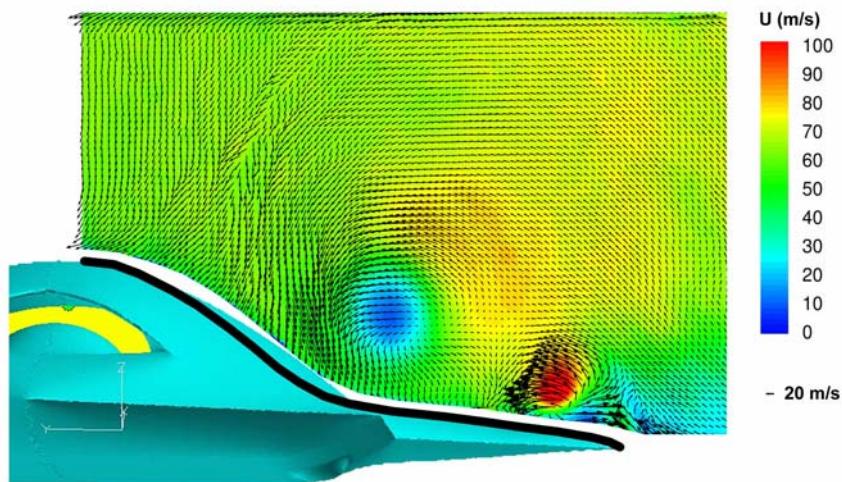
Figure 5.47 Three component velocity field measured using PDV of the Boeing UCAV model. The semi-span measurement plane is located at 5.0 inches downstream of the wing/body junction. The control surface deflection is 0 degrees (a positive angle is up).

Plane 5 (6.5 in. downstream of wing/body junction): Control Surface at 0 Degrees
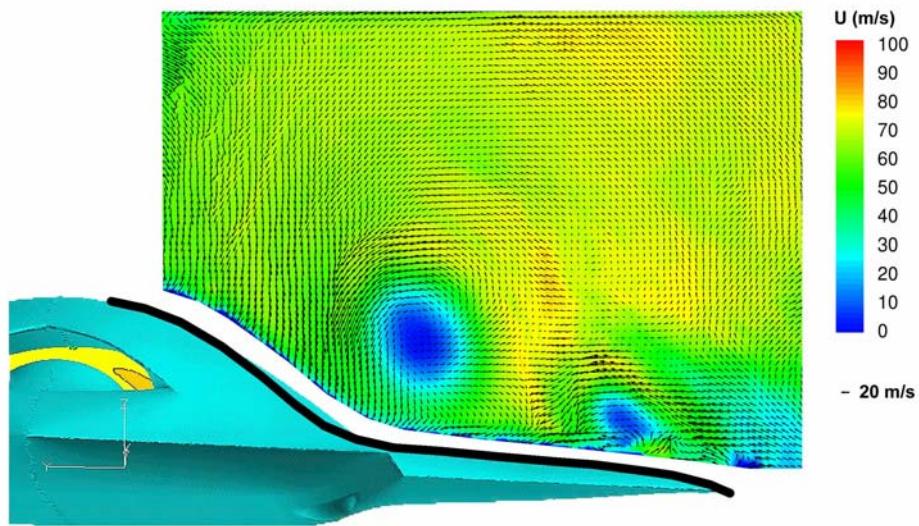
Figure 5.48 Three component velocity field measured using PDV of the Boeing UCAV model. The semi-span measurement plane is located at 6.5 inches downstream of the wing/body junction. The control surface deflection is 0 degrees (a positive angle is up).

Plane 1 (1.0 in. upstream of wing/body junction): Control Surface at -20 Degrees
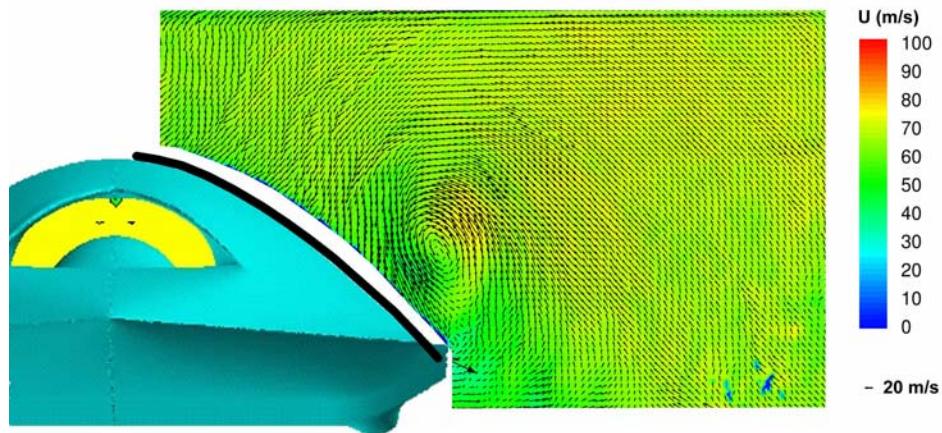
Figure 5.49 Three component velocity field measured using PDV of the Boeing UCAV model. The semi-span measurement plane is located at 1.0 inches upstream of the wing/body junction. The control surface deflection is -20 degrees (a positive angle is up).

Plane 2 (1.0 in. downstream of wing/body junction): Control Surface at -20 Degrees
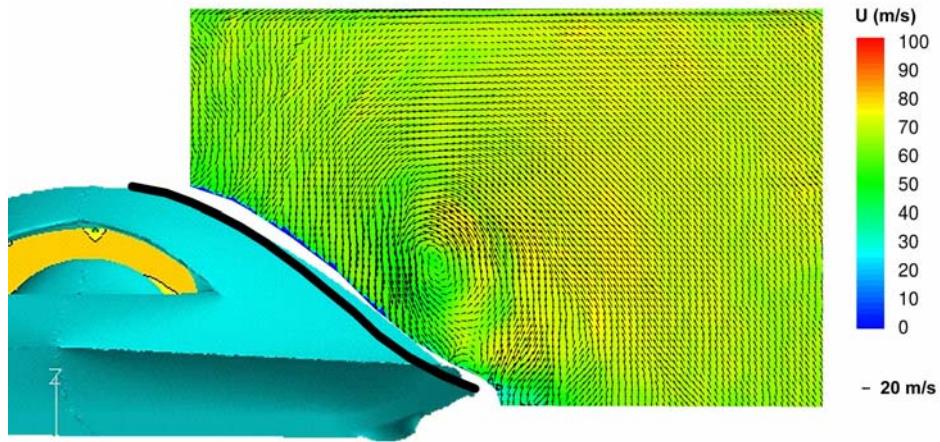
Figure 5.50 Three component velocity field measured using PDV of the Boeing UCAV model. The semi-span measurement plane is located at 1.0 inches downstream of the wing/body junction. The control surface deflection is -20 degrees (a positive angle is up).

Plane 4 (5.0 in. downstream of wing/body junction): Control Surface at -20 Degrees
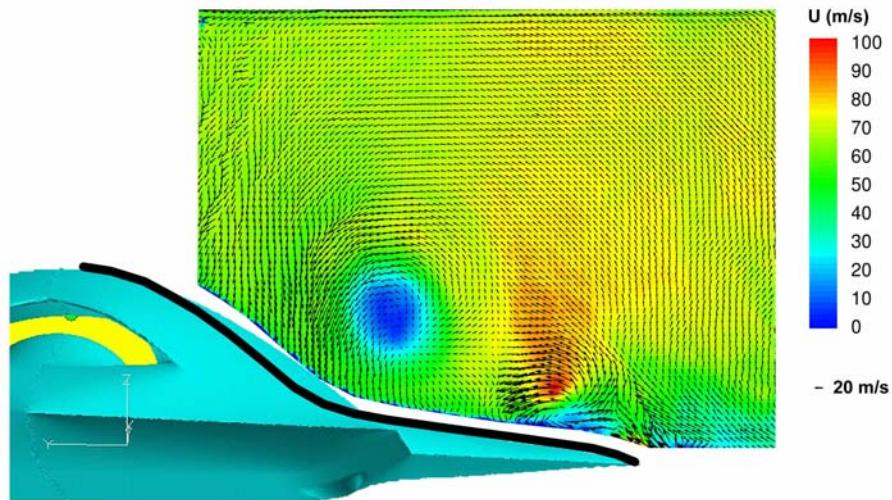
Figure 5.51 Three component velocity field measured using PDV of the Boeing UCAV model. The semi-span measurement plane is located at 5.0 inches downstream of the wing/body junction. The control surface deflection is -20 degrees (a positive angle is up).

Plane 5 (6.5 in. downstream of wing/body junction): Control Surface at -20 Degrees
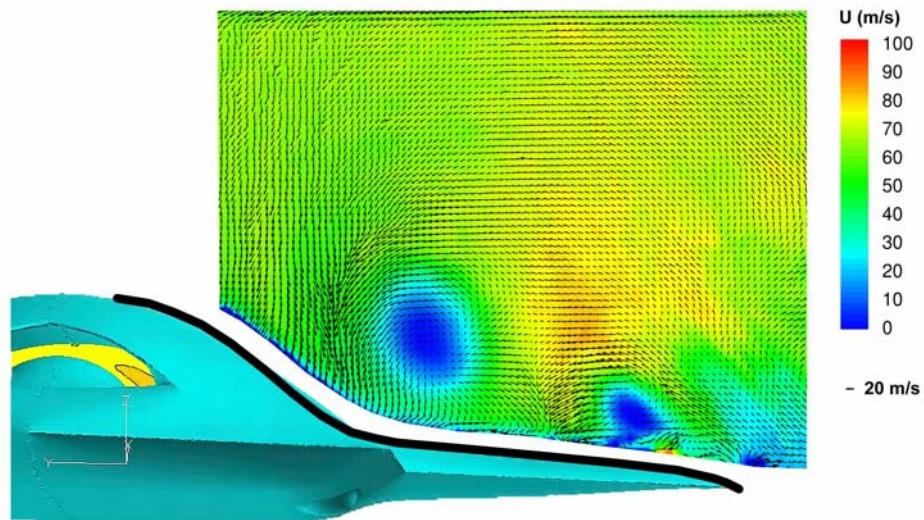
Figure 5.52 Three component velocity field measured using PDV of the Boeing UCAV model. The semi-span measurement plane is located at 6.5 inches downstream of the wing/body junction. The control surface deflection is -20 degrees (a positive angle is up).

Plane 1 (1.0 in. upstream of wing/body junction): Control Surface at 20 Degrees
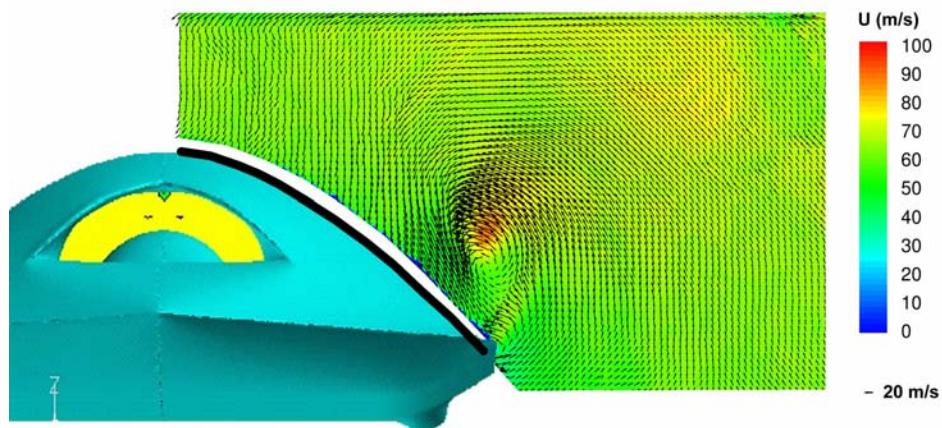
Figure 5.53 Three component velocity field measured using PDV of the Boeing UCAV model. The semi-span measurement plane is located at 1.0 inches upstream of the wing/body junction. The control surface deflection is 20 degrees (a positive angle is up).

Plane 3 (3.0 in. downstream of wing/body junction): Control Surface at 20 Degrees
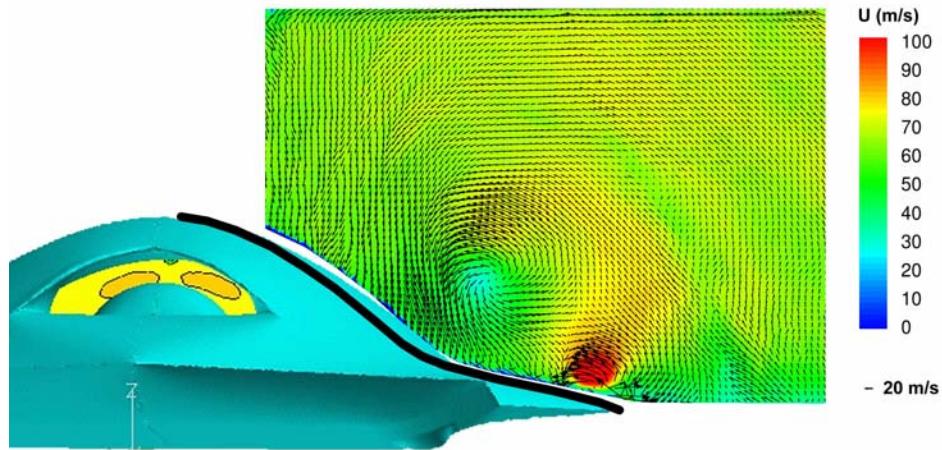
Figure 5.54 Three component velocity field measured using PDV of the Boeing UCAV model. The semi-span measurement plane is located at 3.0 inches downstream of the wing/body junction. The control surface deflection is 20 degrees (a positive angle is up).

Plane 4 (5.0 in. downstream of wing/body junction): Control Surface at 20 Degrees
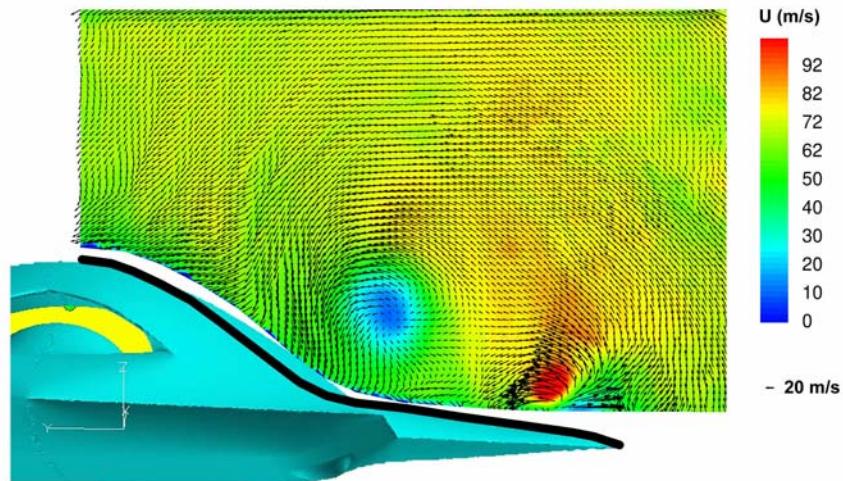
Figure 5.55 Three component velocity field measured using PDV of the Boeing UCAV model. The semi-span measurement plane is located at 5.0 inches downstream of the wing/body junction. The control surface deflection is 20 degrees (a positive angle is up).
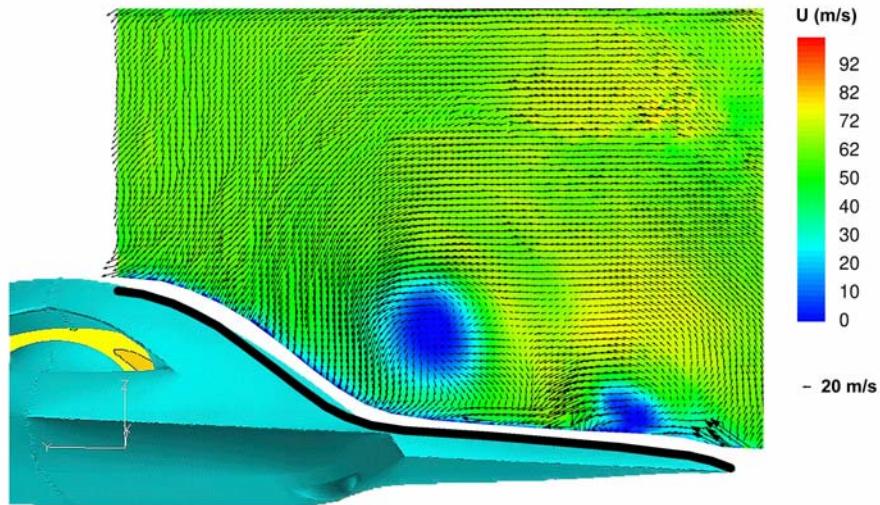
Figure 5.56 Three component velocity field measured using PDV of the Boeing UCAV model. The semi-span measurement plane is located at 6.5 inches downstream of the wing/body junction. The control surface deflection is 20 degrees (a positive angle is up).

Plane 1 (1.0 in. upstream of wing/body junction)
Control Surface: Left - 20 Degrees, Right 20 Degrees
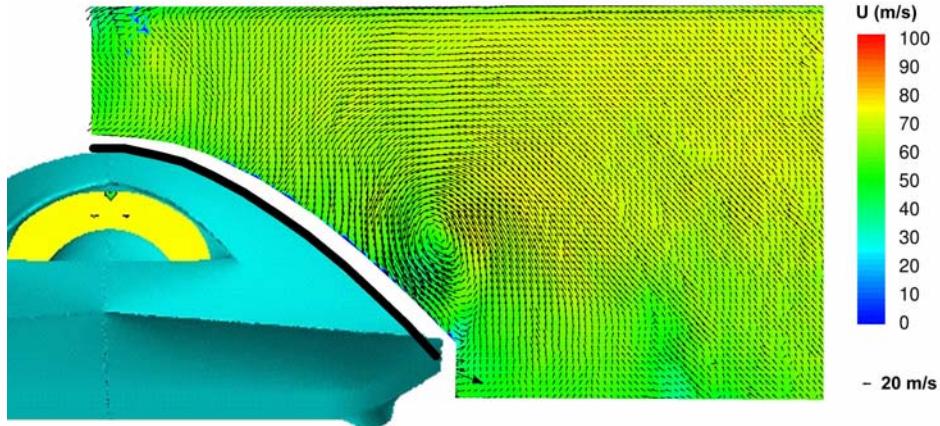
Figure 5.57 Three component velocity field measured using PDV of the Boeing UCAV model. The semi-span measurement plane is located at 1.0 inches upstream of the wing/body junction. The control surface deflection is -20 degrees on this side of the aircraft and +20 degrees on the opposite side (a positive angle is up).
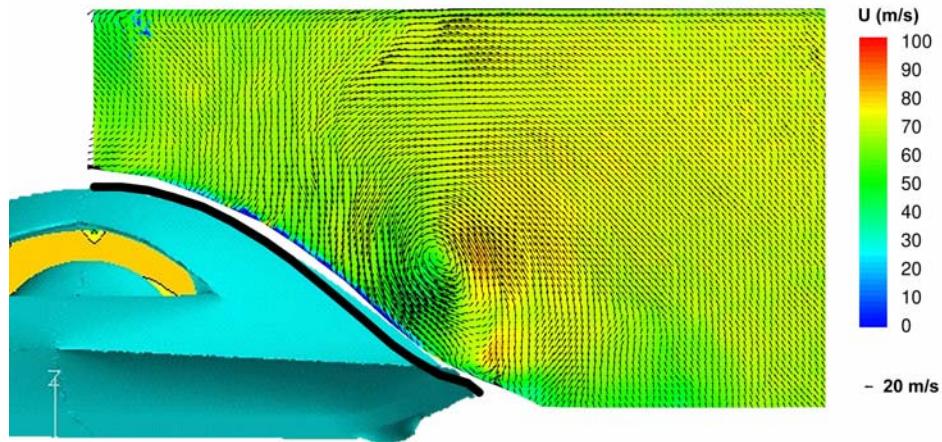
Figure 5.58 Three component velocity field measured using PDV of the Boeing UCAV model. The semi-span measurement plane is located at 1.0 inches downstream of the wing/body junction. The control surface deflection is -20 degrees on this side of the aircraft and +20 degrees on the opposite side (a positive angle is up).

Figure 5.59 Three component velocity field measured using PDV of the Boeing UCAV model. The semi-span measurement plane is located at 3.0 inches downstream of the wing/body junction. The control surface deflection is -20 degrees on this side of the aircraft and +20 degrees on the opposite side (a positive angle is up).

130

Figure 5.60 Three component velocity field measured using PDV of the Boeing UCAV model. The semi-span measurement plane is located at 5.0 inches downstream of the wing/body junction. The control surface deflection is -20 degrees on this side of the aircraft and +20 degrees on the opposite side (a positive angle is up).

PDV Characteristic	Jet Facility	Wind Tunnel Facility
Laser Tuning Coefficient	1.70 GHz/V	-3.00 GHz/V
ϕ	90°	110.8°
Ω	45.8°	102.1°
$\cos(\Omega)$	0.6972	-0.2096
$(\partial V/\partial\phi)/V$	-0.9% per degree	-0.6% per degree
$(\partial V/\partial\Omega)/V$	1.79% per degree	-8.16% per degree
Sensitivity, $2\sin(\phi)/\lambda$	2.66 MHz/(m/sec)	3.10 MHz/(m/sec)
Sensitivity^{-1}, $\lambda/2\sin(\phi)$	0.376 (m/sec)/MHz	0.323 (m/sec)/MHz
pixels/cm	59.8	10.2
magnification	0.148	0.0264
$d\zeta_c / dS_{c12}$ (linear region)	-6.1 MHz/(% trans)	4.4 MHz/(% trans)
$d\zeta_r / dS_r$ (linear region)	-7.6 MHz/(% trans)	4.1 MHz/(% trans)

Table 5.1 Parameters for a Single-Component PDV Test.

		Tunnel			
		Nominal	PDV	Bias	Random
M = 0.2		−14.2	-12.5	1.7	3.8
M = 0.3		-20.2	-19.7	0.5	3.0

		Jet, M = 1.36			
		LDV	PDV	Bias	Random
	x/D = 3	268	264	-4.0	8.8
Aggregate	x/D = 5	263	255	-8.3	9.1
	x/D = 7	251	244	-6.8	~0
	x/D = 3	268	252.8	-15.2	
$S_{c12} = 0.908$	x/D = 5	263	248.3	-14.7	
	x/D = 7	251	237.0	-14.0	
	x/D = 3	268	263.6	-4.4	
$S_{c12} = 0.870$	x/D = 5	263	255.4	-7.6	
	x/D = 7	251	243.7	-7.3	
	x/D = 3	268	268.8	+0.8	
$S_{c12} = 0.805$	x/D = 5	263	258.8	-4.2	
	x/D = 7	251	251.2	+0.2	
	x/D = 3	268	273.1	+5.1	
$S_{c12} = 0.805$	x/D = 5	263	265.5	+2.5	
	x/D = 7	251	250	-1.0	

Table 5.2 Measured Bias and Random Uncertainties for Single Component Tests.

Laser (x, y, z)	Camera (x, y, z)	System Sensitivity (x, y, z)
0, -0.170, 0.985	-1.0, 0, 0	-1.0, -0.171, 0.985
0, -0.170, 0.985	1.0, 0, 0	1.0, -0.171, 0.985
0, -1.0, 0	-1.0, 0, 0	-1.0, -1.0, 0.0
0, -1.0, 0	1.0, 0, 0	1.0, -1.0, 0.0

Table 5.3 Laser and Camera Unit Vectors with resulting System Sensitivity Vectors for Three-Component Forced Mach 1.36 Jet Experiment.

	Unit Vectors k_i and k_o (x,y,z)	System Sensitivity Vector (tunnel coordinates) k_{oi} (x, y, z)	System Sensitivity Vector (model coordinates) k_{oi} (x', y', z')
Laser	0.009, -1.00, 0.021		
Component 1	-0.802, -0.491, 0.339	-0.811, 0.509, 0.318	-0.871, 0.509, -0.024
Component 2	0.775, -0.554, -0.304	0.766, 0.446, -0.325	0.832, 0.446, 0.001
Component 3	-0.809, 0.48, 0.340	-0.817, 1.48, 0.319	-0.877, 1.48, -0.026

Table 5.4 Incident, observation, and system sensitivity vectors for three component PDV delta wing measurements in tunnel oriented and model oriented coordinate system for upstream positions of 62.8% and 85.7% root chord.

	Unit Vectors k_i and k_o (x,y,z)	System Sensitivity Vector (tunnel coordinates) k_{oi} (x, y, z)	System Sensitivity Vector (model coordinates) k_{oi} (x', y', z')
Laser	0.012, -1.00, 0.027		
Component 1	-0.829, 0.460, 0.317	-0.841, 0.539, 0.290	-0.887, 0.539, -0.062
Component 2	0.738, -0.591, -0.326	0.726, 0.409, -0.353	0.807, 0.409, -0.041
Component 3	-0.834, 0.448, 0.322	-0.846, 1.45, 0.294	-0.894, 1.45, -0.060

Table 5.5 Incident, observation, and system sensitivity vectors for three component PDV delta wing measurements in tunnel oriented and model oriented coordinate system for upstream positions of 97.1% and 108% root chord.

Case	Control Surface Angle (+ up)	Position 1 (-1 in)	Position 2 (1 in)	Position 3 (3 in)	Position 4 (5 in)	Position 5 (6.5 in)
1	0	X	-	X	X	X
2	-20	X	X	-	X	X
3	+20	X	-	X	X	X
4	Left Side -20 Right Side +20	X	X	X	X	-

Table 5.6 Trailing edge control surface deflection angle (positive is up) and PDV planes measured along the surface relative to the wing/body junction.

	Unit Vectors k_i and k_o (x,y,z)	System Sensitivity Vector (tunnel coordinates) k_{oi} (x, y, z)
Laser	-0.354, 0.016, -0.935	
Component 1	-0.726, 0.0448, 0.686	-0.372, 0.029, 1.62
Component 2	0.864, -0.464, -0.194	0.1.21, -0.480, 0.741
Component 3	-0.889, -0.423, 0.175	-0.535, -0.439, 1.11

Table 5.7 Incident, observation, and system sensitivity vectors for three component PDV Boeing UCAV model measurements in tunnel oriented coordinate system.

6. Uncertainty Analysis

During the course of developing PDV, several evaluations of the uncertainty and error have been conducted. The goal of the uncertainty analysis is first to determine the error in the measurement and secondly to identify error sources so that they can be reduced or even eliminated. Following is a description of two approaches which were taken to evaluate the uncertainty as the PDV system was developed. The first approach used single component experiments in the Mach 1.34 supersonic jet (Section 5.2.1) and 70 degree delta wing experiments (Section 5.2.2) conducted in the SARL. A detailed analysis of all the sources of error (which we considered major) was conducted so that they could be reduced as the system was developed. Second, we present an uncertainty analysis for multiple component measurements for the two component 70 degree delta wing case (described previously in Section 5.3.2). This indicates additional uncertainties and issues which can arise when calculating two velocity components from two PDV systems. This is followed by a summary of the uncertainty in the wind tunnel tests which were conducted as the PDV system was developed. This gives a good idea of the performance which can be expected from PDV. It should be noted that in the following analysis we have tried to be conservative in our estimates of uncertainties when evaluating the contribution from each individual source, therefore some of the estimates may be slightly higher then expected.

6.1. Detailed Uncertainty Analysis of Single Component Measurements in the wind Tunnel and Supersonic jet.

Errors in the velocity measurements may be classified as bias or random. The former occur consistently from measurement to measurement and degrade the accuracy of each individual measurement and of the average of a series of measurement to an equal extent. The latter fluctuate from measurement to measurement and degrade the precision of individual measurements. When measurements are averaged, the random error is reduced in proportion to the square root of the number of samples averaged.[33] Thus, by averaging a great number of samples, the random error associated with the mean measurement may be reduced. However, in the study of turbulence, statistics are calculated based upon a series of individual measurements,

135

and random errors in the individual measurements will appear as spurious turbulence. Therefore, it is desirable to minimize the random error and to quantify it, if possible.

One way to assess the errors is to compare the PDV measurements to known velocity standards. In the wind tunnel, the known standards were the empty tunnel runs at 68 m/s and 96 m/s. Turbulence intensities in this facility are estimated to be less than 0.1%. In the jet, the known standards were taken to be the mean and fluctuating velocities measured by LDV in the core. The bias error was calculated as the difference between the average PDV measured velocity and the average nominal velocity.

$$\Delta V_{Bias\_Error} = V_{Avg,PDV} - V_{Avg,nom}.$$

Equation 6.1

Because the PDV random error is not correlated with the actual flow velocity variations, it was calculated as

$$\Delta V_{Random\_Error} = \sqrt{V_{rms,PDV}^2 - V_{rms,nom}^2}.$$

Equation 6.2

Table 5.2 summarizes the measured bias and random errors in the small and large scale facilities. For the jet, errors in the core at three axial positions are presented for five data sets. The first case is comprised of all 100 instantaneous images. The other four cases are subsets of the full data set corresponding to four distinct laser set points, S_r, with average values of 0.908, 0.870, 0.805 and 0.677.

To understand the sources of these measured PDV errors we turn to the Doppler shift equation, which has been rearranged to give the velocity in the direction of PDV system sensitivity in terms of some intermediate quantities

$$V_{parallel} = \frac{\lambda}{2\sin\left(\frac{\phi}{2}\right)} \left[\zeta_c\left(S_{c12}\right) - \zeta_r\left(S_r\right) \right].$$

Equation 6.3

The term in brackets is the Doppler shift expressed in terms of the frequency functions, ζ_r and ζ_c. The frequency functions take as their arguments the transmission ratios recorded by the PDV camera system, S_{c12}, and the transmission ratio recorded by the frequency monitoring system, S_r. These ratios may be expressed in terms of directly measured quantities as

$$S_{c12} = m_c \frac{S_{c1}}{S_{c2}} \quad and \quad S_r = m_r \frac{v_r}{v_u}$$

Equation 6.4

136

Here S_{c1} and S_{c2} are the intensities measured at corresponding pixels in the filtered and unfiltered views of the flow. The quantities v_r and v_u are the signals that were recorded by the boxcar integrator from the filtered and unfiltered photodiodes. Note that in the analysis presented here, results from photodiodes are given, but similar reasoning is applied when using the Joule-meters. These scaling factors and their role in error propagation will be discussed further below.

According to the standard practice of error propagation, the contributions of uncorrelated (i.e. independent) error sources are added in quadrature to determine the total error in a measurement. The bias, random and total velocity errors may be expressed as:

$$\Delta V_{Bias} = \sqrt{\sum_i \left(\frac{\partial V}{\partial x_i} \Delta x_i \right)^2} \qquad \text{Equation 6.5}$$

$$\Delta V_{Random} = \sqrt{\sum_j \left(\frac{\partial V}{\partial y_j} \Delta y_j \right)^2} \qquad \text{Equation 6.6}$$

$$\Delta V_{Total} = \sqrt{\sum_i \left(\frac{\partial V}{\partial x_i} \Delta x_i \right)^2 + \sum_j \left(\frac{\partial V}{\partial y_j} \Delta y_j \right)^2} \qquad \text{Equation 6.7}$$

Here, the Δx_i are the uncorrelated sources of bias error in the independent variables and the Δy_i are the uncorrelated sources of random error in the independent variables.[33] The bias and random contributions to the error are separated in the foregoing equations in recognition of the fact that the random contributions can be reduced in the mean measurements but the bias contributions persist undiminished.

6.1.1. Bias Errors

Several mechanisms for bias error have been identified and modeled. The contribution of each of these mechanisms to the total bias error in velocity include:

1. uncertainty in the wavelength of the incident laser light, λ.
2. uncertainty in the angle between incident and scattered laser light, ϕ.
3. uncertainty in characterization of the camera filter frequency function, ζ_c, arising from:

   (a) scaling

(b) temperature drift of the sidearm of the saturated filter (in the jet case).

4. uncertainty in characterization of the monitoring filter frequency function, ζ_r, arising from:

(a) scaling

(b) temperature drift of the sidearm (for the case when starved cells are not used).

5. uncertainty arising from a baseline voltage drift in the boxcar integrator signals (or Joule-meters).

Each of these errors will now be discussed in more detail with subscripts of the dependent variable indicating which mechanism is being considered.

Uncertainty in the wavelength of the incident laser light is a negligible error source for the following reason. Its affect on velocity is given by standard error propagation as

$$\Delta V_1 = \frac{\partial V}{\partial \lambda} \Delta \lambda = \frac{V}{\lambda} \Delta \lambda = V \frac{\Delta \lambda}{\lambda}.$$ Equation 6.8

Clearly, the relative uncertainty introduced to the velocity measurement by this term is equal to the relative uncertainty in the wavelength itself. The wavenumber of the incident laser is constant to seven significant figures (18789.28 cm^{-1}). Therefore, bias error due to uncertainty in λ is negligible and will not be considered further.

Uncertainty in the angle ϕ arises from the limitation in the accuracy with which it can be measured and from variation across the field of view dependent on the experimental arrangement. For the experiments considered, it was estimated that this angle ϕ was known to within approximately $1°$. An analytic expression for the error arising from uncertainty in ϕ is

$$\Delta V_2 = \frac{\partial V}{\partial \varphi} \Delta \varphi = \frac{-V}{2 \tan\left(\frac{\varphi}{2}\right)} \Delta \varphi.$$ Equation 6.9

Note that this expression shows that the error in the velocity measurement introduced by this term is proportional to V itself therefore, the relative error is constant.

Before discussing the bias errors associated with the frequency functions, the method by which these function were determined will be reviewed. The functions were constructed from ordered pairs of calibration data, with each pair consisting of a voltage ratio from the

photodiodes that represents transmission and a voltage to the seed laser that represents frequency. These quantities were scaled to transmission and frequency, respectively. An advantage of the calibration method described previously is that the two frequency functions share a common frequency axis because the very same laser pulses calibrated each filter. Furthermore, the spectral features of iodine are known to great accuracy meaning that this common frequency axis can be scaled to great accuracy. Therefore, the frequency scaling is regarded as a negligible source of error, and the bias error arising from the frequency functions comes predominantly from the scaling of the transmission axes.

The axes for the camera filter and for the monitoring system filter were scaled independently. During the iodine calibration step the voltage ratios were normalized by their maximum values within the range used for frequency discrimination. Both frequency functions then spanned a range from approximately 0 to 1. For the camera filter, the spatial and intensity calibration step calibrates the frequency monitoring system to the PDV camera system. During data reduction, scale factors determined in this step for each pixel multiply the intensity ratio S_{c1}/S_{c2} to yield a transmission ratio S_{c12} that is then applied to the frequency function to obtain a frequency value. The goal here was to ensure that the frequency function ζ_c and the measured ratio S_{c12} had the same transmission scales.

To summarize the point of the preceding paragraphs, the error in the frequency functions was assumed to arise from the scaling of the transmission axes. This scaling error can first be represented as an uncertainty in the scaling factors, m_c m_r, of Equation 6.4. Taking the camera frequency function as an example, this scaling uncertainty can be thought of as a source of uncertainty in the transmission ratio, S_{c12}, so that

$$\Delta S_{c12,Scaling} = \frac{\partial S_{c12}}{\partial m_c} \Delta m_c = \frac{S_{c1}}{S_{c2}} \Delta m_c = S_{c12} \frac{\Delta m_c}{m_c}. \qquad \text{Equation 6.10}$$

An identical analysis applies to the monitoring frequency function. Here we see that the relative uncertainty in the scale of the frequency function is equal to the relative uncertainty in the transmission ratio itself. Thus, we have represented uncertainty in the frequency function as an uncertainty in the transmission ratio.

Since we do not have an analytic form for the frequency functions, we resorted to a numerical representation of the error in velocity arising from the scaling error of the frequency functions. First, the frequency function error was expressed as an error in transmission ratio as

given in Equation 6.10. Next, the velocity error for the camera frequency function was computed using both positive and negative deviations in the transmission ratio as

$$\Delta V_{3a} = \frac{1}{2}\left(\left| V\left(S_{c12} + \Delta S_{c12,Scaling}\right) - V\left(S_{c12}\right)\right| + \left| V\left(S_{c12} - \Delta S_{c12,Scaling}\right) - V\left(S_{c12}\right)\right|\right) \quad \text{Equation 6.11}$$

and similarly for the monitoring frequency function

$$\Delta V_{4a} = \frac{1}{2}\left(\left| V\left(S_{c34} + \Delta S_{c34,Scaling}\right) - V\left(S_{c34}\right)\right| + \left| V\left(S_{c34} - \Delta S_{c34,Scaling}\right) - V\left(S_{c34}\right)\right|\right). \quad \text{Equation 6.12}$$

It was seen earlier that the saturated versions of iodine filters are highly sensitive to sidearm temperature. For the initial single component measurements, we would have preferred to conduct our experiments using starved cells to eliminate this source of error. Only one starved cell was available for the initial single component tests however, and we required two cells for each experiment. One of the cells therefore, was saturated. Its sidearm was maintained at a constant temperature by a water-bath and a precision temperature controller to minimize this error source. To model the effect of a temperature drift in the sidearm on the velocity measurements, filter profiles were measured experimentally at sidearm temperatures ranging from 35 to 55° in increments of 5°. Slightly different analyses were performed for the single component jet and wind tunnel arrangements.

For the jet, a pressure-broadened starved cell was used to monitor the laser frequency and a saturated cell was used in front of the camera. The nominal temperature of the camera cell sidearm was 40°C. Using the frequency function associated with this nominal cell, transmission ratios for a selected velocity range were calculated. The frequency functions associated with the other sidearm temperatures were then used to compute different frequencies, and hence different velocities, based on the same transmission ratios. The differences in these velocities are the errors associated with large temperature drifts. For each test velocity, we have five velocities corresponding to the five different camera frequency functions at five different sidearm temperatures. From these points, it is possible to determine a local gradient $\partial V/\partial T$. This gradient is then used to compute the error in velocity based on the estimated uncertainty in the sidearm temperature.

$$\Delta V_{3b} = \frac{\partial V}{\partial T}\Delta T. \quad \text{Equation 6.13}$$

Note that when the camera filter is the saturated filter the error, in general, will be velocity dependent. Also, note that because the monitoring filter was starved, there is no similar error term for it in the jet experiments.

For the wind tunnel, a starved cell was used in front of the camera and a saturated cell was used to monitor the laser frequency. The nominal temperature of the monitoring cell was 40°C. Using the frequency function of this nominal cell in conjunction with the laser set-point transmission ratio, the frequency of the laser was determined. The frequency functions associated with the other sidearm temperatures were then used to compute different laser frequencies for the same transmission ratio. The differences between these frequencies and the nominal frequency lead to differences in velocities at the five different temperatures. In analogy to the case for the jet, from these points we can determine a gradient and compute an error in velocity based on the estimated uncertainty in the sidearm temperature as

$$\Delta V_{4b} = \frac{\partial V}{\partial T} \Delta T.$$

Equation 6.14

Note that when the monitoring filter is the saturated filter, the error is constant for all velocities and depends only on the laser set-point. Also, note that because the camera filter was starved, there is no similar error term for it in the single component wind tunnel experiments. The uncertainty in sidearm temperature used in the calculations to follow was $\pm 0.1\%$ C°.

The last of the bias errors to be modeled is the result of baseline drift in the voltages measured by the boxcar integrators. This error biases the transmission ratio of the monitoring system, S_r. The drift for the signals v_r and v_u propagates into the transmission ratio as

$$\Delta S_{r,Baseline} = S_r \sqrt{\left(\frac{\Delta v_{r,Baseline}}{v_r}\right)^2 + \left(\frac{\Delta v_{u,Baseline}}{v_u}\right)^2}$$

Equation 6.15

The drift has been estimated to be no more than 10 mV, and a typical voltage for the reference photodiode voltage v_u is 2.86 V. The bias error due to the voltage drift in the frequency monitoring transmission ratio therefore, never exceeds 0.005. This modest uncertainty, then, is significant mainly if the laser set-point has been tuned to a steep region of the frequency function. This bias propagates into the velocity error as

$$\Delta V_5 = \frac{1}{2}\left(\left|V\left(S_{34} + \Delta S_{34,Baseline}\right) - V\left(S_{34}\right)\right| + \left|V\left(S_{34} - \Delta S_{34,Baseline}\right) - V\left(S_{34}\right)\right|\right).$$

Equation 6.16

We have modeled the effect of a drift in the sidearm temperature and the effect of baseline voltage drifts in the boxcar integrators as bias errors. It should be noted that these effects are time-varying and, therefore, could be viewed as random errors rather than bias errors. However, the time scale associated with the temperature and boxcar drifts was assumed to be large compared to the time scale of a typical experiment. Therefore, the errors were considered bias errors.

To conclude the discussion of bias errors, we point out that there is one bias error that we have not modeled. This is the bias that can exist in the transmission ratio S_{12} because some of the light received by the camera system comes from sources other than single-scattering from seed particles. These sources are direct scattering off walls, windows, and the model and multiple-scattering involving at least one scattering event from a seed particle in the flow. The background subtraction step is an effort to remove the scattering that occurs with no seed present (i.e. direct scattering off the test facility); however, it cannot account for multiple-scattering involving the flow. The angles at which multiple-scattering occurs are not known and therefore neither is the frequency of the multiply-scattered light nor its effect on the measured transmission ratio. In some cases, a structure that lies outside the plane of the interrogating laser sheet is evident in a PDV image. This is a good indication that the velocity measurement in that portion of the image has been corrupted by direct or secondary scattering. Thus, for example, no reliable velocity measurements were possible where the sting and model appear in the PDV images presented previously. If the effect of secondary scattering is more subtle, then we may have difficulty in recognizing it.

The results of the bias error model as developed above for the jet facility and for the wind tunnel facility are now presented. The mechanisms outlined above combine in the form of Equation 6.5 to produce a total velocity error. For the jet, Figure 6.1 shows the measured frequency functions. The symbols show a laser set-point of 0.8 on the monitoring curve and the associated points on the camera curve corresponding to velocities ranging from 100 to 280 m/s. Note that this velocity range accounts for most of the usable portion of the camera curve and that increasing velocity corresponds to decreasing transmission. Figure 6.2 shows the absolute bias errors associated with this velocity range arising from each of the mechanisms discussed above. Note that the absolute bias error is relatively constant and does not vary significantly with velocity. This relative error is not shown since it would go to infinity when approaching zero

velocity. The solid curves give the total error. The reason that the error is constant is that the dominant error terms are associated with the laser set-point, which itself is constant. In fact, the dominant error term arises from the scaling error of the monitor frequency function. This is not surprising considering that the laser set-point has a high transmission ratio, and based on Figure 6.2, it is evident that bias errors are worsened for large transmission ratios. For the same reason, the error associated with the camera frequency function rises at lower velocities, which correspond to higher transmission ratios. The measured bias errors presented in Table 5.2 show this same trend to some extent. The worst bias errors occur when the laser set point is greatest ($S_r = 0.907$) and progressively smaller bias errors result as the set-point is diminished. The results for $S_r = 0.677$ do not conform to this pattern; however, there are only 8 instantaneous images contributing to this last case, whereas the other cases are based upon approximately 30 images each.

The base-line drift of the boxcar integrators is the second leading error term. Again, its effect is exacerbated by the high set-point and the relatively high slope of the frequency function at that set-point. The angular error and the temperature error are seen to be relatively unimportant. The measured bias error for the mean centerline velocity in the jet core is within the prediction of the modeled error for the case of the 0.8 set point.

For the single component wind tunnel tests, Figure 6.3 shows the measured frequency functions. The symbols show a laser set-point of 0.54 on the monitoring curve and the associated points on the camera curve corresponding to velocities ranging from -120 to 40 m/s. This velocity range accounts for most of the usable portion of the camera curve. Here increasing velocity corresponds to increasing transmission because we are using the high frequency side of the iodine line as the frequency discriminator rather than the low-frequency side. Figure 6.4 shows the absolute errors associated with this velocity range. At the negative velocities, all error terms contribute comparably, but for positive velocities, the scaling error of the camera frequency function becomes dominant as the transmission ratios become larger. Note that the scaling error of the monitor frequency function is less prominent for the wind tunnel than for the jet because the laser set-point has been reduced from 0.8 to 0.54. Consequently, the absolute errors expected for the wind tunnel are smaller than those predicted for the jet. The measured bias error for the wind tunnel very slightly exceeded the uncertainty predicted by the modeled bias error. Uncertainty in the angle Ω could account for this discrepancy.

6.1.2. Random Errors and Uncertainty

Turning to Equation 6.3, we will first determine those variables that do not contribute to random error. The wavelength λ and the angle ϕ do not contribute because they are specified once for all measurements and therefore their errors propagate systematically, not randomly. The frequency functions, ζ_c and ζ_r are determined before measurements of the flow field are undertaken. Errors associated with these functions may be either bias or random errors, depending on whether the characteristics of the filters change slowly or quickly relative to the time of the experiment. We have tentatively classified the errors arising from sidearm temperature drift as bias errors. The only remaining quantities are the transmission ratios S_{c12} and, S_r and random errors are associated with both of these.

The following mechanisms have been identified as sources of random error in the transmission ratios:

1. the radiometric noise associated with the CCD cameras (for S_{c12})

2. digital truncation errors associated with the boxcar integrators (for S_r)

3. laser speckle noise associated with imaging narrow line-width laser light (for S_{c12}).

4. Finally, there is a residual random error associated with the frequency monitoring system. The 4 MHz fluctuation measured during the empty tunnel test cannot arise from speckle or from the radiometric noise because the camera signals were spatially averaged. The only other source in our model is 2., which cannot amount to 4 MHz. Therefore, we include this residual error without positively identifying its source. Possibly, it arises from the combination of the laser frequency jitter and scaling errors in the frequency functions.

The first of these noise sources has been analyzed in PDV applications in great detail by McKenzie. [19,34] He describes radiometric noise in terms of three components: the amplified-circuit noise of the detector system (readout noise and dark charge), the inherent photon-statistical noise of the detection process, and the truncation of the signal in the analog to digital conversion. McKenzie based his calculations on a minimum unfiltered signal level (S_{c2}) of 1/10 of full-scale and assumed the use of a 16-bit scientific-grade CCD camera. He showed that the radiometric noise in the Doppler shift is less than 2 MHz over a 300 MHz range. Furthermore, he found that it was the photon-statistical component that dominated the radiometric noise.

We followed his analysis for the radiometric noise associated with a signal, S_{c1}, at a given pixel using the appropriate parameters for the PixelView SpectraVideo CCD cameras and our flow and seeding arrangements. The calculations for the noise are first performed in terms of photoelectrons and then converted to counts. The individual contributions to the radiometric noise will be discussed separately and then they will be combined in a single expression.

First, we consider the readout noise, which is denoted using McKenzie's nomenclature, as σ_{ro}. This is specified by PixelVision as 15-25 electrons (rms) per pixel at a readout rate of 500 kHz. Next, we consider the noise associated with dark charge. Dark charge noise arises from the thermally-generated electrons, which are not associated with the incident light. The mean dark charge at each pixel is given as the product of the dark current μ_{DC}, and the readout time for the CCD array Δt. The dark current is specified by the manufacturer and the readout time may be calculated based upon the chip size and the readout rate. The mean dark charge contribution to an image, S_{DC}, is subtracted when the background image is subtracted from the raw image. However, the noise associated with the variance of the dark charge remains. This noise is estimated according to Poisson statistics as $\sigma_{DC} = \sqrt{S_{DC}}$ [e⁻]. For the Pixelview SpectraVideo camera, which has a chip measuring 512 x 512 pixels and a readout rate of 500 kHz, the quantities discussed above are.

$$\Delta t = \frac{512^2 \, [pixels]}{500e3 \, [pixels/\sec]} = 0.52 \sec \qquad \text{Equation 6.17}$$

$$S_{DC} = \mu_{DC} \Delta t = 2 \frac{e^-}{\sec} 0.52 \sec = 1 \, [e^-] \qquad \text{Equation 6.18}$$

$$\sigma_{DC} = \sqrt{S_{DC}} = 1 \, [e^-]. \qquad \text{Equation 6.19}$$

Next, we consider the photon-statistical noise, which is denoted σ_ρ. This noise arises from statistical fluctuations in the incident light. Like the dark-charge noise, the noise associated with photon-statistics can be described according to Poisson statistics, so that

$$\sigma_p = \sqrt{S_i + B_i} \, [e^-] \qquad \text{Equation 6.20}$$

Here S_i and B_i are the signal and background intensities expressed in terms of electrons.

The radiometric uncertainty in the measurement of light intensity at a given pixel is then given by combining the independent error sources described above in quadrature so that:

$$\Delta S_i = \sqrt{\sigma_{RO}^2 + \sigma_{DC}^2 + \sigma_p^2} \ [e^-]$$

Equation 6.21

or

$$\Delta S_i = \sqrt{\sigma_{RO}^2 + S_{DC} + S_i + B_i} \ [e^-]$$

Equation 6.22

Note that the preceding equations are valid only when the terms are expressed in units of electrons. A final parameter is required to relate these equations to the camera readings in terms of counts. That parameter is the system conversion gain, G_{AD}, which is expressed in terms of electrons per count. For the PixelView camera, the value is 5 electrons/count. The radiometric uncertainty *in terms of counts* may then be expressed as

$$\Delta S_i = \frac{1}{G_{AD}} \sqrt{\sigma_{RO}^2 + S_{DC} + G_{AD}\left(S_i + B_i\right)} \ [counts]$$

Equation 6.23

Here σ_{RO} and S_{DC} are expressed in terms of electrons and S_i and B_i are expressed in terms of counts. This mixed form of the equation is supplied because the literature gives the former quantities in terms of electrons and the latter quantities are most conveniently measured in terms of counts. Measured in terms of counts, the radiometric noise cannot have a value less than 1 count. The 1 count minimum is the limitation imposed by digital truncation. For the wind tunnel and jet, typical values of S_{c2} the reference image intensity, were taken to be 5000 and 30000 counts, respectively. B_2 was taken to be approximately 0.05 times the value of S_2. Values for S_{c1} and B_1, the signal image intensities, were calculated based upon the nominal laser set-point, S_r, the Doppler shift, and the frequency functions. For the signal levels encountered in the present experiments, the photon-statistical noise dominated the other radiometric noise sources.

The effect of the radiometric noise on the velocity measurements was then be found through propagation of errors in a manner similar to what we have seen above

$$\Delta S_{c12,rad} = S_{c12} \sqrt{\left(\frac{\Delta S_{c1}}{S_{c1}}\right)^2 + \left(\frac{\Delta S_{c2}}{S_{c2}}\right)^2}$$

Equation 6.24

and

$$\Delta V_{rad} = \frac{1}{2}\left(\left|V\left(S_{12} + \Delta S_{12,rad}\right) - V\left(S_{12}\right)\right| + \left|V\left(S_{12} - \Delta S_{12,rad}\right) - V\left(S_{12}\right)\right|\right).$$

Equation 6.25

It is interesting to note that the preceding analysis for radiometric error applies to individual pixels. Because low-pass filtering was utilized in the current experiments, which in a sense

146

combines pixels, we expect that we are being conservative in our modeling of the radiometric noise. McKenzie has reported experimentally that the overall noise in the transmission ratio is inversely proportional to the number of pixels binned. He has provided a theoretical justification suggesting that the noise should be inversely proportional to the square root of the number of pixels binned.[19] While these two statements are contradictory, they suggest the same trend: low-pass filtering reduces radiometric noise.

The second of the noise sources is the digital truncation associated with the box-car integrators. This truncation error is equivalent to a 2.5 mV variation in the voltages, v_u and v_r. The propagation of this error into the transmission ratio S_r, can be calculated in exact analogy to that of the base-line drift of the boxcar integrators as in Equation 6.15.

The third source of random error, laser speckle, strongly dominates the contributions of the other two sources. Speckle noise is introduced when laser light is scattered off a surface or from a cloud of particles and small differences in path length cause three-dimensional interference patterns. In the PDV technique, ratios are taken of the signal and reference images. If the speckle pattern in these image pairs were perfectly correlated, then the ratioing step would remove the speckle noise. However, the speckle pattern does not exhibit perfect correlation. Part of the reason for this is imperfect mapping so that corresponding pixels in the two images do not necessarily correspond to exactly the same flow regions. The mapping is imperfect for two reasons: one, the dot-finding algorithm and bilinear interpolation do not exactly capture the differences in views, and two, vibrations cause the camera views to shift slightly during the course of a run. The dot-finding algorithm, however, is believed to find the dot centers consistently to better than a tenth of a pixel. Even if the mapping were perfect, minute differences in path length between the signal and reference images could degrade the correlation in speckle patterns since speckle patterns are three-dimensional.

Assuming the speckle patterns are completely uncorrelated in the signal and reference images and applying the standard error propagation analysis for uncorrelated noise, we can express the noise in the transmission ratio as

$$\Delta S_{12,Speckle} = S_{12} \sqrt{ \left(\frac{\Delta S_{1,Speckle}}{S_1} \right)^2 + \left(\frac{\Delta S_{2,Speckle}}{S_2} \right)^2 } \qquad \text{Equation 6.26}$$

McKenzie has pointed out that for speckle-dominated noise, the noise-to-signal ratio is constant with respect to intensity.[34] Therefore, the terms under the radical are constant, and the noise in the transmission ratio may be considered to be proportional to the transmission ratio itself. In the empty wind tunnel runs, where turbulence levels were estimated to be below 0.1%, an approximately uniform Doppler image was anticipated. Any appreciable spatial variation (noise) in this image was therefore, attributed to laser speckle. The inherent jitter of the laser was used to evaluate the validity of equation 6.26. In the high vibration environment of the wind tunnel the laser displayed a frequency jitter with an rms variation of 41 MHz. This led to mean transmission ratios, S_{c12}, ranging from about 0.3 to 0.8. This occurred despite the fact that the nominal set-point was fixed to 0.54 and the flow was steady. In the jet, four different laser set points were utilized and there was less frequency jitter in the mean transmission ratios about those positions. Figure 6.5 shows a plot of the spatial variation in transmission versus the mean transmission for each image in the empty wind tunnel measurements. The three curves correspond to three levels of low-pass filtering, a procedure meant to mitigate the speckle noise. The data is approximately linear, suggesting that speckle noise is indeed the dominant noise source. Without filtering, the speckle noise ($\Delta S_{c12}/S_{c12}$) has a value of about 9%. Low-pass filtering is seen to reduce the speckle noise from 9% to 5% for 3x3 filtering and to 3% for 5x5 filtering. Similar calculations were performed for the jet where a relatively uniform section of the jet core was used to compute the spatial noise in each image. In this case, low-pass filtering was seen to reduce the speckle noise from 7% to 5% for 3x3 filtering and to 4% for 5x5 filtering.

The effect of the speckle noise on the random error in velocity is given by

$$\Delta V_{Speck} = \frac{1}{2}\left(\left|V\left(S_{12}+\Delta S_{12,Speck}\right)-V\left(S_{12}\right)\right|+\left|V\left(S_{12}-\Delta S_{12,Speck}\right)-V\left(S_{12}\right)\right|\right). \qquad \text{Equation 6.27}$$

Figure 6.6 shows absolute random error in velocity arising from the sources discussed above for the jet over a selected velocity range. Figure 6.7 show the results for the wind tunnel. The waviness appearing in some of these curves is the result of the numerical differentiation of the experimentally measured frequency functions. Clearly, laser speckle is the dominant random error source.

In the jet facility, the modeled random error (3 m/s) is considerably less than the measured random error (9 m/s). A possible explanation for this is the use of four different laser set points in obtaining the 100 images used to compute the RMS velocity in the jet. Bias errors

in the PDV system lead to four distinct mean measurements in each subset of jet data (see Table 5.2). These bias errors may then increase the measured velocity fluctuations above the level attributable to speckle noise. Another possibility is that the turbulence level in the jet core is actually closer to that indicated by PDV than LDV. The reasoning behind this argument is that the smaller, lighter ethanol seed particles used in PDV can follow small-scale fluctuations in the core better than the larger, heavier aluminum oxide particles used in the LDV measurements. The modeled random error in velocity for the wind tunnel (2.5 m/s) agrees with measured random error (3 m/s).

It should be noted that one error source that we have not treated explicitly is the error associated with image mapping. Despite the dot-finding and mapping procedures, some residual error exists in overlaying the images. The low-pass filtering procedure reduces this error source, which is not expected to be particularly significant in the current experiments. Few researchers have addressed the topic of this residual error quantitatively. Clancy et al. have made an attempt in which an estimate of the residual misalignment expressed as a fraction of a pixel is combined with a representative gradient in signal intensity to calculate the associated errors in the transmission ratio, the Doppler shift and then the velocity.[14,35] This approach may be successful in flows with relatively constant seeding, such as a jet flow. Here representative gradients in signal intensity can be found. Clancy, in fact, categorized this source of error as a bias error because the registration errors are constant from image to image and the intensity gradients in a jet flow are arguably approximately constant as well. In a flow where the seeding is fluctuating and irregular, such as the delta wing flow, no meaningful estimate of the gradient can be found. The errors introduced by image misalignment are expected to be more random in nature because the signal gradients fluctuate so much. McKenzie adds mapping noise in quadrature as a term to the random uncertainty in an equation analogous to equation 6.26. Thus, there are differing opinions as to whether mapping errors contribute predominantly to bias or random errors, but probably this issue is somewhat flow dependent. Neither of these analysis methods explicitly accounts for the effect of mapping errors on the calibration of the cameras. The chief ways to reduce the contributions of mapping errors are to map accurately and to bin or low-pass filter.

Table 6.1 and Table 6.2 list the error sources that are classified as either bias or random. Their propagation to velocity, and where appropriate into frequency, are indicated. These values are computed for conditions in the jet core and in the empty wind tunnel at 68 m/s, respectively.

From these tables, it is evident that the largest source of bias error derives from the scaling of the frequency functions and the largest source of random error is speckle noise.

There are two ways to think of the modeled random error in velocity. First, if we can be confident that we have modeled this error correctly, we may subtract it in quadrature from the measured PDV fluctuations to obtain a corrected value for the velocity fluctuations. In this manner, fluctuations less than the random error can be measured. Obviously, if the modeled random error is greater than the uncorrected PDV fluctuations, then there is a discrepancy and this procedure cannot be accepted. Second, (and more conservatively) the modeled random error can be thought of as a lower bound on the measurable velocity fluctuations. For velocity fluctuations equal in magnitude to the random error, the measured PDV fluctuations would have a value greater than either one alone by a factor of $\sqrt{2}$ because they are uncorrelated. As the velocity fluctuations become larger, the contribution of the random error quickly becomes negligible. For a signal-to-noise ratio of 4 (i.e. for flow fluctuations four times the magnitude of the noise) the random error accounts for less than 4% of the measured PDV fluctuation.

One additional point should be made regarding the bias error in the PDV measurements. In the preceding analysis, the measured quantity was the velocity component in the direction of PDV system sensitivity. In other words, no attempt was made to describe the direction of the velocity vector itself. In cases where the velocity direction is presumed known, an additional bias error arises related to the uncertainty in the angle Ω between the velocity vector and the PDV system sensitivity. An analytical expression for this error is

$$\Delta V_{\Omega} = \frac{\partial V}{\partial \Omega} \Delta \Omega = V \tan(\Omega) \Delta \Omega \qquad \text{Equation 6.28}$$

For the empty tunnel wind tunnel measurements, this error source can explain discrepancies between the measured and modeled bias error. The reason this term was omitted previously is that it is not an error of the PDV system itself, but an error associated with our attempt to relate the PDV measurement to a presumed velocity direction. Also, note that the PDV system is most sensitive and the uncertainty is minimized when the directions of the velocity vector and of the system sensitivity are either parallel or anti-parallel, i.e. for Ω equal to 0° or 180°.

6.2. Uncertainty Analysis of Multiple Component Measurements

We are mainly interested in the capability of the PDV system to measure the average velocity in the flow. We will consider only error associated with the average measurements in the uncertainty analysis for the multiple component measurements presented here. In addition, all of the cameras had identical iodine transmission profiles so they do not need to be considered independently. We can access the uncertainty in a manner similar to the previous analysis for single component PDV systems. For multi-component systems, we will first calculate the general uncertainty of the Doppler shift measured and then access the uncertainty of each velocity component we wish to measure. As a reference for the uncertainty analysis, we will consider numbers from a single PDV camera system (Camera 2) and nominal values for the empty tunnel test. The other PDV systems should have similar levels of uncertainty since the equipment is identical. It should be noted that this is a more general uncertainty analysis with the goal of evaluating the overall uncertainty associated with the system. We begin our multiple component analysis with the measured Doppler shift which is given by

$$\Delta f_D = \left[\zeta_c \left(S_{c12} \right) - \zeta_r \left(S_r \right) \right]$$
Equation 6.29

Here ζ_c and ζ_r are the frequency functions (iodine transmission profiles) of the camera and wavemeter respectively. Again, the frequency functions take as the argument the transmission ratios recorded by the signal and reference PDV cameras S_{c12} and the transmission ratio recorded by the frequency monitoring system S_r. Since we will be computing the uncertainty numerically, instead of the term by term analysis which was conducted previously, we will simplify the analysis. This is accomplished by considering the linear portion of the transmission curves and combining the details of the sources of uncertainty into calibration slope and intercept terms.[29] Assume a linear transmission profile for the iodine cells and parameters to calibrate the signal and reference cameras together and we can write Equation 6.29 as

$$\zeta_c \left(S_{c12} \right) - \zeta_r \left(S_r \right) = m_c \frac{m_{cal} S_{c1} + b_{cal}}{S_{c2}} + b_c - m_r \frac{S_{r1}}{S_{r2}} - b_r$$
Equation 6.30

Here as before S_{c1} and S_{c2} are the intensities of the signal and reference cameras and S_{r1} and S_{r2} are the intensities from the signal and reference photodiodes on the wavemeter system. The slope and intercept for the camera filter are m_c and b_c respectively and m_r and b_r are the transmission slope and intercept for the reference filter. Finally, m_{cal} and b_{cal} are the slope and

intercept from the camera calibration. Since we always subtract the background image the contribution of b_{cal} is negligible (assuming the background does not change from the measurement). Again using standard quadrature addition of the independent error sources the uncertainty in the Doppler shift can be written as

$$Uncertainty \ in \ \Delta f_D = \sqrt{\sum \frac{\partial \Delta f_D}{\partial x_i} x_i} \qquad \text{Equation 6.31}$$

First considering the linearized frequency function terms of the camera and reference iodine transmission profile we can determine the uncertainty in m_r and m_c and the uncertainty in b_r and b_c. A bias uncertainty can be found in these quantities by considering the variation from the scans taken at the beginning to the end of each day. This can be estimated by lining up the reference cell profile for each testing day and computing how much the camera cells vary between each profile taken. This has been measured for the current experiments to be to be 6.6 MHz/(Transmission ratio) and 1.4 MHz for m_c and b_c respectively. The uncertainty in m_r and b_r are expected to be the same since a similar type of iodine cell was used with similar characteristics. Considering the random uncertainty for a starved iodine cell, the uncertainty in m_r and m_c is due to the temperature variation of the cell body due to the heater and temperature controller. Since these are starved cells, there is essentially no variation in the iodine number density. The temperature variation results in a random uncertainty of 0.11 MHz/(Transmission ratio) and 0.34 MHz for the slope and intercept. This result assumes that the cell body temperature varies by approximately 0.5K and the cells have a sensitivity of 0.21 MHz/K and 0.34 MHz/K as previously reported.

The next source of uncertainty is associated with random camera noise which is due to laser speckle. As noted previously speckle dominated noise has a characteristic that the noise to signal ratio is approximately constant. For the present set of experiments, we can measure the noise to single ratio of smoothed images in the empty tunnel tests. In regions where the intensity is approximately constant, we find that $\Delta S_1/S_1$ and $\Delta S_2/S_2$ are approximately 3.4% for 7 by 7 smoothing variations range from 1.8% to 5.0%. This contributes as a random noise source. The bias camera noise can be considered primarily due to inaccuracies of the camera calibration coefficient. Uncertainties in the camera calibration coefficient can be evaluated by considering the pixel to pixel variation of the slope in a small region of the green card calibration images. The slope should change slightly across the entire image due to optical differences between the

signal and reference cameras. The standard deviation of the slope variation was measured to be approximately 0.8 % for the standing green card images used in processing the present data.

For the frequency monitoring system, the major source of uncertainty is random and due to the resolution of the A/D converter on the SR computer control module. This resolution is approximately 2.5 mV. Considering typical values for S_{r1} and S_{r2} for this experiment the random signal to noise error is approximately 0.14 % for $\Delta S_{r1}/S_{r1}$ and 0.07% for $\Delta S_{r2}/S_{r2}$. Since this may be a slightly optimistic estimate we will consider that the uncertainty in $\Delta S_{r1}/S_{r1}$ and $\Delta S_{r2}/S_{r2}$ to be at least 1% due to vibration and set-up variations.

These uncertainties are tabulated in Table 6.3. To calculate the resulting uncertainty we evaluated equation 6.30 at typical average values found in the experiment. We then changed values by the amount of the predicted uncertainty and recalculated the result. This is essentially the same as finding the derivative of the frequency in terms of each independent variable. As seen in the table the total uncertainty in bias and random frequency is approximately 4.8 MHz and 11.0 MHz respectively. Although the random error is significantly higher, it should always be noted that a significant component of the random uncertainty (65%) is the speckle noise, which is greatly reduced when the images are averaged together for mean measurements. This compares well the magnitude of bias and random uncertainty estimates found previously. These errors were on the order of 3.8 and 8.0 MHz for the single component Delta wing test and 7.4 MHz and 11.9 MHz for the 56 delta wing generic fighter model. It should be noted that this uncertainty is based on nominal values of the quantities for the empty tunnel experiments and can be higher or lower in the actual experiment depending on the signal level and velocity. In addition it should be remembered that this represents a linear approach and as data points move into the nonlinear region the uncertainty may change, although this is generally limited by thresh holding the measured transmission ratio.

Now that we have a value for the uncertainty in the frequency, we can evaluate the propagation of the uncertainty for multiple component measurements. Consider again the present case where we are measuring two velocity components using Equation 4.18. We can consider that each independent vector has an uncertainty associated with it which will be estimated to be approximately 2% based on our ability to make accurate distance measurements. This should be considered a bias uncertainty since the vectors are not expected to change randomly due to any significant vibration. In addition there is an uncertainty associated with the

measured frequency as derived previously for each PDV camera component used to resolve the desired velocity components (axial and spanwise for our present case). The uncertainty for the axial and spanwise velocity components can be written as

$$\Delta V_{x'} = \left\{ \left[\frac{\partial V_{x'}}{\partial(\Delta f_{D1})}\Delta(\Delta f_{D1}) \right]^2 + \left[\frac{\partial V_{x'}}{\partial(\Delta f_{D2})}\Delta(\Delta f_{D2}) \right]^2 + \left[\frac{\partial V_{x'}}{\partial(k_{oi1x})}(\Delta k_{oi1x}) \right]^2 + \left[\frac{\partial V_{x'}}{\partial(k_{oi1y})}(\Delta k_{oi1y}) \right]^2 + \left[\frac{\partial V_{x'}}{\partial(k_{oi2x})}(\Delta k_{oi2x}) \right]^2 + \left[\frac{\partial V_{x'}}{\partial(k_{oi2y})}(\Delta k_{oi2y}) \right]^2 \right\}^{1/2} \quad \text{Equation 6.32}$$

$$\Delta V_{y'} = \left\{ \left[\frac{\partial V_{x'}}{\partial(\Delta f_{D1})}\Delta(\Delta f_{D1}) \right]^2 + \left[\frac{\partial V_{x'}}{\partial(\Delta f_{D2})}\Delta(\Delta f_{D2}) \right]^2 + \left[\frac{\partial V_{x'}}{\partial(k_{oi1x})}(\Delta k_{oi1x}) \right]^2 + \left[\frac{\partial V_{x'}}{\partial(k_{oi1y})}(\Delta k_{oi1y}) \right]^2 + \left[\frac{\partial V_{x'}}{\partial(k_{oi2x})}(\Delta k_{oi2x}) \right]^2 + \left[\frac{\partial V_{x'}}{\partial(k_{oi2y})}(\Delta k_{oi2y}) \right]^2 \right\}^{1/2}$$

Here the independent variables are the Doppler Shift and two components of the system sensitivity vector for each PDV camera system. The uncertainty calculated using Equation 6.32 would mainly be considered bias, but the uncertainty in the Doppler shift also contains a random component. In the analysis performed here, the uncertainty is solved numerically in a slightly modified method than previously discussed. To obtain the uncertainty in this analysis we will use the actual data for the empty tunnel test and change the independent parameter in Equation 6.32 by the amount of the uncertainty. In this way, the terms for quadrature addition can be evaluated for each independent parameter. This analysis will be conducted for each camera combination used to calculate the two velocity components investigated in this study.

Table 6.4 gives the uncertainty associated with each independent variable found in Equation 6.32 and the resulting uncertainty in the two components measured in this study again at the quantities evaluated for free stream conditions. The uncertainty analysis was preformed using all three combinations of signal and reference cameras. As is observed here the uncertainty is the highest using PDV components 1&3 and much less (50% to 64%) when using the other camera combinations. This higher error was also observed when evaluating this combination of components in Figure 5.35. This figure had a much higher distortion and noise level than the other combinations. For the PDV combination used in the computation of the axial and spanwise velocities in this study (components 2&3) the bias uncertainty was 3.4 m/s and 2.19 m/s respectively. The random uncertainty was 6.53 m/s and 4.84 m/s respectively. It should always be noted that a significant component of the random uncertainty (65%) is the speckle noise which is greatly reduced when the images are averaged together. As expected, the uncertainty in multiple component measurements are higher than the single component

measurements. This is due to combining two independent measurements with their own uncertainties. The uncertainty of the mean freestream velocity is 5.3% which agrees well with the actual measurement. The mean spanwise uncertainty is lower than the error measured in the actual experiment, but is of the same order. It should be noted that there was considerable time and technique required to reduce the uncertainties associated with the frequency to the current level. Considering that the uncertainty bias is 4.8 MHz and the width of the laser is on the order of 100 MHz a narrower linewidth laser may be needed to further reduce this uncertainty.

6.3. Summary of Uncertainty Analysis

In summary an uncertainty analysis was performed in detail on the single component PDV system and multiple component PDV system to investigate not only the level of the current measurement uncertainty, but also the major sources of this uncertainty. In general, the uncertainty is found to be somewhat static, varying slightly with velocity measured (making the technique better suited for high speed flows). Table 6.5 gives the error and uncertainty in the empty tunnel or core jet velocity tests conducted. The current level of measured error ranges from 0.5 to 1.7 m/s for bias and 0.35 to 3.8 m/s for random in empty tunnel, single component tests. Computed uncertainties for these tests range from 1.25 to 2.3 m/s for bias and 2.5 to 3.5 m/s for random. From measurements of the jet core velocity, single component PDV results had an error of 6.3 m/s and 6.0 m/s out of a measured velocity of 261 m/s in the direction of system sensitivity. It should be noted that the random uncertainty is due mostly to laser speckle noise, which is greatly reduced to negligible levels when computing mean velocity fields using a sufficient number of images. Three components were successfully measured in the supersonic jet and two components were successfully measured in the large scale wind tunnel. The bias error in multiple component measurements was 3.2 m/s with a computed uncertainty of 3.4 m/s for a velocity of 63.7 m/s. Although PDV is a somewhat difficult technique to implement and requires some experience and expertise, the current system allows users to investigate flow fields of research interest, particularly those with vortices inducing large velocity gradients. Methods for reducing errors should still be sought as technologies improve (i.e immediate data reduction, narrower linewidth lasers, improved cameras, etc.).
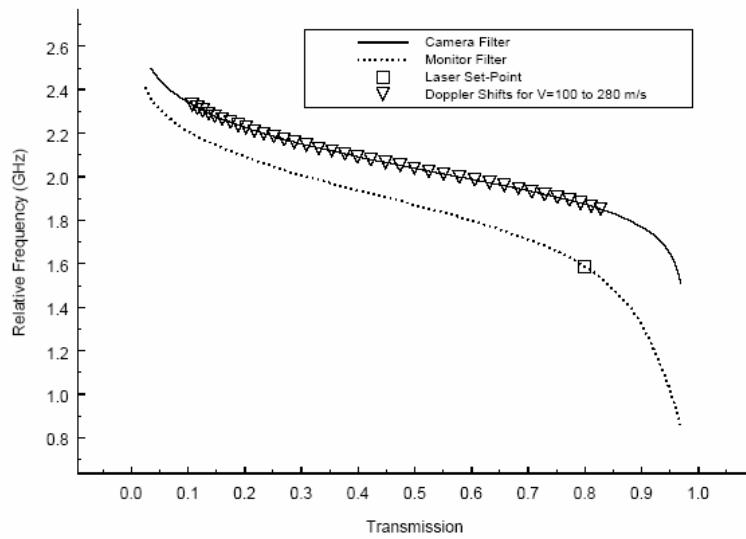
Figure 6.1 Frequency functions, ζ_c and ζ_r, used in single component jet experiments showing Doppler shifts for velocities from 100 to 280 m/s.
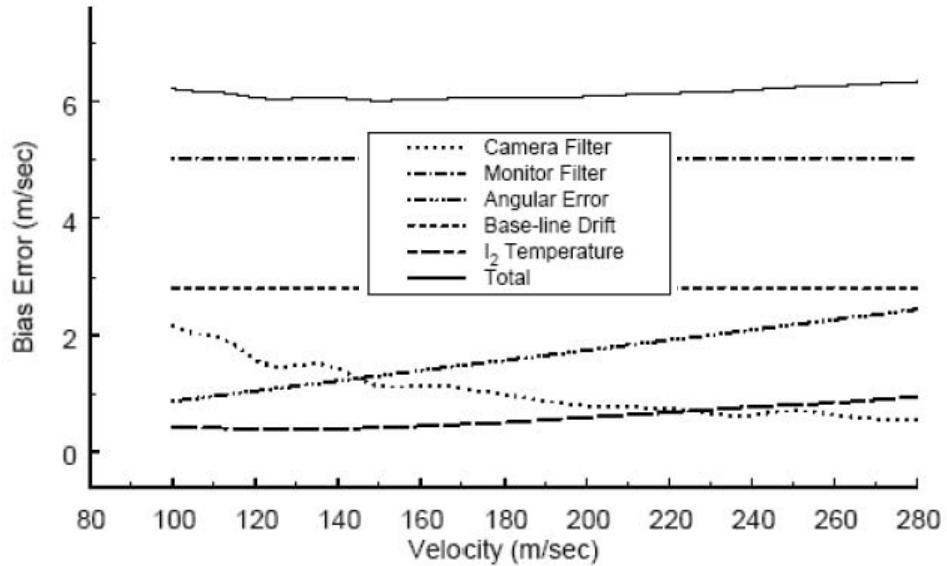
Figure 6.2 Modeled bias errors within the velocity range of the single component jet experiments. A laser setpoint, S_r, equal to 0.8 was used for these calculations.

156
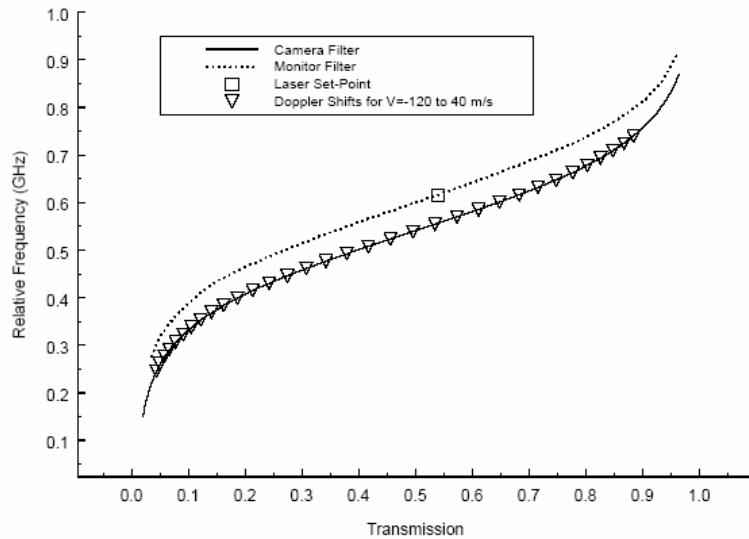
Figure 6.3 Frequency functions, ζ_c and ζ_r, used in single component wind tunnel experiments showing Doppler shifts for velocities from -120 to 40 m/s.
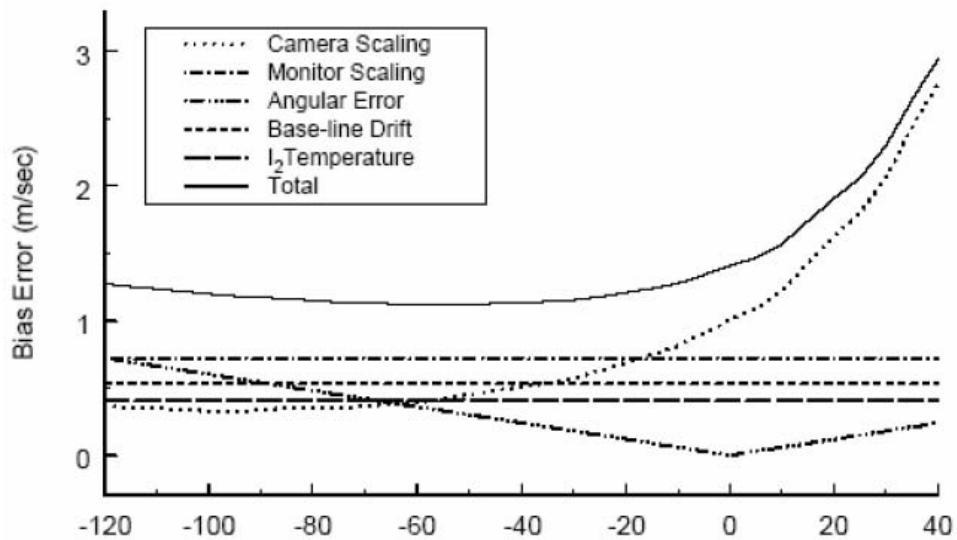
Figure 6.4 Modeled bias errors within the velocity range of the wind tunnel experiments. A laser setpoint, S_r, equal to 0.54 was used for these calculations.
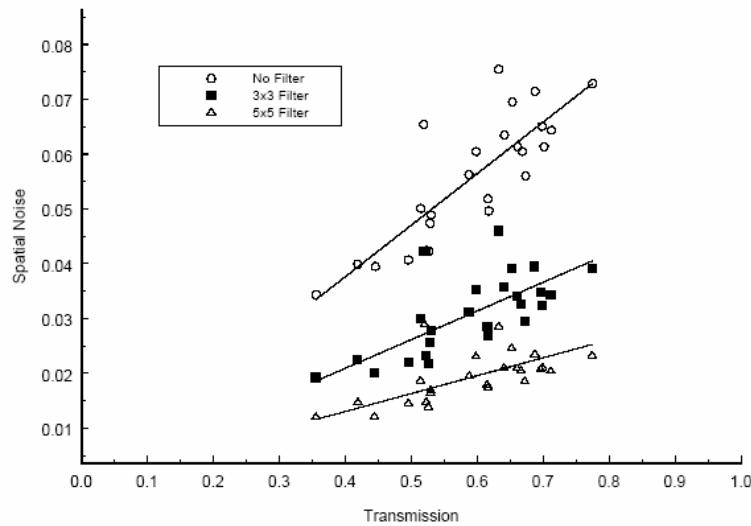
Figure 6.5 Effect of spatial filtering on speckle noise for the wind tunnel experiments. The spatial fluctuation of the camera transmission ratio is plotted against the mean transmission ratio for a series of images.
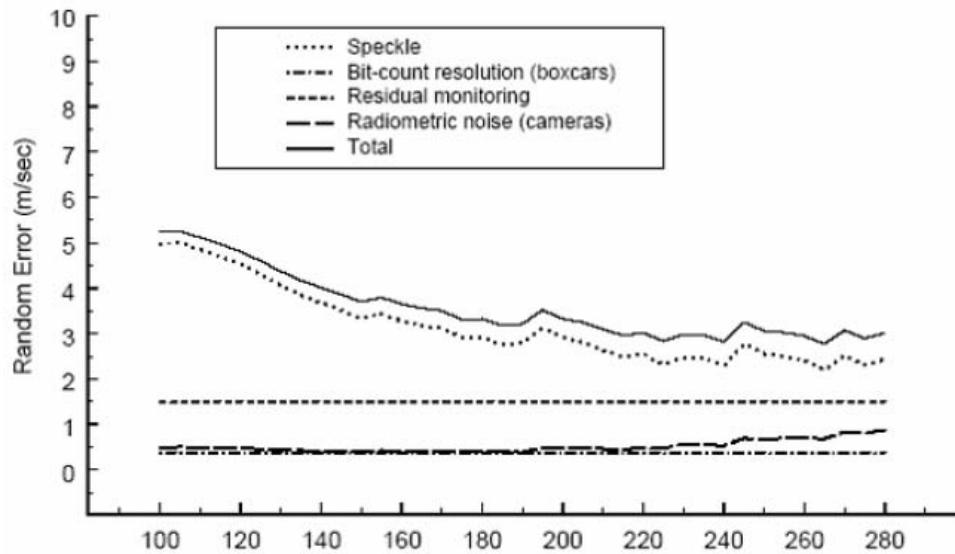
Figure 6.6 Modeled random error within the velocity range of the jet experiments.
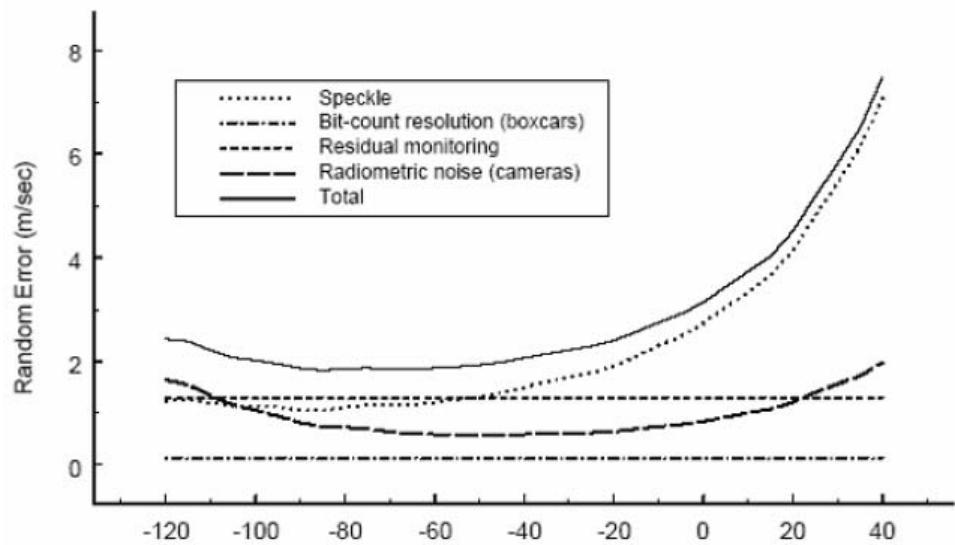
Figure 6.7 Modeled random error within the velocity range of the wind tunnel experiments.

Bias Error Source	Error Contribution to Jet Core Measurements
uncertainty in λ	negligible
uncertainty in ϕ	2.3 m/s
uncertainty in scaling of ζ_c	0.64 m/s (1.7 MHz)
uncertainty in scaling of ζ_r	5.0 m/s (13.3 MHz)
uncertainty in sidearm temp of camera filter	0.85 m/s (2.3 MHz)
base line drift of boxcars	2.8 m/s (7.4 MHz)
Total Bias Error	5.8 m/s
Random Error Source	
radiometric noise of CCD detectors	0.7 m/s (1.9 MHz)
digital truncation error of boxcars	0.37 m/s (1 MHz)
speckle	2.6 m/s (6.9 MHz)
residual monitor error	1.5 m/s (4 MHz)
Total Random Error	3.0 m/s

Table 6.1 Modeled Bias and Random PDV Errors for Mach 1.36 Jet with $S_{c12} = 0.8$ and V=260 m/s.

Bias Error Source	Error Contribution to Wind Tunnel Measurements
uncertainty in λ	negligible
uncertainty in ϕ	0.09 m/s
uncertainty in scaling of ζ_c	0.76 m/s (2.4 MHz)
uncertainty in scaling of ζ_r	0.72 m/s (2.2 MHz)
uncertainty in sidearm temp of monitor filter	0.41 m/s (1.3 MHz)
base line drift of boxcars	0.53 m/s (1.6 MHz)
Total Bias Error	1.25 m/s
Random Error Source	
radiometric noise of CCD detectors	0.7 m/s (2.2 MHz)
digital truncation error of boxcars	0.12 m/s (0.4 MHz)
speckle	2.1 m/s (6.5 MHz)
residual monitor error	1.3 m/s (4 MHz)
Total Random Error	2.5 m/s

Table 6.2 Modeled Bias and Random Single Component PDV Errors for SARL Wind Tunnel with $S_{c12} = 0.8$ and V=14.2 m/s.

	Uncertainty in Independent Variable		Typical Uncertainty in Doppler Shift Frequency [MHz]	
	Bias	Random	Bias	Random
m_c (MHz/trans)	6.6	0.11	2.43	0.041
b_c (MHz)	1.4	0.34	1.40	0.34
$\Delta S_{r1}/S_{r1}$	-	3.4%	-	2.70
$\Delta S_{r2}/S_{r2}$	-	3.4%	-	2.68
m_{cal}	0.008	-	1.75	-
$\Delta S_{c1}/S_{c1}$	-	3.4%	-	7.42
$\Delta S_{c2}/S_{c2}$	-	3.4%	-	7.17
m_r (MHz/trans)	6.6	0.11	3.18	0.053
b_r (MHz)	1.4	0.34	1.40	0.34
Total			4.80 MHz	11.0 MHz

Table 6.3 Modeled Bias and Random Uncertainties for Multiple Component PDV SARL Delta Wing Measurements.

| From Eqn. 46 | Uncertainty in Independent Variable | | Typical Uncertainty in Doppler Shift Frequency [MHz] | | | | | |
| | | | PDV Components 1 & 2 | | PDV Components 1 & 3 | | PDV Components 2 & 3 | |
	Bias	Random	Axial Vel. (m/s)	Spanwise Vel. (m/s)	Axial Vel. (m/s)	Spanwise Vel. (m/s)	Axial Vel. (m/s)	Spanwise Vel. (m/s)
k_{oi1x}	2 %	-	0.8	1.3	2.1	1.2	-	
k_{oi1y}	2 %	-	0.1	0.1	0.1	0.1	-	
k_{oi2x}	2 %	-	0.8	1.3			1.1	0.6
k_{oi2y}	2 %	-	0.1	0.1			0.1	0.1
k_{oi3x}	2 %	-	-	-	0.8	1.4	0.4	0.7
k_{oi3y}	2 %	-	-	-	0.1	0.1	0.1	0.1
Δf_{D1} [MHz]	4.8	-	1.4	2.6	4.5	2.6	2.3	1.4
Δf_{D2} [MHz]	4.8	-	1.6	2.7	1.5	2.6	0.7	1.3
Δf_{D1}* [MHz]	-	11.0	3.2	6.0	10.3	6.1	5.3	3.1
Δf_{D2}* [MHz]	-	11.0	3.7	6.3	3.5	6.1	1.6	3
Bias Total			2.41	4.18	6.75	4.12	3.4	2.19
Random Total*			5.45	9.65	12.8	9.56	6.53	4.84

Table 6.4 Modeled Bias and Random Uncertainties for Multiple Component PDV SARL Delta Wing Measurements.

	Measured Error (m/s)		Computed Uncertainty (m/s)	
Experiment (Velocity in direction measured)	Bias	Random	Bias	Random
Mach 1.36 Jet Core Single Component (261 m/s)	6.3	6.0	5.8	3.0
Mach 0.2 Empty Tunnel Single Component (-14.2 m/s)	1.7	3.8	1.25	2.5
Mach 0.3 Empty Tunnel Single Component (-20.2 m/s)	0.5	3.0	-	-
Mach 0.2 Empty Tunnel Single Component**Error! Bookmark not defined.** (-18.9 m/s)	1.0 (avg) to 1.5 (ins)	0.35 (avg) to .95 (ins)	2.3	3.5
Mach 1.34 Jet Core Multiple Components[24] (399 m/s)	< 7.2	10	7.0	16.2
Mach 0.2 Empty Tunnel Multiple Components (63.7 m/s)	3.2	1.6 (avg)	3.4	6.5

Table 6.5 Summary of the errors (measured from jet core and empty tunnel tests) and computed modeled uncertainties for the variety of tests taken during this study.

7. Lessons Learned and Suggestions for Improvement

Over the course of developing the final Planar Doppler Velocimetry system several aspects were discovered which aid in taking reliable data. Furthermore, improvements were discovered which are beyond the scope of the project.

Following are some general system improvements and considerations which should be addressed when utilizing PDV:

1. Cameras

The cameras utilized in the development of the three component PDV system (PixelVision) were scientific grade and obtained excellent images with sufficient resolution, linearity, full well depth, and sensitivity. However, the camera incorporated a mechanical shutter which could fail during testing in large wind tunnel environments due to dust and surface contaminants. It would be suggested that if possible new cameras be purchased which incorporate electronic shutters which can operate in a more rugged environment.

2. Simultaneous filter scans

As observed in the last data set it is important that all the camera filters be calibrated against the reference filter by simultaneously scanning them. The Joule-meters provide a more compact and accurate system since they have automatic gain adjustment as the intensity decreases. It would be better if additional Joule-meters could be purchased as a back-up so that all filters can be calibrated simultaneously. This would eliminate the need to calibrate the absorption filter profiles with the flow field being measured.

3. Number of images

Generally it was determined during testing in the large wind tunnel environment that at least 300 images be taken and averaged for each condition involving smoke. This insures that there are enough images to provide an adequate average with a sufficient signal level. For data taken with fewer images generally there are unresolved regions in the data plane due to inadequate seeding. For static calibration shots of the background, dotcard, and green card images it was found that 5 to 10 images are sufficient for averaging.

4. Calibration data

Another discussion that often takes place is what calibration data is necessary to compute PDV data. Although it was demonstrate that running green cards (which are easily taken during a test) can be used to compute the velocity from PDV measurements, it is still necessary to obtain static green card images. This is due to the fact that often there are experimental difficulties encountered. Even though the additional calibration data may not be used in processing, they still are valuable in diagnosing the source of problems when they are encountered. When taking green card images the intensity should be changed sufficiently so that an adequate linear curve fit can be calculated. It was found that taking calibration images at the beginning and end of each data of testing is valuable due to misalignments or changes which may occur during testing. Finally, one of the most critical calibrations is of the filter profiles. Due to the sealed cell design, the profiles don't change significantly over time. However, when taking the profiles they should be checked to make sure that they are of adequate quality and taken as close to the data as possible. For example the profiles taken during the last set of experiments had some difficulties and were of a much lower quality (with more frequency shifts and irregular points) than previous tests. Additionally starved cells should be used exclusively to eliminate the effects of sidearm temperature drift.

5. Seeding System

Although the custom made theatrical smoke (Rosko Fluid) generator installed in the SARL wind tunnel facility provides adequate particles for PDV, the system could still be improved. It should be noted that the entire tunnel should not be seeded for PDV since secondary scattering would introduce significant errors. The smoke system could however benefit from improved position control. It was amazing that the wind tunnel operators could adjust the position with the current pulley system. Improved results and coverage could be obtained if a mechanical traversing system was installed to position the smoke more accurately in the tunnel.

6. PDV data images

For the PDV data taken during the test, images should be taken at a few different frequency settings within the linear region of the filter profile. This insures that there will be data for

each PDV component in which the scattered light is not Doppler shifted out of the filter profile. Additionally background images should be taken with the laser on and seeding off at the run conditions if possible.

7. Laser Speckle

To reduce the random error, laser speckle noise must be reduced. Smith and McKenzie have both provided theoretical treatments of speckle noise that suggest means of reducing speckle noise by hardware modifications.[19,36] Smith, for example, presents the following equation, which gives the ratio of the typical distance between speckle fringes in the camera image plane to the distance across a pixel

$$\delta_{speckle} = \frac{1.2\lambda f\left(m+1\right)n_x}{image\_size_x}$$ Equation 7.1

In Equation 7.1, λ is the wavelength of the laser light, f is the f-number of the optical system and m is the magnification ratio. The number of pixels in the horizontal direction across the array is n_x is and the width of the array is $image\_size_x$. Reducing the ratio in Equation 7.1 reduces the speckle noise because more speckle fringes will appear on each pixel, and thus be integrated together. This equation implies that a large camera aperture (small f-number), a small magnification ratio, and large CCD pixels tend to reduce the speckle noise. In most PDV experiments, m is relatively small compared to unity and therefore does not offer much potential to reduce the speckle noise. The ratio ($image\_size_x/n_x$) is the characteristic dimension of a single pixel. This implies that for a given number of pixels, the larger the CCD array, the better from the point of view of speckle noise. This reasoning provides some guidance when selecting equipment. The most obvious and simple way to reduce the speckle noise is to increase the aperture of the imaging system. Figure 7.1 shows the strong effect of aperture size on speckle noise. Instantaneous images of the jet taken at indicated f-numbers of 32, 16, 5.6 and 2.8 are presented with no data processing. The noise-to-signal ratios in a core region of the jet are, correspondingly, 0.35, 0.22, 0.076 and 0.042. This is the trend predicted by equation 7.1. Data processing steps can also be taken to reduce speckle noise. These steps include pixel binning and low-pass filtering. Both procedures integrate more speckle fringes per pixel to reduce the noise level.

8. Camera Positions

In general, Equation 1.1 places no restrictions on the positions of the Laser or detectors. In reality, the selection of the Laser and detector positions is a strong function of the facility and model. It is assumed that the models tested in the SARL will be aircraft configurations. The geometry of these models includes wing-body junctions and vertical control surfaces. These features can obscure optical access to some relevant regions of the flow. Both illumination and detector views must have optical access to all regions of interest in the flow. If the Laser sheet were introduced from the side, the model geometry may prevent the sheet from propagating into these regions of interest. Furthermore, the detectors must be positioned such that the laser sheet can be imaged. Finally, the combination of the illumination vector and detection vectors must produce a non-singular system of equations. The final consideration is of a practical nature. The Laser must be floated to prevent vibration for effecting Laser seeding. Given these constraints, it is concluded that the Laser should be positioned on top of the tunnel. The detector positions are dependent on the orientation of the sheet and the geometry of the model. To ensure that regions near a wing-body junction can be imaged by all detectors, it is concluded that the system should be concentrated on one-half of the tunnel. With this constraint, the four detector positions shown in Figure 7.2 are evident, two positions on top of the tunnel and two positions on the side of the tunnel. In each case, one upstream and one downstream position are envisioned. With the Laser on top of the tunnel, the detectors on top of the tunnel will have good sensitivity to the vertical and stream-wise velocity components. These positions will have little sensitivity to the cross-stream velocity. If the Laser sheet is angled relative to the flow, one of these positions may be compromised because of inability to view of the sheet. If the Laser sheet is perpendicular to the tunnel free-stream, the detector positions on top of the tunnel provide excellent sensitivity and relatively easy setup. The detector positions on the side of the tunnel will have good sensitivity to the free-stream and cross-stream velocity and very little sensitivity to the vertical velocity. The view from these positions can be obstructed as the angle of attack of the model is rotated. However, these positions can be translated vertically to provide the best view over a range of model positions.
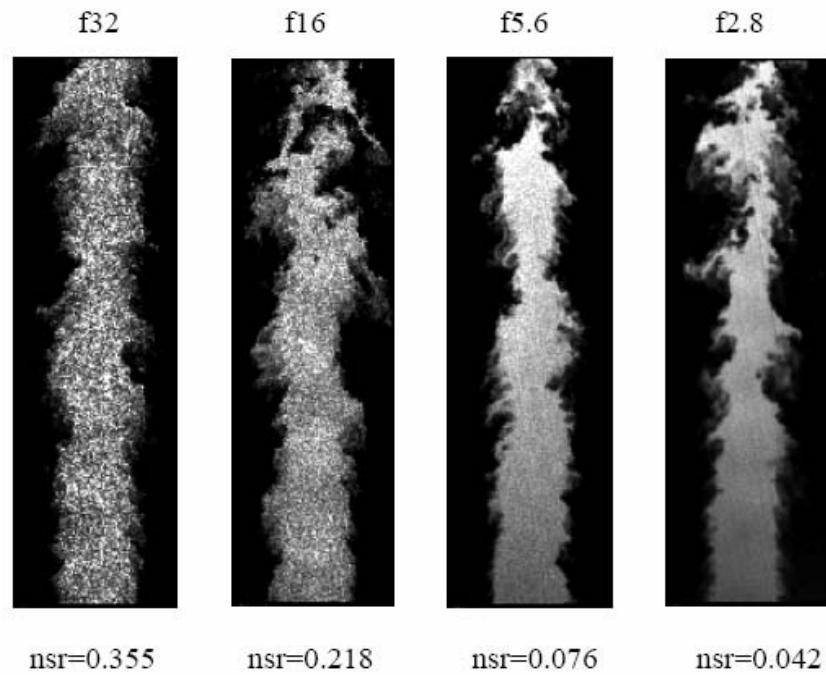
Figure 7.1 Speckle noise in unprocessed jet images as a function of f-number.
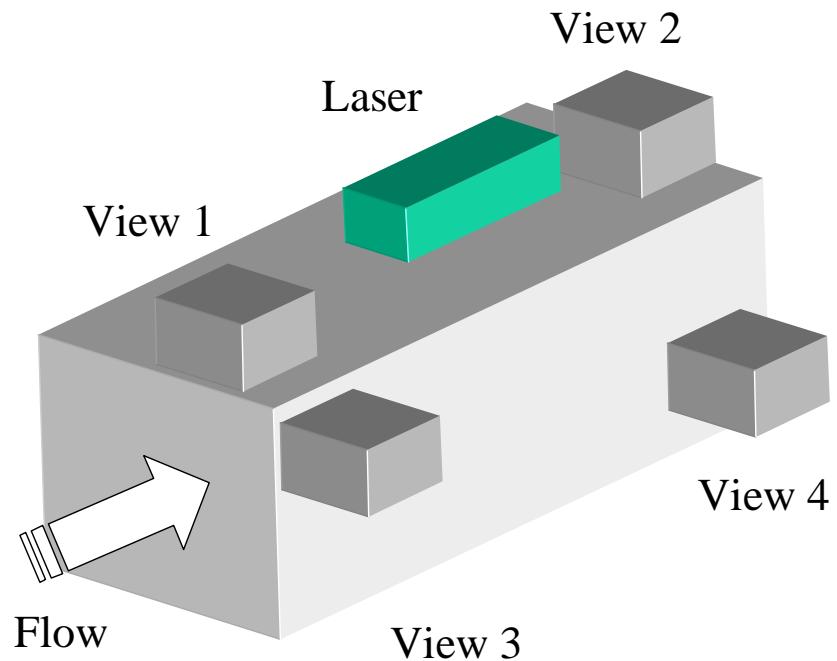
Figure 7.2 Laser and Detector positions for permanet installation.

8. Key Discoveries and Marketing

During the development of the PDV system, it was recognized that the starved Iodine cells were an important component of the system. Furthermore, it was essential that the number density of the Iodine in the cells be controlled. A package was developed that allowed the Iodine cells to be set at a desired number density. A stopcock was then closed to keep the number density constant. This package was then wrapped in heat tape and mounted using a piece of angle, some insulation, and two straps. This package worked effectively, however there were some problems. The stopcock would periodically fail as the cells were thermally cycled, therefore it was important to keep the cells heated at all times. There was always some concern that the cells would fail so they were removed from the detector positions and scanned before and after each days runs. This was time consuming and could lead to misalignment of the detector optics. A means of constructing a permanently sealed cell package that was easy to mount was sought.

The original glass cells were modified slightly and the stem between the cell body and the stopcock was lengthened. This allowed the stem to be burnt off after the number density of the cell has been set. This permanently sealed package was then wrapped in a heating blanket and mounted inside an anodized aluminum housing. The housing contained mounting holes so that the package would accept standard optical components. The stability of the number density and vacuum of the permanently sealed package relieves the need to scan the Iodine cells on a daily basis. In fact, these cells have been demonstrated to be stable for over three years. This improved the productivity of the system in the tunnel. Furthermore, it was recognized that these cells had some commercial viability. To date, over twenty individual cells have been sold by ISSI.

9. Conclusions

A PDV system has been developed with ISSI for measurement of single and multiple velocity components in wind tunnel experiments. During the study the methodology, equipment, data collection programs, and data analysis programs were developed and applied to several flow fields. Several discoveries were made during this development program to improve the system components. These include the development of hardware such as the permanently sealed iodine cells, frequency reference system, and the PDV camera systems. The data acquisition was automated using several programs that provided a user interface and recorded relevant information about the experiment. Data reduction programs and methods were also developed and incorporated into software packages. The system has been developed to the point that multiple velocity components can be measured at the level of uncertainty associated with currently available equipment.

10. References

[1] J. McDaniel, D. Fletcher, R. Hartfield, and S. Hollo, "Staged transverse injection into a Mach 2 flow behind a rearward-facing step: a 3-D compressible test case for hypersonic combustor code validation," AIAA 91-5071, 1991.

[2] P.H. Paul, M.P. Lee, and R.K. Hanson, "Molecular velocity imaging of supersonic flows using pulsed laser-induced fluorescence of NO," *Optics* Letters, 14: 417-420, 1989.

[3] L. Drain, *The Laser* Doppler *Technique*. John Wiley and Sons, 1980.

[4] R.L. McKenzie, "Measurement capabilities of planar Doppler velocimety using pulsed lasers," *Applied Optics,* 35: 948-964, 1996.

[5] H. Komine, and S.J. Brosnan, "Instantaneous, three-component, Doppler global velocimetry," *Laser Anemometry,* 1: 273-277, 1991.

[6] J.F. Meyers, and H. Komine, "Doppler global velocimetry: a new way to look at velocity," *Laser Anemometry,* 1: 289-296, 1991.

[7] G.S. Elliott, "The study of compressible free shear layers using laser based diagnostic techniques," PhD Dissertation, The Ohio State University, Columbus, 1993.

[8] G.S. Elliott, M. Samimy, and S.A. Arnette, "A Molecular Filter Based Velocimetry Technique for High Speed Flows," *Experiments in Fluids,* 18: 107-118, 1994.

[9] M.W. Smith, G.B. Northam, and J.P. Dummond, "Application of absorption filter planar Doppler velocimetry to sonic and supersonic jets," *AIAA Journal,* 34: 434-441, 1996.

[10] R.B. Miles, and W.R. Lempert, "Flow diagnostics in unseeded air," AIAA Paper 90-0624, 1990.

[11] M. Samimy, and M. Wernet, "A review of planar multiple-component velocimetry in high speed flows," *AIAA Journal*, 1999.

[12] H. Komine, S.J. Brosnan, A.B. Litton, and Stappaerts E.A. "Real-time, Doppler global velocimetry," AIAA Paper 91-0337, 1991.

[13] M. Raffel, C.E. Willert, and J. Kompenhans, <u>Particle Image Velocimetry</u>, Springer Verlag, June 1998.

[14] P. Clancy and M. Samimy, "Two-component planar Doppler velocimetry in high speed flows," *AIAA Journal*, 35:1729–1738, 1997.

[15] J. Forkey, N. Finkelstein, W. Lempert, and R. Miles, "Control of experimental uncertainties in filtered Rayleigh scattering measurements," AIAA 95-0298, 1995.

[16] J. Forkey, N. Finkelstein, W. Lempert, and R. Miles, "Control of experimental uncertainties in filtered Rayleigh scattering measurements," AIAA 95-0298, 1995.

[17] W. Press, S. Teukolsky, W. Vetterling, and B. Flannery. *Numerical Recipes in C: The Art of Scientific Computing*. Cambridge University Press, 2nd edition, 1992.

[18] J. Meyers, J. Lee, and A. Cavone, "Three component Doppler global velocimeter measurements of the flow above a delta wing," Lisbon, Portugal, 1992.

[19] R. McKenzie, "Planar Doppler velocimetry performance in low-speed flows," AIAA 97-0498, 1997.

[20] M.Smith, "Application of a planar Doppler velocimetry system to a high Reynolds number compressible jet," AIAA 98-0428, 1998.

[21] T. Beutner, G. Elliott, A. Mosedale, and C. Carter, "Doppler global velocimetry applications in large-scale facilities," AIAA 98-2608, 1998.

[22] D. Rizzetta, "Numerical simulation of the interaction between a leading-edge vortex and a vertical tail," AIAA 96-2012, 1996.

[23] T. Beutner, H. Baust, and J. Meyers, "Doppler global velocimetry measurements of a vortex-tail interaction," Proceedings of the 7th International Symposium on Flow Visualization, 1995.

[24] J. Crafton, C.D. Carter, and G.S. Elliott, "Three-component phase-averaged velocity measurements of an optically perturbed supersonic jet using multi-component planar Doppler velocimetry," *Measurement Science and Technology*, 12: 409-419, 2001.

[25] A. Mosedale, G.S. Elliott, C.D. Carter, and T.J. Beutner, "On the use of planar Doppler velocimetry," AIAA-98-2809, 1998. *Awarded best fluid dynamics paper of 1998 by AIAA.*

[26] G.S. Elliott, and T.J. Beutner, "Molecular filter based planar Doppler velocimetry," Invited article for *Progress in Aerospace Sciences*, 35: 799-845, 1999.

[27] G.S. Elliott, T.J. Beutner, and C. Carter, "Application of planar Doppler velocimetry wind tunnel testing," AIAA-2000-0412, Invited Paper to the *AIAA 38th Aerospace Sciences Meeting and Exhibit,* 2000.

[28] A. Mosedale, G.S. Elliott, C.D. Carter, and T.J. Beutner, "Planar Doppler velocimetry in a large-scale facility," *AIAA Journal*, 38: 1010-1024, 2000.

[29] T. Beutner, G. Elliott, G. Williams, H. Baust, J. Crafton, and C.D. Carter, "Forebody and leading edge vortex measurements using planar Doppler velocimetry," Measurement Science and Technology, 12: 378-394, 2001.

[30] T. Beutner, G. Williams, H. Baust, G. Elliott, J. Crafton, and C. Carter, "Characterization and applications of Doppler global velocimetry," AIAA Paper 99-0266, 1999.

[31] C. Tyler, "A Joint Computational Fluid Dynamics and Experimental Fluid Dynamics Test Program," AIAA Paper presented at the 2004- Aerospace Sciences Meeting and Exhibit.

[32] R.M. Cummings, S.A. Morton, and S.G. Siegal, "Computational Simulation and PIV Measurements of the Laminar Vortical Flowfield for a Delta Wing at High Angle of Attack," AIAA-2003-1102, 2003.

[33] P. Bevington and D. Robinson. *Data Reduction and Error Analysis for The Physical Sciences*. WCB/McGraw-Hill, second edition edition, 1992.

[34] R. McKenzie, "Measurement capabilities of planar Doppler velocimetry using pulsed lasers," 1995. AIAA 95-0297.

[35] P. Clancy, M. Samimy, and W. Erskine, "Planar Doppler velocimetry: Three-component velocimetry in supersonic jets," AIAA 98-0506, 1998.

[36] M. Smith and G. Northam, "Application of absorption filter-planar Doppler velocimetry to sonic and supersonic jets," AIAA 95-0299, 1995.